Particle Production in pp and Heavy Ion Collisions from $\sqrt{s_{NN}}$ = 200 GeV to 5.5 TeV

Thesis Submitted to
The University of Calcutta
for The Degree of
Doctor of Philosophy (Science)

By
Mriganka Mouli Mondal

2010

Dedicated to My Parents

Sital Prosad Mondal and Malati Mondal

ACKNOWLEDGEMENTS

I gratefully acknowledge the constant and invaluable academic and personal support received from my supervisor Dr. Subhasis Chattopadhyay. He entrusted me to complete the STAR analysis presented in the thesis largely independently, which was a huge challenge. With his innovative ideas in doing new things he encouraged me to work in detector design, simulation and analysis mostly from scratch. I would like to sincerely thank him for his dedicated supervision without which it would have been never possible to complete this thesis.

I am very much grateful to Dr. Y. P. Viyogi, Head of the Experimental High Energy Physics and Application group for his encouragement and providing substantial sources of inspirations and profound insight during these years.

I would to like to convey my sincere thanks to Dr. D. K. Srivastava, Head of Physics Group, Dr. S. Pal, Dr. A. Dhara and Dr. P. Barat for their advice and inspirations.

As a member of the ALICE-PMD team I have learned a lot about the high energy physics experiment and teamwork and I am grateful to Dr. Tapan Nayak for his encouragement and during my time at VECC.

I am thankful to Mr. M.R. Dutta Majumdar and Mr.G.S.N. Murthy of VECC for their helps and suggestions at various stages.

I would like to thank Mr. S. Ramanarayana for allowing me to work with him during cosmic trigger development in the electronics lab and thereby learning many basic things. He is truly a cooperating person.

I thank Dr. Bedanga Mohanty for his valuable suggestions and encouragement in many issues during the last five years.

It was a pleasure having useful discussion with Dr. J. Alam and Dr. S. Sarkar and T. Samanta of VECC on issues related physics and computer.

Working on the installation of the Photon multiplicity Detector in the STAR experiment during Oct'2009 at BNL was a learning time for which I want to thank Dr. Zubayer Ahammed and Prithwish Tribedy for their help. I have

learned the techniques of problem solving related to PMD-trigger sysyem from Dr. Zhangbu Xu and Dr. Sushanta Pal. Shift taking in the STAR experiment is a great experience where I have enjoyed and learned a lot and I would like to thank many STAR collaborators I met during data taking.

I also must thank the entire High Energy Physics Experiment & Application Group-members Dr. Premomoy Ghosh, Mr. V. Singhal, Mr. J. Saini and Mr. S. Khan for their help during my stay at VECC.

I would like to acknowledge Mr. Partha Bhaskar, Mr. Tushar Das, Mr. Jayant Kumar, Ms. Nilima Mondal of VECC and Mr. Nabarun Chowdhury, Mr. Santu Karmakar, Mr. Dipankar Bapari, Mr. Sukumar Mondal, Mr. Khokan Mondal, Mr. Tirthankar Paik, Mr. Anjan Naskar, Mr. Amit Mondal, Mr. Kamal Mondal, Mr. Prince Jana, Mr. Sanat Mondal, Mr. Bhaskar Mondal, Mr. Kamal Mondal Jr. of PMD laboratory of VECC for their help time to time.

I want to offer special thanks to Dr. Sunil Monohar Dogra for his constant help regarding software framework details in STAR.

Special thanks to Dr. Jana Bielocikova for being a great collaborator in the work on di-hadron correlation. I must thank Dr. Bielocikova and Dr. Michal Sumbera, Nuclear Physics Inst., Academy of Sciences, Czech Republic for support during my visit to the institute and stay at the Jet Workshop at Prague.

Discussions with Prof. Helen Caines, Prof. Lanny Ray, Dr. James Dunlop, Jan Kapitan either at Brookhaven National Labortory or by e-mail helped me a lot in deciding the proper way to proceed in the analysis. The members of the Jet-correlations groups are remembered for valuable suggestions regarding the analysis.

I would also like to thank Dr. Andreas Morse for useful e-mail discussions I had with him related to PYTHIA and Dr. Gustavo Conessa Balbastre (INFN) for helpful discussion regarding the fragmentation and direct photon production in PYTHIA and HERWIG.

In have enjoyed my time during working on PMD Test-beam experiment, detector module debugging with high voltage, simulation and on physics discussions with Provat, Ajay, Satish, Lokesh, Natasha, Ranbir, Sikshit, Chitrasen, Sidharth.

It was a great to spend time at VECC with my batchmates Jhilam, Arnamitra, Tapasi, Rupa, Saikat and Sidharth. Saikat and Tapasi helped me a lot in

thesis submission related procedure in CU. I specially remember Sidharth for being with me all the time and having valuable discussions all aspects in these years. I have really enjoyed and shared my feelings with Apu da, Atanu da, Biswanath da and Anand da during the period and really thankful to them.I greatly remember Supriya da, Debasish da, Aparajita di, Mili di, Jamil di, Tilak da, Mishreyee di and many others for their help and cooperation time to time.

I will also remember my junior fellow scholars Provash, Prasun, Victor, Santosh, Amlan, Sabyasachi and the most young faces Arnab, Nihar, Sudipan, Nasim, Subhas, Trambak, Yunis, Amlan, Manish, Somnath, Surassee, and Sukanya.

I would like to acknowledge the Department of Atomic Energy, for providing the financial support for the fulfillment of the thesis.

I would like to sincerely thank Prof. Bikash Sinha, DAE Homi Bhaba Chair and Dr. R. K. Bhandari, Director, VECC for their continuous support to continue my work.

I would thank all my teachesrs, specially Mr. Darl Islam, Mr. Subhas Kundu and Mr. Debaprasad Bhanja Choudhary for their encouragement and inspiration in my life.

The thesis is the beginning of the journey amid ups and downs of the roads and I would not have come this far without the love and support of my wonderful parents, Shri. Sital Prosad Mondal and Smt. Malati Mondal. I profoundly thank my parents, my sister, my relatives and friends for their constant love, support, encouragement and most of all, having faith in me.

Mriganka Mouli Mondal
Kolkata, India

Abstract of The Thesis

Exploring the creation of Quark Gluon Plasma (QGP), a new state of Nuclear matter is the main aim in Relativistic Heavy Ion collision experiments which are being performed in the STAR experiment at RHIC ($\sqrt{s}$ = 200 GeV) and ALICE ($\sqrt{s}$ = 5.5 TeV) experiment at LHC. Various observables derived from the properties of the produced particles of the interacting system. Specialized detectors are built for detection of specific types of particles. Dedicated efforts are made in data analysis studying the observables in the soft and hard sector in AA collisions which are then compared with the results form pp and dAu collisions for attaining at a consistent picture. In this thesis as a part of the detector developmental work, fabrication and testing of the Photon Multiplicity Detector (PMD) installed in the ALICE experiment at LHC have been discussed. A detailed simulation using PYTHIA with GEANT is performed with pp collision (at $\sqrt{s}$ = 14 TeV) events at LHC as a readiness exercise of data analysis in such collisions.

In this work, we have also analyzed the STAR data for pp and dAu collisions at $\sqrt{s}$ = 200 GeV for extracting the j_T, k_T of jets using the method of di-hadron correlations. Transverse momentum imbalance (k_T) of the di-jets in pp collisions, by its own nature, has a special importance in characterizing the intrinsic transverse momentum of partons and its broadening in vacuum. Interaction of the hard partons in nuclear medium is expected to lead to the additional broadening in k_T. Centrality dependence of j_T, k_T in dAu collisions have been studied with the STAR data for the first time in wide kinematic region. Comparisons have been made with the results form PYTHIA and HIJING models. Jet transverse momentum ($\sqrt{\langle j_t^2 \rangle}$) and jet acoplanarity effect ($\sqrt{\langle k_t^2 \rangle}$) for pp at $\sqrt{s}$ = 200 GeV using π^0-ch correlation for π^0 selected in the p_T range 6.5-18.5 GeV/c are found to be 598 $\pm$ 28 (stat) GeV/c and 2.80$\pm$0.04(stat)$\pm$0.27(sys) GeV/c respectively. The effect of the k_T broadening form the dAu data is found to be 10-20%. These results will help in interpreting the results from heavy ion collisions like AuAu at RHIC illuminating the formation of the high-density matter. We have also performed a simulation study for γ-jet detection as a golden channel in the Photon Spectrometer (PHOS) acceptance in ALICE. The work consists of a method of using the transverse momentum imbalance of the di-jets to enhance the purity of the direct photon detection in pp for ALICE in LHC energy.

Contents

List of Figures

List of Tables

Chapter 1

Introduction

The branch of high energy physics is related to the understanding of the fundamental constituents of the nature and their interactions. The fundamental constituent particles can be classified into three categories : *leptons* which interact only electro-magnetically and weakly, *hadrons* that are subject to strong interactions, and the *gauge bosons* that act as mediators of the fundamental forces. Twelve types of particles : Electron, muon, tau, the respective neutrinos and their antiparticles belong to the lepton family. Relatively, hadrons exist in a large number and they can be explained as made of *quarks*. Hadrons are divided into *mesons* (containing a quark and an antiquark) and *baryons* (consisting of three quarks). The Standard Model (SM) of particle physics describes the theory of interactions among these particles. It incorporates the weak, the electromagnetic, and the strong interactions among the four fundamental forces governing the nature. The weak and the electromagnetic forces differ by the range of interactions which is related to the mass of the mediators, e.g. the photons and the Z^0 and $W^{\pm}$ bosons. Photons allow a very long range interactions while large masses of Z^0 (91 GeV/c^2) and $W^{\pm}$(80 GeV/c^2) limits the range of weak interaction. Quantum Chromodynamics (QCD), the theory of strong interaction treats the interactions among the quark and gluons as due to the excited states of vacuum. Two notable features of the theory of strong interactions are the confinement of quarks inside the hadrons and the asymptotic freedom at a scale of large momentum transfer.

1.1 Matter at extreme conditions

Historically the study of nuclear matter at extreme conditions of temperature and pressure is of prime interest since 1970's. It is related to the matter existing at the early universe at about 10 microsecond after the Big Bang and the matter existing at the center of the neutron star. It has been discussed in [1] that when the *energy* density ε of the matter exceeds some typical hadronic value ($\sim$ 1GeV/fm^3), matter no longer consists of separate hadrons (protons, neutrons, etc.), but of their fundamental constituents, quarks and gluons. In such a condition, the quark and gluons are no longer confined inside the hadrons but remain free to move inside the whole nuclear matter. The matter is then considered to be not the normal nuclear matter but to be existing in a new phase which is commonly known as the "quark Gluon Plasma" (QGP). The universe should have gone through such a state at the early stage after its creation, the time of which is believed to be about 10 μsec after Big Bang. The deconfined state might be observed inside the core of a neutron star where the density is several times the normal or cold nuclear matter density (0.15 nucleons/fm^3). The experimentalists might be able to arrive at the state of deconfined matter either by achieving an energy density much higher than the critical value in collider experiments like RHIC and LHC or by compressing the nuclear matter at the fixed target experiment at FAIR.

The Quantum Chromodynamics (QCD) has been suggested to be the underlying theory of strong interactions and the new phases of nuclear matter could be associated with the corresponding changes in the structure of the vacuum [2, 3]. The phenomena of quark confinement was a consequence of the non perturbative structure of the vacuum which gets modified at high temperatures and/or densities, suggesting the quarks and gluons under such conditions would be deconfined. A perturbative description of the interactions at the critical energy density, $\varepsilon_C \sim$ 1GeV/fm^3 and at the associated critical temperature, T$_C \sim$ 170 MeV is difficult be carried out where the coupling constant is of the order of unity. Various model-treatments are useful to overcome this limitation. MIT bag models [4] treats the confinement of the colored objects, quarks and gluons inside some finite region, *the bag*. Under a constant pressure B_{bag} acting over a physical vacuum, the positive energy E_{bag} ($B_{bag}.V_{bag}$) is defined in terms of the bag pressure and the bag volume V_{bag} [4]. The string models [5, 6, 7, 8] on the other hand, consider a real object, a string, made of color field lines and the connecting quarks. Understanding of the QCD in extremely non-perturbative domain along with the lattice calculations [9, 10, 11] led to a detailed investigations of the thermodynamic properties of quark gluon plasma [11].

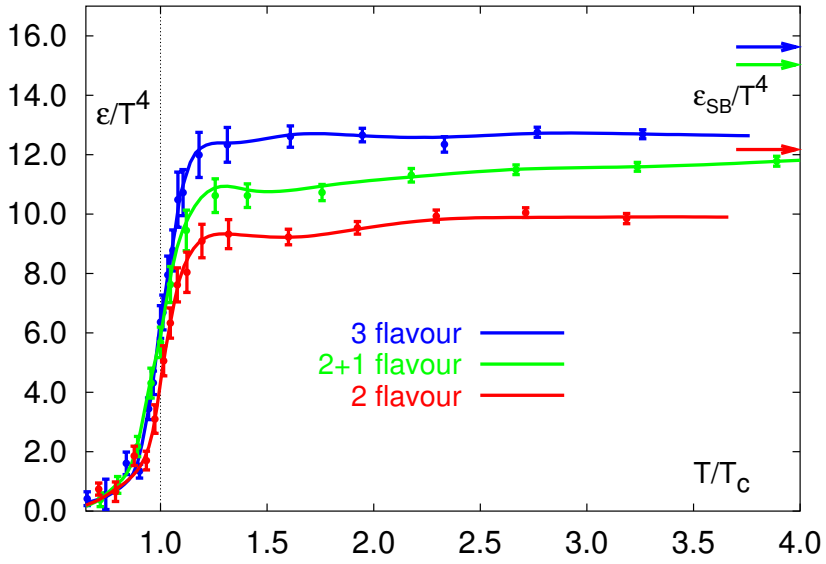

Figure 1.1: Lattice QCD results [12] for the energy density ε/T^4 as a function of the temperature scaled by the critical temperature T_C.

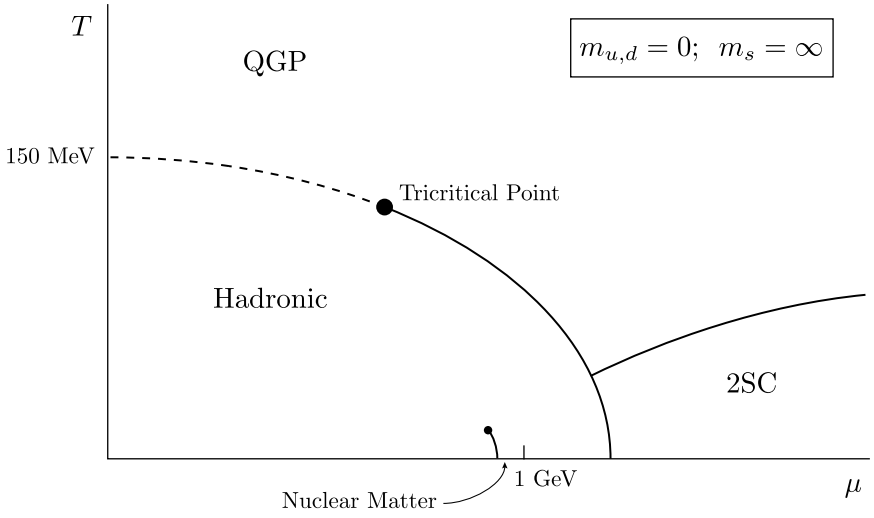

Figure 1.2: Theoretical phase diagram of the nuclear matter consisting of two massless quarks represented as the variation of temperature T with the baryon chemical potential μ [13].

According to the lattice QCD calculation, the Fig. 1.1 predicts a phase transitions at $T \approx 170$MeV which corresponds to an energy density of

$\epsilon \approx 1\text{GeV/fm}^3$, nearly an order of magnitude larger than that of the normal nuclear matter. The values of temperature and/or energy density depend on the dimensional values and the arrows on right top indicate the values at the Stefan-Boltzman limit. The exact order of the phase transition is not known. At zero net baryon density, it is first order considering only gluons in the gauge theory. Addition of two (up and down) or three light quarks (adding a strange quark) led to the behavior of a transition from the second order to a crossover. Fig 1.2 shows the phase diagram of an ideal nuclear matter for vanishing light flavour quark masses (up and down) and infinite strange quark mass. For a large baryon chemical potential, the order of phase transition is first order and lies below the tricritical point and at higher temperature the transition is second order. However, for nonzero light quark masses the dashed line becomes a smooth crossover and the tricritical point become a critical point. As the center of mass energy of the colliding ions increases, the net baryon chemical potential decreases and therefore the transition of phase boundary will automatically shift from the second order to a smooth crossover. In order to locate the critical point, the RHIC is currently scanning a wide region of phase boundary in a Beam Energy Scan (BES) program by varying the center of mass energy of collisions ($\sqrt{s_{NN}}$) from 7.0 GeV to 200 GeV.

1.2 Relativistic Heavy Ion Collisions

Over the years, fixed target heavy ion collision experiments at the Berkeley Bevalac (1975–1985), the BNL AGS (1987–1995) and the CERN SPS (1987–present) are carried out using the beam energies from several GeV/n (AGS) to 158 GeV/n (SPS) using nuclei of a wide range of atomic masses. The highest center of mass energy achieved in these experiments reaches upto $\sqrt{s_{NN}} =$ 17 GeV. The Relativistic Heavy Ion Collider (RHIC) at BNL which started taking data in 2001, is a dedicated facility for the study of nuclear collisions at the ultra-relativistic energies [14] reaching upto $\sqrt{s_{NN}} = 200$ GeV for Au + Au system. Increase in the center of mass energy of the colliding system made it possible to study the phase transition properties of the bulk nuclear matter at temperatures and densities large enough to create the phase of quark gluon plasma. As RHIC, the experiments provide a unique window into the hot QCD vacuum, with opportunities for fundamental advances in the understanding of quark confinement, chiral symmetry breaking and the possibility of the creation of new and exciting phenomena in the realm of nuclear matter at the highest densities.

The setups in high energy heavy ion collision experiments consist of detectors suitable to measure the energy and momentum of the particles produced in the collisions. The fate of the colliding nuclei manifest itself through the detailed study of various properties like temperature, parton number density, energy density, opacity, collective behavior, thermalization during quark-gluon phase, deconfinement, number and nature of the degrees of freedom, recombination of quarks and gluons to form final-state hadrons, chiral symmetry restoration, time evolution of system parameters, equation of state, color and thermal transport properties, critical behavior among others.

1.2.1 Energy density in a heavy ion collision experiment

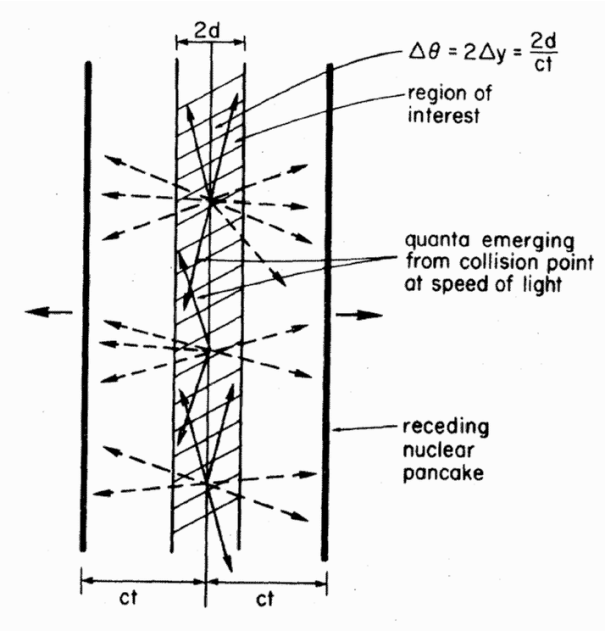

Figure 1.3: Figure from [15] illustrating Bjorken's description of the geometry of the initially produced particles at a time t after the overlap of two incoming nuclei in a particlar frame.

At the relativistic energy two colliding nuclei are Lorentz contracted and appear as thin "disks". The overlapping time of the two nuclei will be very small and all the particles will be produced essentially from the overlapping region of area "A" and width "2d" at some proper time τ_{form}. The Fig. 1.3 shows the Bjorken picture of the collision scenario. Bjorken's [15] estimation of the

energy density can be expressed in following form

$$\begin{aligned}\langle\varepsilon(\tau_{form})\rangle &= \frac{dN\langle m_T\rangle}{dz\,A} = \frac{dN(\tau_{form})}{dy}\frac{\langle m_T\rangle}{\tau_{form}A} \\ &= \frac{1}{\tau_{form}A}\frac{dE_T(\tau_{form})}{dy} \end{aligned} \tag{1.1}$$

It is valid at mid rapidity (y = 0) where the particles have an average total transverse energy of $\langle m_T\rangle$ and $E = m_T$ for particles with no longitudinal velocity.

One assumption which is to be satisfied in the Bjorken picture is that the formation time should be much larger that the crossing time ($\tau_{form} >> 2R/\gamma$). The formation times are estimated to be about 1 fm/c at SPS, 0.2 fm/c at RHIC and 0.1 fm/c at the LHC. The estimated energy densities at AGS($\sqrt{s_{NN}} = 5GeV$), SPS($\sqrt{s_{NN}} = 17GeV$), and RHIC($\sqrt{s_{NN}} = 200GeV$) are about 1.5, 2.9 and 5.4 GeV/fm^3 respectively.

1.2.2 Thermalization

For thermodynamical description of the system, it is required that the system achieves the local thermal equilibrium which also explains the collective behavior of the system. Multiple scatterings of partons at the formation time lead to softer parton branching and finally a strongly coupled system. Thermalization time (τ_{therm}) is defined as the time required for the system to attain a local thermal equilibrium. One can then use the hydrodynamic expansion of the system and can calculate collective flow parameters like the elliptic flow parameter v_2 [16, 17, 18, 19, 20]. The thermalization time (τ_{therm}) can be deduced from the energy density at the formation time. For RHIC, it requires very short thermalization time, in the range of 0.6-1.0 fm/c, in order to reproduce the magnitude of elliptic flow. The energy density estimated in this range of thermalization time is 5.4 to 9.0 GeV/fm^3, which is well above the critical energy density for the phase transition and therefore one expects a deconfined bulk thermalized matter to be formed at RHIC.

1.2.3 Evolution of the System

The formation and evolution of the matter consists of hard and soft processes corresponding to large and medium momentum transfers respectively. The

hard processes can be treated through the QCD dynamics but there exists no "first principle" calculation for softer processes and the phenomenological models are used for explaining the data. The system evolves with time and two pictures can be thought of working in particle production,
i) the string picture based on the phenomenological models of soft hadron-hadron interaction, and
ii) the field-theoretic parton picture of hadron interactions within the firmly established framework of perturbative QCD.

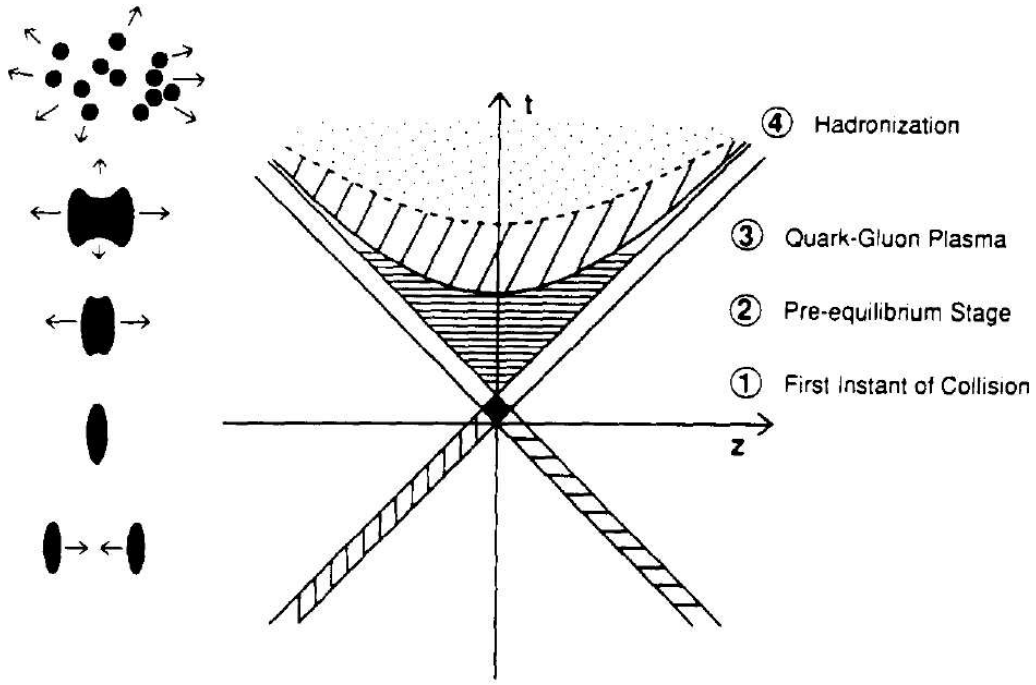

Figure 1.4: Diagram of the longitudinal space-time evolution of a relativistic nucleus-nucleus collision, from the moment of nuclear overlap, via pre-equilibrium and quark gluon plasma phase to the formation of final state hadrons.

The Fig 1.4 describes the evolution of a relativistic nucleus-nucleus collision, from the moment of nuclear overlap, via pre-equilibrium and quark gluon plasma phase to the formation of final state hadrons. With time, the system undergoes through a pre-equilibrium stage with multiple partonic scatterings towards the formation of an equilibrated partonic medium. The expansion and cooling of the medium leads to the transition to a hadronic phase (mixed phase), and finally a pure hadronic gas which eventually produces free streaming particles(hadronization). In this picture first-order phase transition is as-

sumed. It should be mentioned that depending on the colliding energy and the collision geometry (say for Au-Au system), the size and lifetime of the partonic medium is defined.

1.2.4 Signatures of QGP

The basic aim of the study of high energy heavy ion collisions is to characterize the nature of the medium formed in the relativistic heavy ion collisions. It is assumed that in smaller systems like pp and dAu the QGP is not formed. Therefore in most of the studies relating to QGP, observations from pp and dAu collision experiments are considered to be baseline for the study. Often peripheral collisions of heavy ions are treated like pp collisions and are used for reference signatures. We discuss below some of the well known observables predicted to provide signatures of various stages of the collisions.

Production of dileptons and direct photons : Dilepton channels from $q\bar{q} \rightarrow l^+ + l^-$ and direct photon production channels $q\bar{q} \rightarrow \gamma g$ (annihilation) and $qg \rightarrow q\gamma$ (compton) are interesting signals for probing QGP.

In a medium of quarks and gluons in the deconfined phase, a quark can interact with an antiquark to form a virtual phootn γ^* and the virtual photon subsequently decays into a lepton l^+ and an antilepton l^-.

$$q\bar{q} \rightarrow l^+ + l^- \qquad (dilepton) \tag{1.2}$$

Direct photon channels are

$$q\bar{q} \rightarrow \gamma g \qquad (annihilationprocess) \tag{1.3}$$

$$qg \rightarrow q\gamma \qquad (comptonprocess) \tag{1.4}$$

The interaction probability of photons and leptons with the color medium being very low, they are not likely to suffer further interaction in the plasma. Momentum distribution of $l^+ + l^-$ and γ depend on the momentum distributions of the quarks and gluons in the plasma, which are governed by the thermodynamic conditions of the plasma. Therefore l^+, l^- pairs [21, 22, 23] and γ_{direct} [24, 25, 26, 27] carry information of the thermodynamic state of the medium at the moment their production.

Dileptons produced by the processes like Drell-Yan, hadronic channels and the resonance decays like ρ, ω, ϕ and J/ψ act as background. The resonance decay

produces a peak at the low mass region of < 1GeV, while the peak from the J/ψ belongs to the higher invariant mass region. The invariant mass spectra of the dilepton pair in the mass range of 1.0 to 2.8 GeV is important to study where the contribution from the QGP phase is predicted to be dominant [28]. The contribution from the QGP phase is highly dependent on temperature of the plasma and therefore on the energy density.

Direct photons have dominant background contributions from the hadronic decay photons and photons from the pre-equilibrium stage. Experimentally decay photons from π^0 and η contribute to $\sim 99\%$ of all the photons. It makes the detection of direct photons extremely challenging [29, 30]. Moreover the bremsstrahlung photons contribute in the soft photon region significantly and it is hard to identify experimentally.

J/ψ suppression : Due to the presence of the color charges in the plasma (QGP), the color charge of a quark is subject to screening, popularly known as Debye screening. J/ψs produced in the pre-equilibrium stage when get confined in the QGP region, the interaction strength between the c$\bar{c}$ string becomes weaker. c$\bar{c}$ therefore dissociates and combines with the light quark to produce open charm mesons e.g. $D(c\bar{u}$ and $c\bar{d})$, $\bar{D}(\bar{c}u$ and $\bar{c}d)$, $D_s(c\bar{s})$ and $\bar{D}_s(\bar{c}s)$. Therefore, the suppression of J/ψ production is considered to be a signature of the presence of quark-gluon-plasma [31].

Strangeness enhancement : The matter formed in heavy ion collisions evolves and finally hadronizes into particles. Bulk thermodynamic properties of the early stage of the colliding matter can be measured from the hadron spectra, the collective flow and the correlation among the soft hadrons. Statistical models derive the equilibrium properties of a macroscopic system from the measured yields of the constituent particles [32, 33]. Hagedron [34] and Fermi [35] models can be used to find the ratios of particle production yield in high energy collisions, where the conserved quantities such as baryon number and strangeness play an important role [36].

In nucleus nucleus collisions, $u\bar{u}$, $s\bar{s}$ and $d\bar{d}$ pairs are produced and subsequently the by combination with neighboring quarks and antiquarks, strange particles are produced. Thus, the mesons like K and ϕ produced in the collisions($K^+ = u\bar{s}, K^0 = d\bar{s}, K^- = \bar{u}s$ and $\phi = s\bar{s}$) carry strangeness. In pp and pA collisions the ratio of a strange to non-strange particle, $\frac{k^+}{\pi^+} < 0.1$ [37]. For a Hagedron gas at thermal (where the total momentum of the system is conserved, i.e the system is in local thermal equilibrium) and chemical equilibrium (no new net particles are formed) at T = 200 GeV, $\frac{k^+}{\pi^+}$ ratio is about to 0.38. The ratio increases with the temperature indicating the system ap-

proaching towards equilibrium [37, 38, 39, 40, 41]. The content of the strange quarks and strange antiquarks is much greater in QGP than what one would expect either in a colliding nucleonic matter or in an equilibrated hadron gas without a phase transition. Hence, an enhancement in the number of strange quarks and antiquark is suggested as a signal for the presence of quark gluon plasma [37]. Furthermore, in the stopping region, the QGP with non-zero quark chemical potential (μ_s =0, μ_d =0), production of $K^+ = u\bar{s}$ or $K^0 = d\bar{s}$ is more favorable than $K^- = \bar{d}s$ or $\bar{K}^0 = \bar{u}s$. Thereby, the measurement of s and $\bar{s}$ relative to u and $\bar{u}$ is useful to find the thermodynamic states of QGP.

Elliptic flow : The spatial distribution of the colliding matter resembles an ellipsoid for collisions other than the head on collisions. The system having an initial spatial anisotropy, when attains local thermal equilibrium and undergoes through the hydrodynamical expansion, a pressure gradient is developed which is largest in the shortest direction of the ellipsoid. The gradient produces higher momenta in that direction, quickly reducing the spatial asymmetry. The spatial anisotropy finally gets transfered to the momentum anisotropy [42], thereby carrying the signature of the collectivity of the medium known as elliptic flow. The eccentricity (ε) of the reaction zone is

$$\varepsilon = \frac{\langle y^2 \rangle - \langle x^2 \rangle}{\langle y^2 \rangle + \langle x^2 \rangle} \tag{1.5}$$

The elliptic flow is measured by the azimuthal anisotropy. The elliptic flow is defined as the second Fourier coefficient v_2, where

$$\frac{d^2N}{d\phi p_T} = N_0(1 + 2v_2 \cos(2\phi)) \tag{1.6}$$

Here ϕ is the angle of the particles with respect to the reaction plane. Measurement of v_2 as a function of p_T is known as the measurement of the differential v_2. The most direct evidence that v_2 is related to spatial asymmetries present early in the reaction is that v_2 at low p_T approximately scales with the initial eccentricity (ε) of the reaction zone [43, 44]. v_2 shows interesting behaviors for different particle species where the heavier particles are expected to have higher v_2 [45, 46]. Baryons and mesons when scaled by the constituent quark content, shows a scaling of v_2 suggesting the development of v_2 in the partonic phase of the strongly interacting matter. This topic is of major interest after detailed studies at RHIC.

HBT : Bose-Einstein correlation commonly known as the Hanbury Brown and Twiss (HBT) interferometry, between identical (pion/kaon/photon) particles,

lying nearby in the momentum space provides a measure of the space time extent of the source at the end of the reaction. HBT results are sensitive to the expansion dynamics integrated over the collision. Theoretical predictions of a large source size and/or a long duration of particle emission [47, 48, 49] can explain the presence of a long-lived mixture of phases in the matter as it undergoes a first-order phase transition from a quark-gluon plasma back to the hadronic phase.

In e^+e^-, pp or $\bar{p}p$ collisions the order of rapidity-space-time correlations indicate that the small rapidity pions are produced from a smaller section of the the order of 1fm in the longitudinal direction from the colliding point while the larger rapidity pions are produced from outer region [50, 51]. In nucleus nucleus collisions the number of pion source points is proportional to the number of baryon baryon collisions and the values of the transverse HBT radius parameters [52] are found to be increasing with centralities.

The HBT parameters ($R_{x,y,z}$) provide an interesting way to study the properties of the nuclear matter undergoing a phase transition. In case of a first order phase transition, the long lived mixed phase leads to $R_x > R_y$, where R_x and R_y are the radius parameters along and perpendicular to the detector direction respectively [53, 54, 55].

In HBT analysis, multidimensional Gaussian fits are made to the normalized relative momentum distributions yielding fit parameters, $R_{\rm long}$, $R_{\rm side}$, $R_{\rm out}$ [56], also referred to as HBT radii, where the correlation function is parameterized as

$$C_2 = 1 + \lambda \exp(-R^2_{\rm side}q^2_{\rm side} - R^2_{\rm out}q^2_{\rm out} - R^2_{\rm long}q^2_{\rm long}). \tag{1.7}$$

Dependency of the HBT radii on the transverse momentum of the particle pairs and their ratio $R_{\rm out}/R_{\rm side}$ are interesting results obtained from STAR and PHENIX [57, 58].

Energy Loss of High p_T particles : Hard probes arising in the early stage of the collisions penetrate the locally equilibrated expanding medium. For instance, at RHIC energy fraction of the particles produced by the hard scattering is sufficiently large. Due to the larger momentum trnsfer Q^2, hard scattered partons are created at a time $\delta\tau \sim 1/p_T$ ($\delta\tau \sim 0.2$ fm for GeV/c parton), whereas most of the partons from the plasma are formed and equilibrated at a later time $\sim 1/g$T ~ 0.5 fm/c [59]. The hard scattered partons propagate along approximately straight eikonal lines through the plasma until $\tau \sim$ R ~ 5 fm/c in central AuAu collisions. During the passage of the hard partons through the medium, they interact with the partonic medium and its

interaction leds to the conversion of the high p_T partons into soft hadrons. The elastic energy loss of partons in a QCD plasma of temperature T$\sim$300 MeV is small (dE/dx $<$ 0.5 GeV/fm for a quark jet with E=30 GeV [60]). However, due to the non-Abelian nature of gluon radiation in QCD, the radiative gluon energy loss, dE/dx, depends linearly on the thickness of the medium, and could be much larger than the elastic energy loss. Jet quenching due to the gluon radiation in QGP should therefore become an observable as a suppression of high p_T hadron yields in heavy-ion collisions.

The energy loss in the partonic medium from GLV [61, 62, 63] approach assumes the medium to be composed of well separated colored scattering centers (with Debye screened Yukawa potentials) with mean free path of a parton $\lambda > 1/\mu$. The color screening length of the medium is given by

$$\Delta E = \frac{C_R \lambda_s}{N(E)} \frac{L^2 \mu^2}{\lambda_g} log \frac{E}{\mu} \tag{1.8}$$

where E is the jet energy; C_R is related to the color factor; L is the plasma depth; μ is the typical transverse momentum transfer; λ_g is the radiated gluon mean free path; and N is the number of gluons emitted. The energy loss is predicted to be proportional to the gluon density $\frac{dN_g}{dy}$. The reference for studying

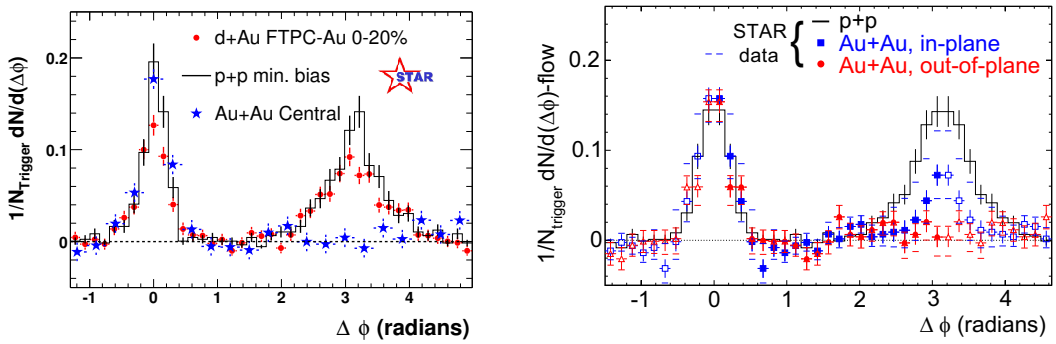

Figure 1.5: Dihadron azimuthal correlations at high p_T. Left panel shows the correlations for pp, central dAu and central AuAu collisions (background subtracted) from STAR [64, 70]. Right panel shows the background-subtracted high p_T dihadron correlation for different orientations of the trigger hadron relative to the Au+Au reaction plane [71]

the effect is taken from the nucleon-nucleon collisions. AA collisions can be taken as multiple number of pp collisions and the scaling of AA collisions based on the binary collision picture is used for studying the supression. $R_{AB}(p_T)$,

the ratio of inclusive charged hadron yields in AB (either AuAu or dAu) collisions to pp, corrected for trivial geometry effects via scaling by $\langle N_{bin} \rangle$ is given by,

$$R_{AB}(p_T) = \frac{dN_{AB}/d\eta d^2p_T}{T_{AB} d\sigma_{NN}/d\eta d^2p_T}. \tag{1.9}$$

(where $\langle N_{bin} \rangle$ is number of binary collisions, the calculated mean number of binary nucleon-nucleon collisions contributing to each AB centrality bin): where the overlap integral $T_{AB} = \langle N_{bin} \rangle \sigma^{pp}_{inelastic}$ represents the geometry correction.

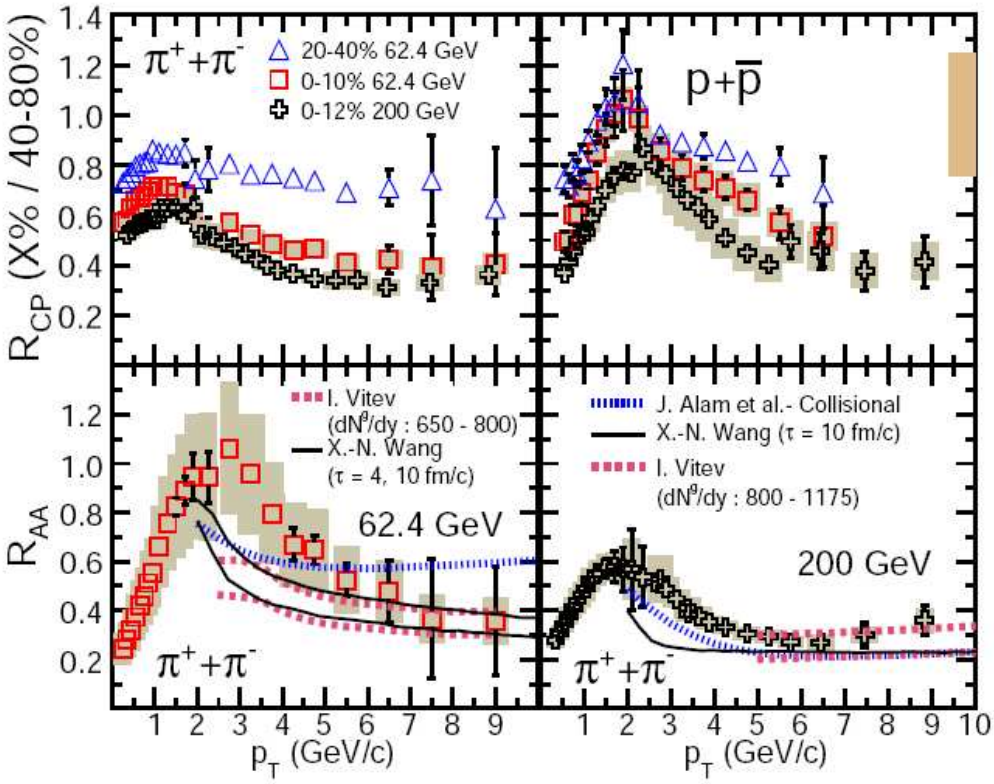

Figure 1.6: p_T dependence of the nuclear modification factors R_{AA} and R_{CP} of hadrons in AuAu collisions at $\sqrt{s_{NN}}$=200 and 62.4 GeV. Data are compared to calculations from the radiative and collisional energy loss scenarios [73]

.

At RHIC energy, a striking phenomenon seen on $R_{AB}(p_T)$ is that the large p_T hadrons in central AuAu collisions are suppressed by a factor ≈ 5 relative to the naive (binary scaling) expectations. Conventional nuclear effects,

such as nuclear shadowing of the parton distribution functions and the initial state multiple scattering, cannot account for the suppression. Furthermore, the suppression is not seen in d+Au collisions and unique to Au+Au central collisions, thereby proving experimentally that it results not from the nuclear effects in the initial state (such as gluon saturation), but from the final state interaction (FSI) of the hard scattered partons or their fragmentation products in the dense medium generated in Au+Au collisions [64, 65, 66, 67]. The enhancement in R_{dAu} for moderate p_T at mid-rapidity, known as the Cronin effect [68] is generally attributed [69] to the influence of multiple scattering of partons through the cold nuclear matter *prior to* the hard scattering that produces the observed high-p_T hadron.

Another approach known as the dihadron correlations are used to study this effect. Dihadron correlations for pp and dAu are very interesting in the perspective that the azimuthal correlation function of the associated charge particles with respect to the trigger particle shows a clear peak at the near side ($\Delta\phi = 0$) and another at the away side ($\Delta\phi = 2\pi$). These peaks are characteristics of jets produced in these collisions. The disappearance of the away side jet structure observed in the central AuAu collisions at RHIC energy clearly demonstrates the interaction of the hard p_T partons in the partonic medium (Fig. 1.5 (left)). The path length traversed by the jet in the medium depends upon its orientation with respect to the reaction plane. The Fig. 1.5(right) shows that the out-of-plane suppression is larger compared to the in-plane suppression demonstrating the path length dependence of the effect.

A very different interpretation of the suppression observed in central AuAu collisions is based on the initial-state gluon saturation effects [72]. The Saturation effectively modifies the parton distribution function such that the number of hard scatterings and consequently the high p_T hadron yield is reduced. In [72], it was proposed that the gluon saturation phenomena alone may account for a significant part of the observed high p_T hadron suppression pattern. Data from the AuAu collisions alone can not unambiguously distinguish between these two scenarios.

However like other initial-state effect, saturation is expected to be present in dAu collisions and should result in ∼30% suppression in minimum bias dAu collisions [72]. Results from the dAu collisions at $\sqrt{s_{NN}}$= 200 GeV shows the modification of high p_T hadron yields due to the initial state nuclear effects for a system in which a hot, dense medium is not produced in the final state. The the final state effect due to the formation of dense medium for central AuAu collisions is manifested as the suppression of the away side jet. Fig 1.6

shows the p_T dependence of the nuclear modification factors R_{AA} and R_{CP} of hadrons in AuAu collisions at $\sqrt{s_{NN}}$=200 and 62.4 GeV. Data are compared to calculations from radiative and collisional energy loss scenarios [73].

The results of high p_T physics from the complicated heavy-ion collision experiments can only be interpreted based on the understanding from the simpler system like pp, e^+e^-, pA, and eA. Characteristics of hard-scattered partons being well understood in pp and e^+e^- collisions, can be used as a calibrated probe for heavy-ion collisions. On the other hand, the knowledge from the eA and pA collisions on the nuclear parton distributions and k_T broadening can help us to fix the initial conditions prior to the hard-scattering processes in heavy-ion collisions. By combining this knowledge with the measurements of jet production in heavy-ion collisions, one expects to disentangle various nuclear effects, and learn about the modifications of jets in the medium in the final state. The work presented in this thesis will be in the high p_T domain where we will discuss mostly about jets and associated correlations in reference systems e.g. pp and dAu.

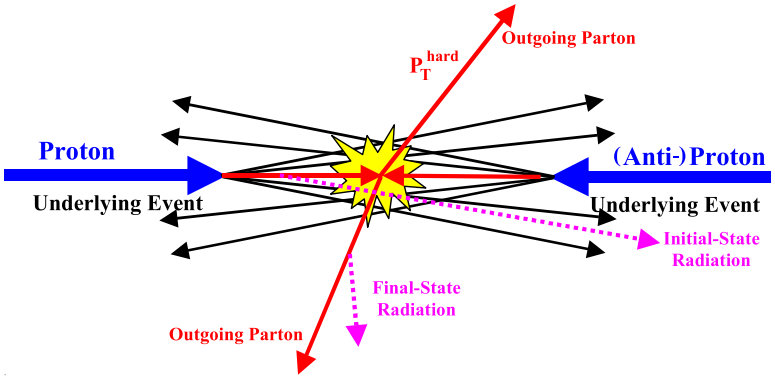

Figure 1.7: Illustration of a 2-to-2 parton scattering in the hard collision of two incident hadrons [74].

1.3 Jets from high energy physics experiments

In relativistic heavy ion collisions or high energy hadron hadron collisions, the scattering reactions can be classified into four categories i.e. elastic, diffractive, soft-inelastic and hard.

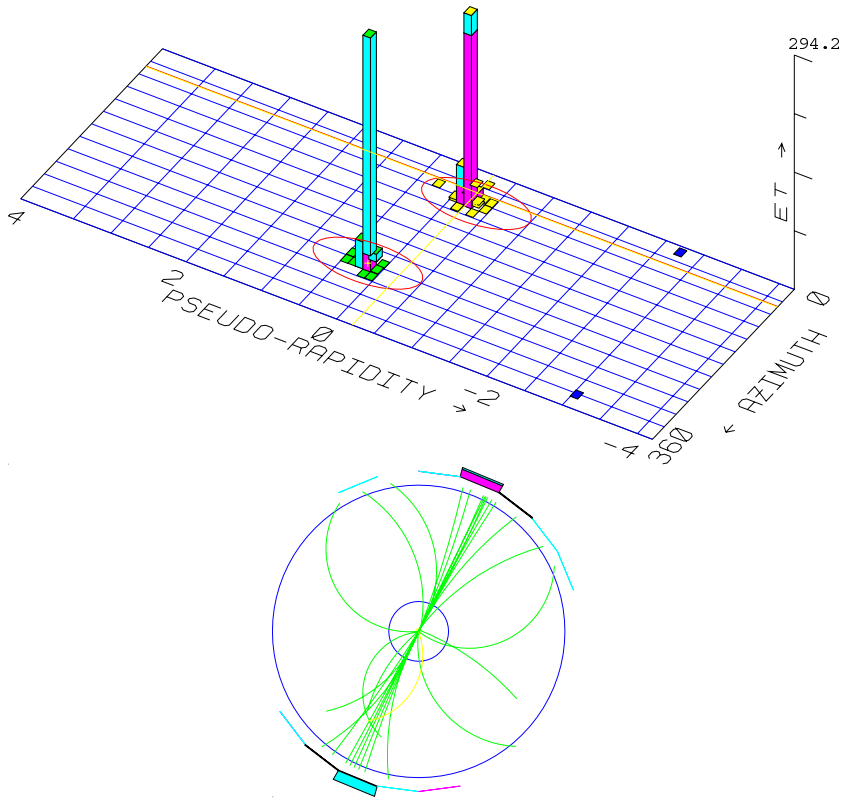

Figure 1.8: A jet event for pp at $\sqrt{s} = 1.96$ TeV in the CDF [75] calorimeter (top) and central tracking chamber (bottom) identified by the cone jet finder, JetClu, with $R = 0.7$

1. **elastic :** Initial and final state particles are of the same type and of same energy.

2. **diffractive :** One or both of the incident hadrons break apart to form fragments.

3. **soft-inelastic :** In this process also the incident hadrons break apart but at a low momentum transfer which is described by the exchange of virtual hadrons (Regge theory). It comprises the largest part of the cross section.

4. **hard :** Two partons from each of the colliding hadrons undergo elastic scattering with a large momentum transfer. Eventually a large number of particles are formed by the fragmentation of the outgoing partons which appears as a stream of collimated particles, known as jets.

Jet physics belongs to the high p_T domain of particle production via hard scattering processes. A hard scattered event is illustrated in Fig. 1.7 where the outgoing partons fragment into jets of particles. The rest of the particles in the event are softer particles which arise due to the breakup of the remnants of the colliding hadrons and form the underlying event. The partons undergoing hard scattering may suffer energy loss before and after the hard scattering by the mechanism of gluon radiation, which are commonly known as Initial State Radiation (ISR) and Final State Radiations (FSR) respectively.

Hard scattered partons evolve via short-distance interactions over a very short time scale and the subsequent fragmentation produces hadronic final states. The connection of the jets from the final state particles help to map the partonic level picture. The Fig. 1.8 shows a di-jet event in the CDF calorimeter, where the jets are lying back to back in ϕ ($\Delta\phi \approx 180^0$).

1.3.1 Different types of hard scattering : $\gamma - jet$, jet-jet events

The hard scattering between the constituents of two colliding protons is described by the quantum chromodynamics (QCD) [76] as a point like scattering. The production of hadrons is treated in QCD as a result of the interaction of quarks and gluons. In analogy to QED processes, QCD processes can often be expressed in the from of Feyman diagrams. The main difference to the QED in terms of the interaction is the involvement of the self-coupling of gluons. Fig. 1.9 shows the Feynman graphs for 2→2 hard scatterings processes. First three are jet-jet processes with I) t-channel scattering, II) qq-scattering process and III) a t-channel scattering with a 3-gluon vertex. The items IV and V are of special types of channels ($\gamma-$jet) which produce direct photons. The first one is annihilation of a quark and an antiquark with the creation of a photon and a gluon. The last one is the scattering of a quark and a gluon resulting in a quark and a photon after scattering which is analogous to an electromagnetic Compton scattering.

$\gamma-$jet is an interesting channel of the 2→2 hard scattering process originating from the annihilation ($q\bar{q} \rightarrow g\gamma$) and the Compton ($qg \rightarrow q\gamma$) processes. The photons coming out of these processes are known as *direct gammas* which usually act as single photons, with no other particles in their vicinity.

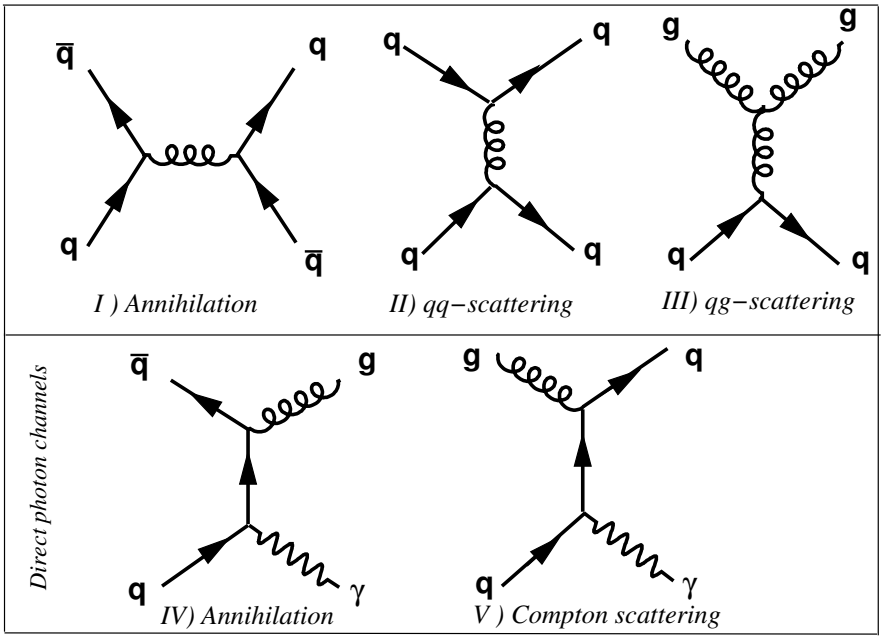

Figure 1.9: Feynman diagram for 2→2 hard scatterings processes.

1.3.2 Formalism of hard scattering : parton distribution function, fragmentation function

Partonic hard processes manifest themselves via jets, a stream of particles collimated in $\eta - \phi$ space. The mechanism of production of the high p_T ($> 2GeV/c$) particles is mostly by the hard scattering of the constituents of two colliding nuclei. The production mechanism of these particles are well understood in pp collisions. Hard scattering of two partons belongs to the domain of perturbative QCD and the interaction between two particles can be treated as an interaction of free particles.

The constituents of the proton are quarks and gluons (together known as partons) which carry the momentum of the proton in units of the Bjorken variable, $\mathrm{x} = 2p_T/\sqrt{s}$. The scale of momentum transfer defines the parton distribution function in x, which is measured by the experiments. The momentum distribution of partons inside the hadrons are assumed to be universal. Fig. 1.10 shows the parton distribution function (PDF) measured by ZEUS with global fit data. In hadronic interaction, the elastic scattering of the partons leads to the production of two high p_T partons. As quark and gluons cannot exit as

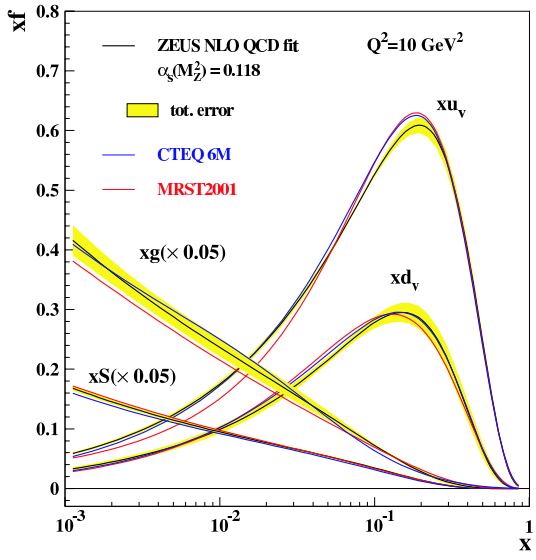

Figure 1.10: Comparison of the PDFs from the ZEUS fit [77] to global fits by MRST2001 [78] and CTEQ 6M [79]. "f" in xf in the Y-axis indicates the notation for different partonic species (u, d).

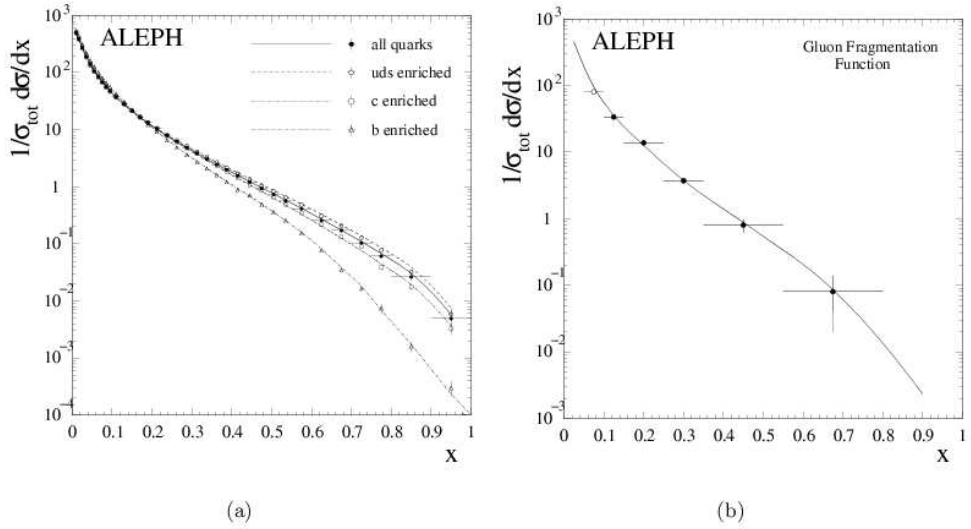

Figure 1.11: Inclusive fragmentation function for a) quarks and b) gluons, measured by the ALEPH experiment [80].

free particles, partons can be described as an intermediate state. The partons finally transform into hadrons in a mechanism called fragmentation. The term "fragmentation" indicates the breakup of "strings" that mediate the strong force and connects to the high-p_T partons as they escape. Strings can represent the long range behavior of QCD, where the string connects the two color charges with a binding energy dependent upon the length of the string. While the string is elongated, it breaks apart forming another quark and antiquark pair. Hadrons eventually appear from the pairing of quarks and antiquarks. The p_T spectra of the particles in a jet can be expressed in terms of $x = p_t^{hadron}/p_t^{jet}$ and the Fig. 1.11 shows the measured distribution in x (which is known as the fragmentation function) from the ALEPH [80] experiment.

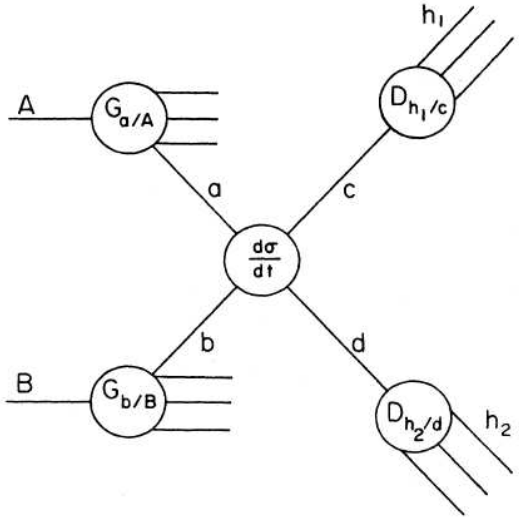

Figure 1.12: A schematic representation of a hard scattering process where G is the distribution function and D is the fragmentation function.

The particle production in proton-proton collisions by hard scatterings can be explained as a three step process.
a) Two partons carrying $x_a = p_{za}/p_{zA}$ and $x_b = p_{zb}/p_{zB}$ undergo hard scattering where p_{zA}, p_{zB}, p_{za}, p_{zb} are the Z-components of the momenta of the colliding protons and the constituent partons respectively as shown in Fig. 1.12.
b) Elastic x-section of two hard scattered partons $ab \rightarrow cd$ can be calculated analytically from QCD as represented by $\frac{d\sigma}{d\hat{t}}(ab \rightarrow cd)\delta(\hat{s} + \hat{t} + \hat{u})$.
c) Finally the fragmentation function $D_{C/c}(z)$, explains the probability of finding a particle C of momentum p_{zC} fragmenting from the parton c of momentum p_{zc}.
The entire process can therefore be explained as a result the equation,

$$E_c \frac{d\sigma}{d^3 p_c}(AB \to C + x) = \sum_{a,b,c,d} \int dx_a dx_b dz_c G_{a/A}(x_a) G_{b/B}(x_b) D_{C/c}(z_c) \frac{\hat{s}}{z_c^2} \frac{d\sigma}{d\hat{t}}(ab \to cd) \delta(\hat{s} + \hat{t} + \hat{u}) \quad (1.10)$$

describing the production of particle C in the interaction of two nuclei A and B, where $G_{a/A}(x_a)$ and $G_{b/B}(x_b)$ represent the parton distribution functions of nuclei A and B. $D_{C/c}(z_c)$ is the probability of getting a particle "C" of momentum p_C while fragmenting form the parton "c" of momentum p_c.

1.4 Intra-jet and jet-jet correlations : j_T and k_T

In pp collisions if the colliding partons move along the collisions axis, the two emerging partons would have the same magnitude of transverse momenta pointing opposite in azimuth. However it was found that there is a net imbalance in the transverse momentum vectors of the dijets. It indicates that each of the partons carries an initial transverse momentum $\vec{k}_T$ [81], originally described as "intrinsic"-k_T [82]. This results in an acoplanarity, i.e, one of the jets lies out of the plane defined by the collision axis and the other jet. The jets are therefore non collinear having a net transverse momentum $\langle p_T^2 \rangle = 2.\ \langle k_T^2 \rangle$. The net transverse momentum of the outgoing parton-pair is $\sqrt{2}\langle k_T \rangle$, where $\langle k_T \rangle$ is the apparent transverse momentum of each colliding parton.

In reality, it is found that the net transverse momentum of the parton pairs can be expressed as:

$$\frac{\langle p_T^2 \rangle_{pair}}{2} = \langle k_T^2 \rangle_{intrinsic} + \langle k_T^2 \rangle_{soft} + \langle k_T^2 \rangle_{NLO} \quad (1.11)$$

, where the intrinsic part refers to the possible "fermi motion" of the confined quarks or gluons inside the parton, the NLO refers to the long tail due to the initial and final state gluon radiation and the soft part refer to the actual Gaussian-like distribution observed as $p_{T\,pair} \to 0$, which is explained by resummation [83]. From naive expectation based on nucleon constituent quark mass, pure intrinsic k_T can be $\approx$ 300 MeV/c [82]. Measurements of dileptons, diphotons or dijets over a wide range of center of mass energies give rise to $\langle k_T \rangle$ upto 5 GeV/c [84] because of the soft and the NLO contributions as discussed earlier. Several experiments at ISR needed extra p_T-kick to the hard scattered partons to explain the data and due to its large value the obtained $\langle k_T \rangle$ is explained by the k_T-smearing [85, 86]. $\sqrt{\langle k_T^2 \rangle}$ is explained as

$dx_a G_{a/A}(x_a, Q^2) \rightarrow dx_a d^2k_{Ta} f(k_{Ta}) G_{a/A}(x_a/Q^2)$ where the distribution $f(k_{Ta})$ is to be of the form $f(k_{Ta}) = \frac{e^{-k_T^2/\langle k_T^2\rangle}}{\pi\langle k_T^2\rangle}$ for the parton a and similarly for the parton b also. This formalism is to be applied to eq. 1.10 for theoretical calculation of particle production incorporating the effect of k_T smearings.

Jet fragments have a momentum $\vec{j_T}$ perpendicular to the partonic transverse momentum. The magnitude of $\langle j_{Ty}\rangle$, the mean value of j_T projected onto the plane perpendicular to the jet thrust, measured to be ≈400MeV [87] at low energy pp collisions, which is found to be similar for e^+e^- collisions [88, 89]. It should be mentioned that $\sqrt{\langle k_T^2\rangle} = \frac{2}{\sqrt{\pi}}\ \langle k_T\rangle = \sqrt{\pi}\langle |k_{Ty}|\rangle$ where the two component vector $\vec{k}_T$ with k_{Tx} and k_{Ty} are Gaussian distributed with equal standard deviations.

$\langle j_T\rangle$ and $\langle k_T\rangle$ can be measured either by reconstructing the dijets or by the method of the correlation among the particles produced in dijets. The method was originally used in CERN-ISR to measure the acoplanarity [81, 82, 87, 88].

1.5 Nuclear Modification of intrinsic k_T

In presence of the nuclear medium in the collisions, the multiple scattering within the medium likely to increase the parton transverse momentum. This is commonly known as k_T-broadening. It is expected that there will have a $A^{1/3}$ dependence due the the nuclear radius incorporating the path length for the collisions, L$\sim A^{1/3}$ [90, 91, 92]. It was found that high-p_T hadrons are not suppressed in proton-nucleus collisions, but produced copiously. This effect, named after James Cronin, demonstrates that the bound nucleons cooperate producing high-p_T particles. There are several models trying to explain the Cronin enhancement [93, 94, 95, 96]. A complimentary observable of Cronin enhancement, related to the additional transverse momentum delivered to the parton is the dijet broadening in the nuclear medium. It is found that there is a strong dependence of $\langle k_T^2\rangle$ on energy of the collisions [90] and on the Q^2 on the parton parton interactions [87, 97].

There are two large classes of models [98] used to explain the k_T broadening: (1) soft or Glauber scattering where the multiple scattering is either at the hadronic or partonic level and (2) semi-hard multiple scattering where the multiple scattering is at the partonic level.

In both the soft and hard scattering models, the increase $\Delta\langle k_T^2\rangle = \langle k_T^2\rangle_{p+A} - \langle k_T^2\rangle_{p+p}$ is proportional to the product of the scattering cross section and the nuclear thickness function,

$$\Delta\langle k_T^2\rangle \propto \nu(b,\sqrt{s}) - 1 = \sigma_{\rm MS}(\sqrt{s})T_A(b) \tag{1.12}$$

where $\nu(b,\sqrt{s})$ is the number of interactions, b is the impact parameter of the collision, $\sigma_{\rm MS}$ is the multiple scattering cross-section, and $T_A(b)$ is the nuclear thickness function. In the specific case of hard sphere nucleon scattering [99] $\nu(b,\sqrt{s}) = \sigma_{\rm NN}(\sqrt{s})\frac{3A}{2\pi R^2}\sqrt{1-\frac{b^2}{R^2}}$, where R is the nuclear radius, which gives an $A^{\frac{1}{3}}$ increase in $\Delta\langle k_T^2\rangle$.

It has been found that [100, 101] both the models predict that broadening increases with centrality. However Hwa and Yang [102] explained the Cronin effect at RHIC without imparting successive transverse momentum kicks to the scattered partons. The model proposed by them based on a parton combination model also suggests that there is very little or no increase in k_T from pp to dAu collisions.

Results for PHENIX [103, 104] in this perspective is very important. PHENIX studied the jet properties in pp collisions using the correlation method in the trigger particle p_T upto 8 GeV/c. For dAu, they show no major modification of the fragmenation width and of the acoplanarity measured by the quantity $\langle\ \sin\phi_{i,j}\ \rangle$ between the trigger and the associated particles. In the present work we have analyzed the STAR data (the acceptance is in full ϕ and the p_T-trigger(of π^0) of higher reach) and tried to extract $\langle\sqrt{k_T}\rangle$ values for pp and dAu. Therefore the major aim of the thesis in the analysis part is to address the modification of the k_T in the nuclear medium.

1.6 Organization of the work

Over last several decades, a dedicated program is being performed worldwide aimed at understanding the strongly interacting matter at extreme conditions. At extreme temperature and energy density or at extreme compression, the matter is believed to go through a transformation from the hadronic matter to a deconfined state called Quark Gluon Plasma (QGP).

It is suggested that one can access such states experimentally by colliding two heavy nuclei at varying energies. Presently, two major accelerator facilities, RHIC at BNL and LHC at CERN have been delivering beams for performing

experiments keeping the search of QGP as a major goal. These experimental setups are major installations consisting of several sub detectors designed to detect particles of specific identity and/or of specific kinematic range.

In addition to building the experimental setup and taking data, it is necessary that one understands all observations in detail by varying the collision energy and the colliding species. Collisions with smaller nuclei e.g. pp or dAu would act as reference systems, results from which can be compared with the results from AA collisions for describing interesting effects if any. In this thesis, we have discussed the works related to building and testing of a detector system for a high energy heavy ion experiment and analysis of data for understanding some of the basic properties of such collisions.

In Chapter-2, a brief overview is given on STAR experiments at RHIC with an emphasis of sub-detectors from which data have been used in subsequent analysis.

Chapter-3 discusses the development of a major detector system, i.e. the photon multiplicity detector (PMD) being used in the ALICE experiment at LHC-CERN. Details of design, fabrication and performance simulation have been presented. Another PMD working on similar principle is taking data in the STAR experiment at BNL.

Subsequent chapters in this thesis have been devoted to data analysis, development of methods for data analysis and interpretation of the available data.

Chapter-4 presents in detail the study of azimuthal correlation in pp and dAu collisions towards understanding the properties of jets formed at RHIC energy. Details of data reduction, analysis techniques and extraction of jet properties have been discussed.

At RHIC and LHC energies, single photons produced by compton process are extremely interesting probes for characterizing the collision. However, photons from other sources e.g. fragmentation photons act as major backgrounds in the detection of single photons. In chapter-5 we have described a method developed for enriching the direct photon sample in high energy collisions.

In chapter-6, we investigated the production of baryon at forward rapidity and made an estimate of the the amount of stopping in AA collisions at top RHIC energy.

We have summarized the results with a short discussions on highlights of the results in chapter-7. An outlook has also been presented in this chapter.

Chapter 2

STAR experiment at RHIC

2.1 Introduction

Historically, the first high energy heavy ion experiments were performed at the Lawrence Berkley National Laboratory in 1970,s. Later the Alternating Gradient Cyclotron (AGS) at Brokhaven in 80's and the Super Proton Synchrotron at CERN in 90's delivered heavy ion beams. Experiments were carried out in all the above mentioned accelerators were fixed target experiments and the highest center of mass (CM) energy achieved was limited to $\sqrt{s_{NN}} \approx 17$ GeV.

The first dedicated heavy ion collider experiment which has been taking data at the Relativistic Heavy Ion Collider (RHIC) at the Brookhaven National Laboratory (BNL) with the highest centre of mass energy achieved for heavy ion collisions ($\sqrt{s_{NN}} = 200$ GeV for AuAu collisions). The Large Hadron Collider at CERN is equipped for colliding lead (Pb) ions at $\sqrt{s_{NN}} = 5.5$ TeV. The work presented in this thesis has two parts. The first part contains the fabrication and testing of a Photon Multiplicity Detector (PMD) which is installed at the ALICE experiment at LHC for detection of photons at the forward rapidity. We have also discussed the analysis of data taken by the STAR experiment at RHIC as second part of the work. In this chapter therefore, we present a brief review of the RHIC complex and the STAR experiment with the detectors relevant to the present analysis.

2.2 The RHIC Complex

Fig. 2.1 shows the schematic view of the RHIC accelerator complex. RHIC consists of a Tandem van de Graaff pre-accelerator, the Booster Synchrotron, the Alternating Gradient Synchrotron (AGS), the interconnecting beam transfer lines as injecting chain, and two independent concentric acceleration and storage rings in a tunnel with a circumference of 3.8 km. Beams in those two rings are called yellow and blue beams, with the yellow beam going counter-clock-wise and the blue beam going clock-wise. Storage ring magnets are superconducting. There are six intersection points, four of which had been instrumented with experiments, STAR, PHENIX, PHOBOS, and BRAHMS. Currently PHOBOS and BRAHMS have ceased operating and only the two bigger experiments of STAR and PHENIX are taking data. The primary accelerating capability of RHIC is for heavy-ion collisions at energies up to 100 GeV/n per beam. With the magnet system set at B_ρ=839.5 Tm for 100 GeV/n Au beams, the operational momentum increases with the charge-to-mass ratio, resulting in kinetic energies of 125 GeV/n for lighter ions and 250 GeV for protons. In other words, the top collision energy for the heaviest nuclear beams is $\sqrt{s_{NN}} = 200$GeV/nucleon pair, while for pp it is $\sqrt{s} = 500$ GeV. The luminosity (the number of ions per unit time per unit cross-section) is 2×10^{26} $\mathrm{cm}^{-2}\mathrm{s}^{-1}$ for 100 GeV/n AuAu collisions averaged over the nominal 10-hour storage time.

RHIC is a versatile accelerator which provides features unique among other hadron colliders. Firstly, thanks to two independent ring-design, it is capable to collide beams of unequal species, such as protons or light ions with heavy-ions. Secondly, it provides collisions between beams of heavy-ions over a wide energy range from top energy down to injection or even lower so as to connect to previous experimental results. The luminosity is energy dependent and is approximately proportional to the operating energy.

The acceleration scenario of the RHIC accelerator can also be seen in Figure 2.1. Here the Au beam is used as an example. Au beams originate in a pulsed sputter ion source and are accelerated by the Tandem Van de Graaff accelerator to the kinetic energy of $\sim$1 MeV/n and with QT=+12 charge state. While exiting from the Van de Graaff the Au-ions are further stripped to a charge state of +32. They are then transferred to the Booster synchrotron, where beams are captured into bunches and accelerated to 95 MeV/n. A foil at the Booster exit strips all atomic electrons but two tightly bound K-shell electrons. Then the Au-ion beam is filled into the AGS, de-bunched and re-

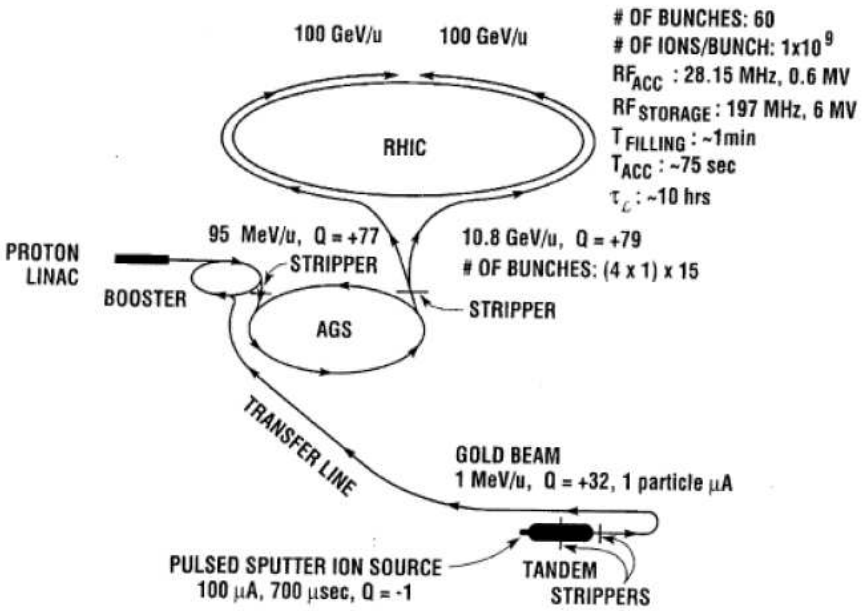

Figure 2.1: The RHIC accelerator complex.

bunched into final bunches, and then accelerated to 8.86 GeV/n and fully stripped. After exiting from the AGS the beam is transported to the RHIC storage rings. In the storage ring, beam is stored and accelerated utilizing two Radio- Frequency (RF) systems. One, at 28 MHz, captures the AGS, bunches and accelerates them to the top energy, the other one, at 197 MHz, provides a short collision diamond (σ_L ~25 cm) to efficiently utilize the luminosity. At its required energy the yellow and blue beams are cogged (two beams are adjusted to meet at the center of detectors) and the collisions start. When the luminosity declines to an unacceptable level, typically after several hours of operation, the beam is dumped.

2.3 The STAR Detectors

The STAR experiment is built to detect charge and neutral particles in a wide-acceptance coverage. The detector is designed so as to handle resolving high density tracks with high momentum resolution with particle identifications. Therefore, STAR can measure decay products and large-angle correlations

over a wide range of species. The central detectors in STAR cover a region of -1< η <1 with several other detectors placed in the coverage to increase the acceptance in the forward rapidity region. A solenoidal magnet is used to produce a uniform magnetic field upto 0.5 T in the central tracking detector region for obtaining good momentum resolution of the charged particles. Fig. 2.2 Fig. 2.3 shows the schematic diagram of the STAR detectors.

The STAR detectors consist of the followings:

- The heart of the STAR detector is the Time Projection Chamber (TPC) occupying the largest volume in the central region around the collision point [105]. The TPC has a cylindrical shape with a length of 4.2m and a radius of 2 m, aligned along the beam pipe. It provides tracking information along with the particle identification using the specific energy loss of particles traversing the gas volume.

- Inside the TPC, the Silicon Vertex Tracker (SVT) and the Silicon Strip Detector (SSD) provide additional tracking information to improve the extrapolation of tracks to the vertex [106, 107]. SVT consists of three concentric barrels of silicon drift detectors situated at 5, 10 and 15 cm from the beam whereas SSD is situated 23 cm away from the beam axis. The primary goal for these detectors was the measurement of the secondary decay vertices of strange particles, that can improve the signal-to-background ratio for these signals.

- Surrounding the TPC is the Central Trigger Barrel (CTB), an array of 240 scintillator modules acting as a trigger and multiplicity detector. CTB has subsequently been replaced by a Time-of-Flight(TOF) detector. The purpose of the TOF detector is to extend the particle identification capabilities of the STAR detector to high transverse momentum [108]. The full TOF coverage requires 120 TOF trays, 60 in the east ($0 < \eta <$ 1) and 60 in the west (-1 $< \eta <$ 0). TOF also has triggering capabilities.

- The outermost layer of the experiment is the Electromagnetic Calorimeter (EMC), useful for the detection of photons, identification of electrons and the reconstruction of neutral pions. The EMC is divided into two subgroups: the Barrel EMC covers the mid-rapidity region between -1 $< \eta <$ 1 and the Endcap EMC, mounted between the endcaps of the TPC and the magnet, extends the coverage to η = 2.0. All these sub-detectors mentioned before are enclosed in a solenoidal magnet providing a maximum field of B = 0.5T [109].

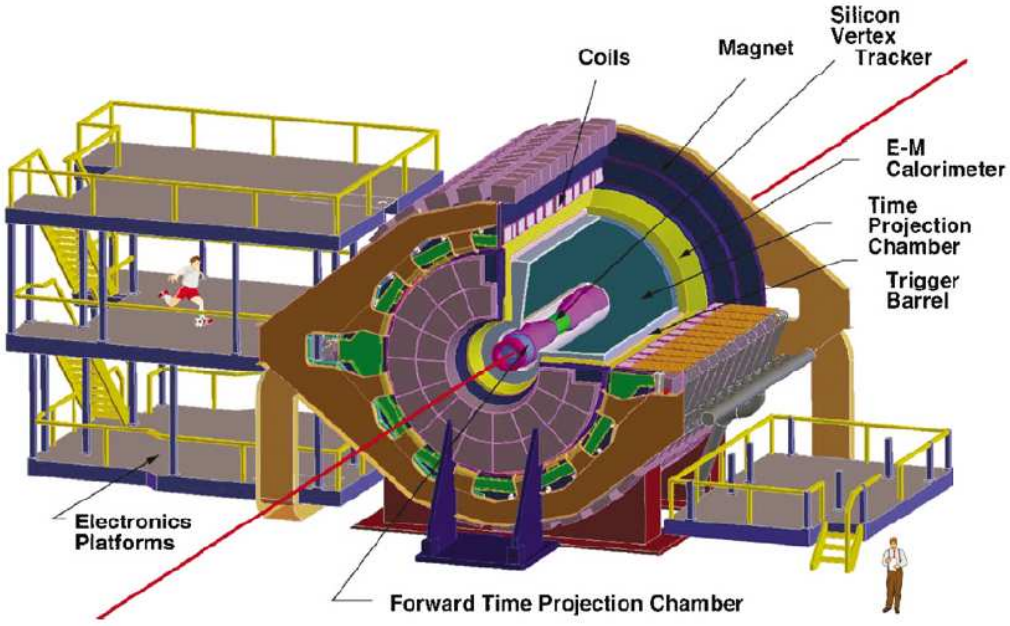

Figure 2.2: Cross sectional View of the STAR detectors (forward detectors indtalled at the late stagere are notshown).

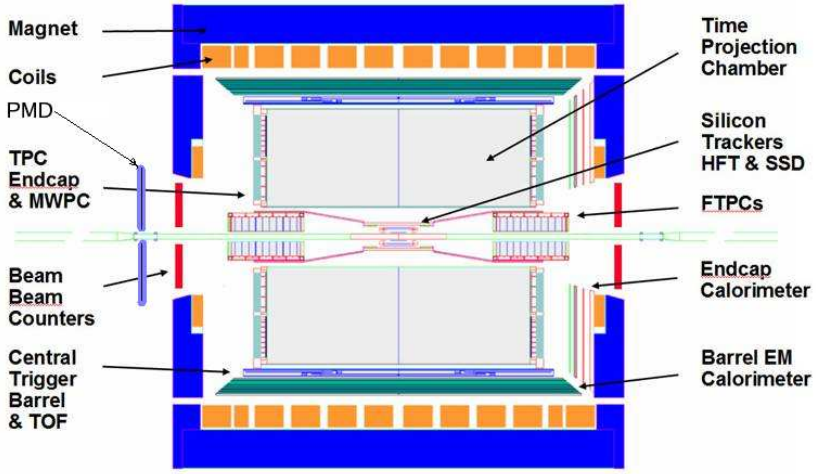

Figure 2.3: Side View of the STAR detectors including the forward detectors e.g. PMD.

- The Forward Time Projection Chambers (FTPCs) extend the tracking capabilities of STAR to the forward and backward regions from $2.5 < \eta < 4.0$ [110]. The FTPCs are also provided with a centrality measure for the d+Au run in 2003, where a TPC-based centrality used for Au+Au would have introduced a large bias.

- The Photon Multiplicity Detector (PMD) detects the spatial distribution of photons between $-3.8 < \eta < -2.3$ [111]. Due to the fact of having a common η coverage for the PMD and the FTPC, the study of photon hadron correlations in the forward rapidity is possible in the quest of searching the formation of the disoriented chiral condensate. PMD can also be used for centrality selection and transverse energy estimation. PMD has been designed and built entirely by the Indian Collaborations institutes.

2.3.1 Time Projection Chamber (TPC)

The main tracking detector of the STAR experiment is the Time Projection Chamber (TPC) which covers the full azimuthal angle in a pseudorapidity region of $-1.8 < \eta < 1.8$. The TPC can track particles with momentum between 100 MeV/c and 30 GeV/c and identify them via the characteristic energy loss up to 1 GeV/c. The reading out of an event creates a three dimensional image of approximately 70 millions of points, enough to handle the high multiplicity of central Au+Au collisions. A schematic layout of the STAR-TPC is shown in Fig. 2.4.

The TPC is a hollow cylinder parallel to the beam line, with an inner radius of 0.5 m, and outer radius of 2 m and a overall length of 4.2 m. The cylinder is filled with P10 gas, a mixture of 90% argon and 10% methane, kept at 2 mbar positive pressure in order to prevent air to enter from outside. It sits in the homogeneous magnetic field which is generated by the solenoidal magnet and oriented along the beam axis.

The TPC is located inside a uniform magnetic field of field strength of $B = 0.5$ T which leads the charge particles to follow helix-shaped trajectories and allows the determination of a particle's momentum from the curvature of the helix. A charged particle going through the TPC ionizes the gas molecules, on an average every few tenths of a millimeter along its path. A central membrane at the center of the TPC is kept at -28kV. The electric field makes the ionization electrons drift to the endcaps.

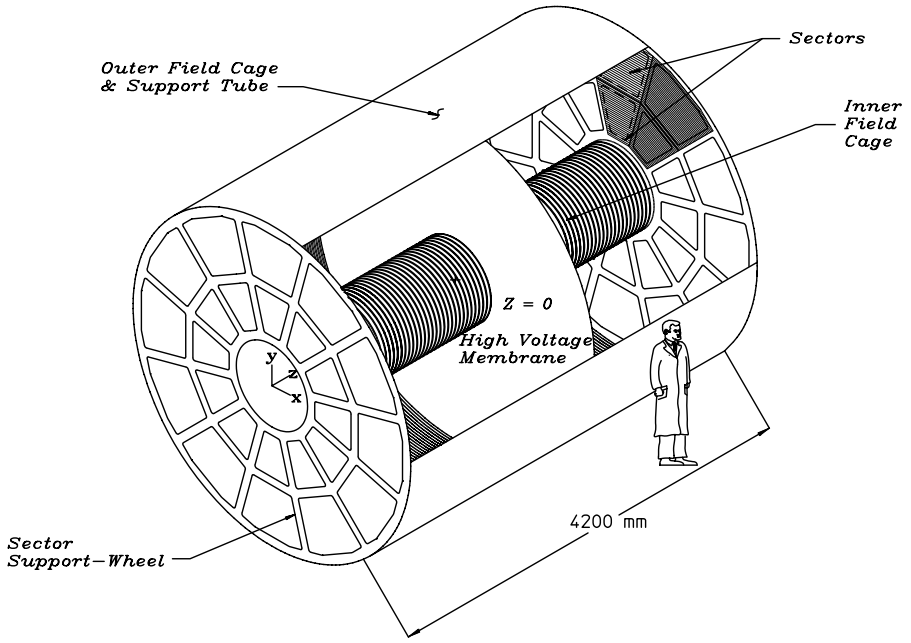

Figure 2.4: Schematic layout of the STAR-TPC

Each endcap consists of 12 multi-wire proportional chambers (MWPCs), each of them covering an angle of 30^0. The MWPCs consist of three planes of wires (the gating grid, the ground grid and the anode grid) and a pad plane connected to the front-end electronics. A schematic layout of the read out region is shown in Fig. 2.5.

During the event read-out, the gating grid is open to allow the drift of ionization electrons. After that, it closes to prevent positive ions from drifting to the TPC volume.

The ground grid separates the homogeneous drift field from the strongly inhomogeneous amplification field surrounding the anode wires.

The anode area is characterized by a strong inhomogeneous electric field which accelerates the drifting electrons and generates an electron avalanche. This allows a signal amplification, which is proportional to the initial number of the drifting electrons. Finally, the anode grid collects all the electrons.

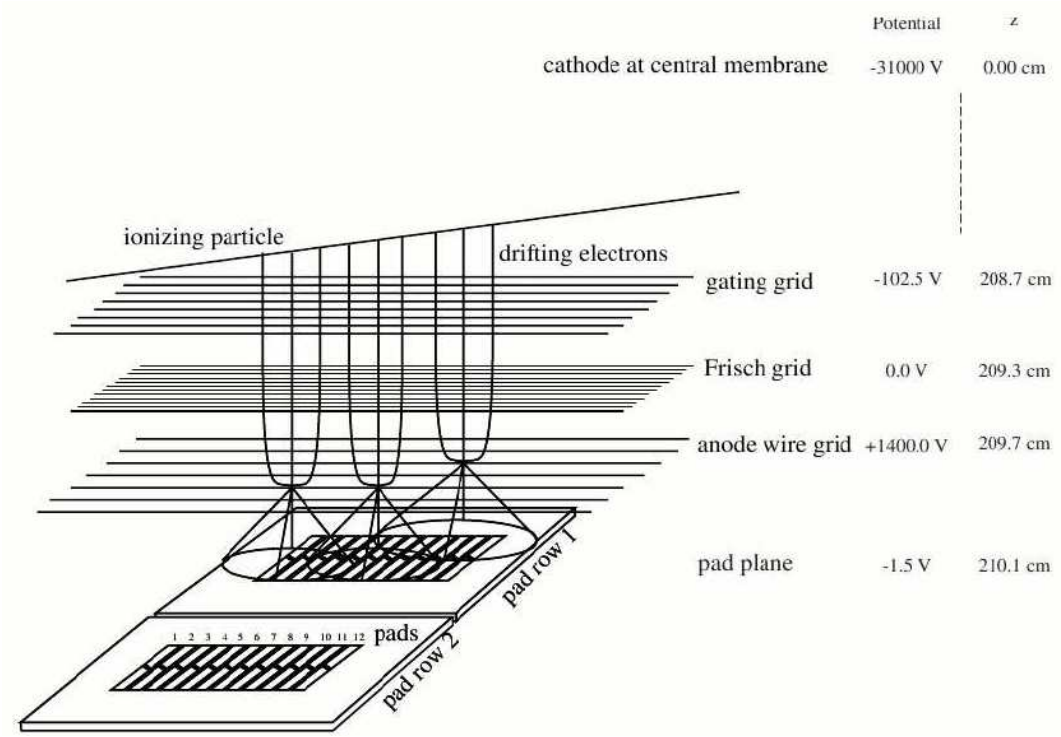

Figure 2.5: Electron drift and signal amplification principle in the TPC. The values on the right hand side for the potential and the distance to the central membrane z are typical values for the outer sector of the STAR TPC.

The readout pads are divided into 12 super sectors on each TPC side. Each super sector is divided into an inner and an outer sector (Fig. 2.6.). Each inner sector contains a large number of small pads, distributed in 13 pad rows, to maximize the position and two-track resolution in a region with high particle density. The pads of the outer sectors are densely packed in 32 rows per sector to optimize the measure of energy loss by ionization in a region with lower particle densities.

The signals induced in several adjacent pads allow to identify the position where the particle ionized the gas. For each collision, each pad is read 512 times, giving the time information that allows to determine the distance covered by the drifting cloud. The drift velocity is known and is equal to 5.4 cm/μs. Putting the spatial information together with the time information, it is possible to reconstruct point by point the trajectory of a charged particle across the TPC volume.

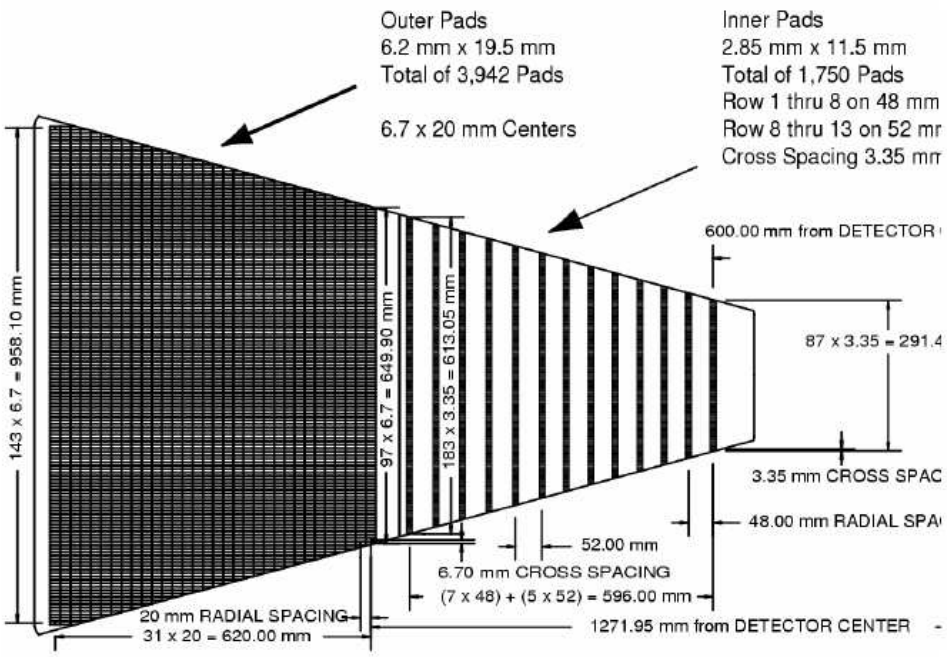

Figure 2.6: The anode pad plane with one full sector. The inner sub-sector has small pads arranged in widely spaced rows for a better two-particle resolution. The outer sub-sector is densely packed with larger pads for a better energy resolution.

The TPC also allows to identify particles via the specific energy loss, which can be calculated using the Bethe-Bloch formula:

$$\frac{dE}{dx} = -\frac{2\pi N_A z^2 e^4}{mc^2\beta^2}\{\frac{\rho Z}{A} ln\frac{2mc^2\beta^2 E_M}{I^2(1-\beta^2)} - 2\beta^2\} \tag{2.1}$$

In this formula, the properties of the particle are its charge z and its velocity β. Z, A, ρ and I are the atomic number, the mass number, the density and the specific ionization of the drifting gas respectively. E_M is the maximum energy transfer in one interaction. The other constants are the mass m of the electron, the charge e of the electron, the speed of light c and the Avogadro number N_A [112]. The particle can be identified by its momentum dependence on the specific energy loss.

2.3.2 Forward TPC

The FTPC was constructed to extend the acceptance of the STAR experiment, covering $2.5 < |\eta| < 4$ and $\Delta\phi = 2\pi$. The increased acceptance improves the general event characterization in STAR and also allows the study of asymmetric systems such as pA collisions. A schematic view of the FTPC is shown in Fig.2.7. The FTPC is a cylindrical structure of 75 cm in diameter and 120 cm long. It has a radial drift field and readout chambers located in five rings on the outer cylinder surface. Each ring has two pad-rows and is subdivided azimuthally into six readout chambers. An $Ar/CO_2(50\%/50\%)$ mixture is selected as the working gas. A laser calibration system serves to calibrate the drift velocity and correct for spatial distortions. The ionization electrons are

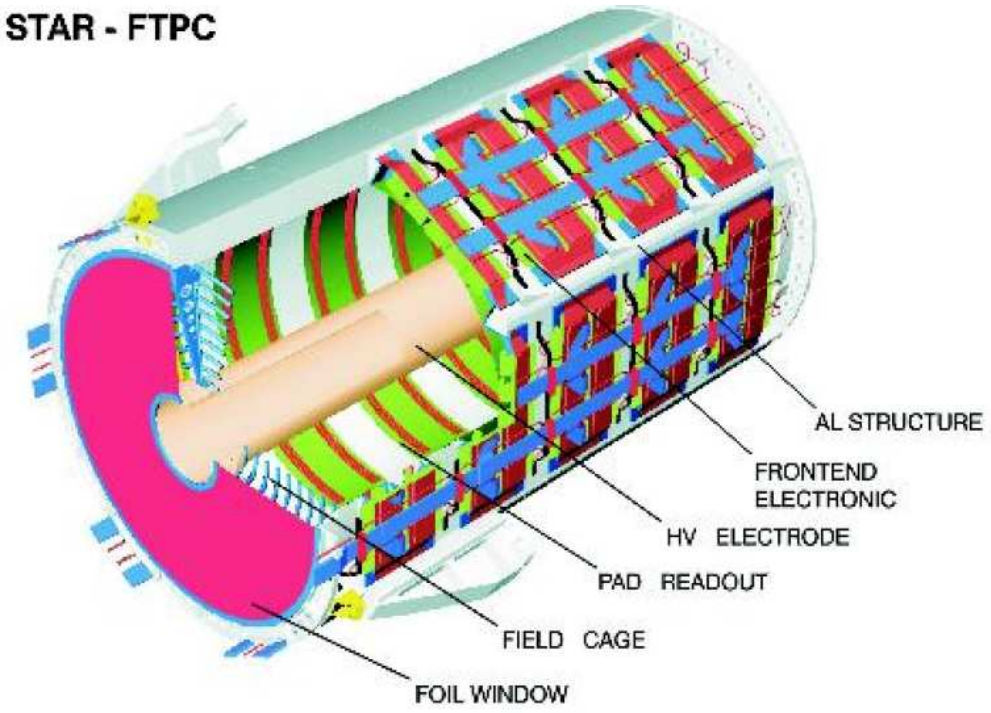

Figure 2.7: Schematic diagram of FTPC

drifted radially to the anode sense wires. Then induced signals on the adjacent cathode surface are read out by part of the 9600 pads in total. Up to 10 position measurements per track are used to fit the momentum.

2.3.3 Barrel Electromagnetic Calorimeter (BEMC)

The BEMC is STAR's major detector for measuring electromagnetic signals. BEMC being a fast detector, STAR utilizes the detector to trigger on, and study, rare and high p_T processes such as jets, leading hadrons, direct photons, and heavy quarks. It also provides a large acceptance for measuring photons, electrons, π^0 , η, ρ^0 and Z mesons in systems spanning from polarized p + p through Au+Au collisions. Fig. 2.8 shows the side view of a STAR BEMC

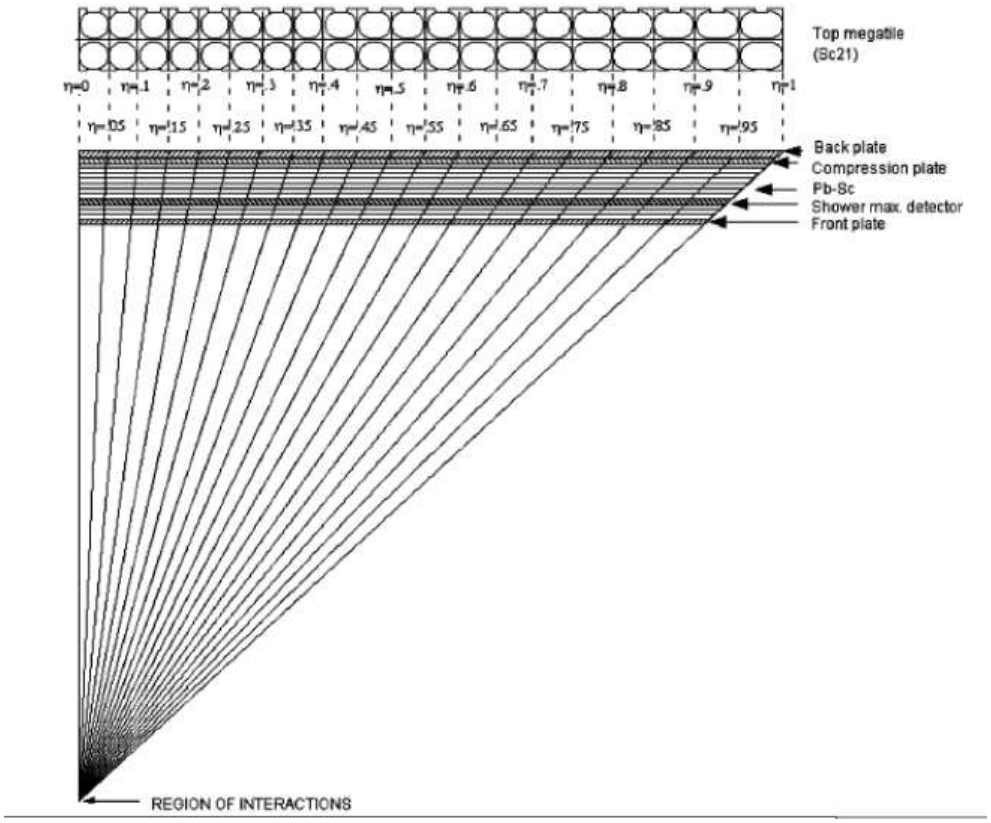

Figure 2.8: Side view of a calorimeter module showing the projective nature of the towers.

module. The STAR BEMC is a lead-scintillator sampling calorimeter. It covers -1$\geq \eta \leq$1 and 2π in azimuth. The front face is at a radius of 220 cm from and parallel to the beam axis. The design includes 120 calorimeter modules, each subtending 6^0 in $\Delta\phi$ and 1.0 unit in $\Delta\eta$. Modules are mounted 60 in ϕ and

by 2 in η. Each module is segmented into 40 towers, 2 in ϕ and 20 in η, with each tower subtending 0.05 in ϕ by 0.05 in η.

Figure. 2.9 shows the side view of a STAR BEMC module. It consists of a lead- scintillator stack and a Shower Maximum Detectors (SMD) situated at approximately 5 radiation lengths (X_0) from the front of the stack. There are 20 layer each of 5 mm thick lead, 19 layers each of 5 mm thick scintillator, and 2 layers each of 6 mm thick scintillator. The latter thick ones are used in the preshower portion of the detector.

The Barrel SMD detector is used to provide fine spatial resolution in the BEMC which has towers of significantly lower granularity compared to an electromagnetic shower. A STAR BEMC tower has a front-face size of $\sim$10 $\times$ 10 cm^2 at $\eta = 0$ and it increases towards $|\eta| = 1$. The high spatial resolution provided by the SMD is essential for π^0, direct γ, and electron identification. For example, the separation between two photons from the decay of a high-p_T π^0 can be smaller than the front-face dimension of a BEMC tower. They may hit the same tower, which by itself can not distinguish them, and we have to rely on the SMD. In this sense, the SMD significantly enhances the versatility of the STAR BEMC.

The SMD is a wire proportional counter-strip readout detector using gas amplification. Figure. 2.10 shows a schematic illustration of the STAR SMD. The unique feature of the STAR SMD is its double layer design. Two planes with strips etched in the η and ϕ directions allow reconstruction of a two-dimensional image of the shower as shown in the figure. There are a total of 36000 strips in the full detector and 120 wire channels. Each of the 1200 distinct areas, approximately 0.1 by 0.1 in $\Delta\eta - \Delta\phi$, has 15 ϕ strips and 15 η strips. So each SMD strip has a width of 0.0067 in $\Delta\phi$ and $\Delta\eta$ directions.

When a photon or an electron enters the BEMC, it creates an electromagnetic shower. The shower in the transverse direction develops on an average to its maximum $\sim$ at $5X_0$, whose position is measured by the SMD. As the shower travels through the BEMC tower, it loses energy in lead layers and is sampled in the scintillator layers, in which roughly 5% of the total energy is lost. Signals from each of the 21 active scintillating layers are read out with a wavelength shifting fiber, transferred and merged into a single photomultiplier tube (PMT). As a result, the signal magnitude at the PMT is proportional to the sampled fraction of the shower, which is proportional to the energy of the incident photon or electron. With a well calibrated gain controlled by the high voltage, the particle energy can be precisely measured. Hadrons within a certain momentum range usually deposit minimal ionizing energy into the

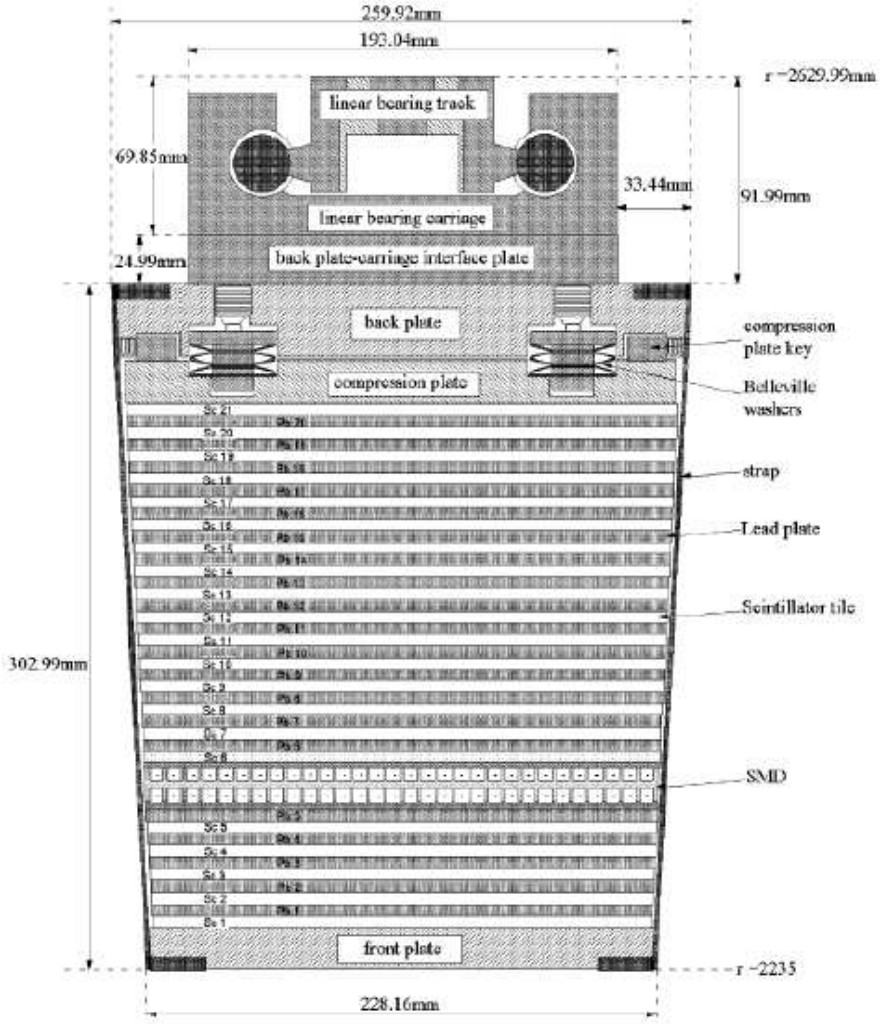

Figure 2.9: Side view of a STAR BEMC tower. The location of the two layers of shower maximum detector at a depth of approximately $5X_0$ from the front face at η=0 is also shown.

BEMC towers, which are known as Minimum Ionizing Particles (MIP), but they also possibly create hadronic showers and deposit significant amount of energy. The mean hadronic background energy in any given BEMC tower in a central Au+Au event is in the order of 140 MeV/tower with a standard deviation of 170 MeV. Energy loss from electrons and MIPs are two major points used to calibrate the BEMC towers. High voltage of each tower is adjusted according to the calibration from early runs and fixed in the remaining

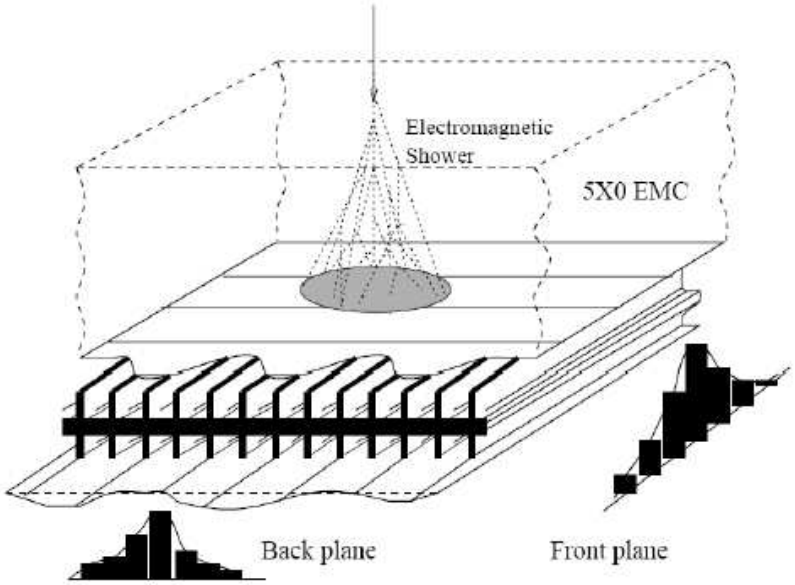

Figure 2.10: Schematic illustration of the double layer STAR BEMC SMD.

time of the data collection, so that the size of the MIP signal in each tower will be roughly the same. Layer by layer tests of the BEMC optical signal, and full system tests with cosmic rays and the test beams show that on an average 3 photoelectrons per MIP per calorimeter layer are produced from the fully integrated optical system. For these photostatistics, the resolution of an ideal sampling calorimeter is expected to be $\approx 14\%/\sqrt{E}$ plus a 1.5% constant term added in quadrature. In a real sampling calorimeter, transverse and longitudinal non-uniformities within a tower, and cross talk between towers, are the causes for this limiting resolution. The measured resolution is roughly $16\%/\sqrt{E}$ plus 1.5% .

2.4 Trigger

Most of the STAR detectors are too slow to be used for triggering applications. The bunch crossing rate is almost 10MHz, which means that the trigger detector should be ready every 107 ns. ZDC, BBC, and CTB are suitable for the purpose [113, 114].

2.4.1 Zero Degree Calorimeter (ZDC)

ZDC is located at about 18 m from the interaction point, on both sides of the collision point. It is designed to detect spectator neutrons emitted in the collision within a cone of $\theta < 2$ milli-radians around the beam axis. Each ZDC consists of three modules. Each module consists of a series of tungsten plates alternating with layers of wavelength shifting fibers that route Cherenkov light to a photo-multiplier tube. The energy measured by the ZDCs is proportional to the neutron multiplicity, which is known to be correlated with the event geometry and can be used to measure the centrality of the collision. However, in this analysis the ZDC is used only as minimum bias trigger in dAu collisions, requiring at least one neutron detected along the gold direction. The acceptance of this trigger corresponds to 95±3% of the total dAu geometric cross section.

2.4.2 Beam-Beam Counter (BBC)

The STAR Beam-Beam Counters consist of large and small hexagonal scintillator tiles. They are mounted around the beam pipe on the East and West sides outside the pole-tip of the STAR magnet at ±3.7 m from the interaction point. A ring with inner and outer radii of 9.6 cm and 48 cm is fully covered by the array of 18 small hexagonal tiles, corresponding to the pseudorapidity region of $3.4 < |\eta| < 5.0$. The ring between 38 cm and 193 cm, corresponding to a pseudorapidity region of $2.1 < \eta < 3.6$ is covered by the 18 large tiles. The BBCs mainly provide a minimum bias trigger for p+p collisions. In AuAu collisions, the many mid-rapidity tracks and spectator neutrons can be used as trigger, but these signatures are absent in p+p collisions. A coincidence in at least one of the 18 small BBC tiles on both sides provides a trigger for pp collisions. The difference in the time of flight between the two sides of the BBC's gives also information on the interaction vertex position. Large values in time of flight are associated with the passage of beam halo and, as a consequence, the corresponding trigger is rejected.

2.4.3 Specialized trigger

Most trigger detectors are used to measure global event properties, like multiplicity, the event vertex or just the occurrence of a minimum-bias event. This allows unspecialized datasets that are suitable for almost all the analysis

but not sufficient for any special type of analysis involving rare signals. The triggers based on preferences on selecting rare probes are very useful which dramatically reduce storage and offline processing requirements.

For some signatures, BEMC and EEMC triggered datasets with specific conditions are highly useful. A trigger is defined as high tower (HT) containing at least one BEMC/EMC tower above specified ADC threshold (E_T threshold). In pp collisions, a jet patch trigger above a threshold is also used to select events with high-energy jet. There are also complex triggers to select hard processes like high-energy jets, J/ψ or Υ production. In our analysis we have used high tower data for selecting di-jet events containing a π^0 in an event.

Chapter 3

The Photon Multiplicity Detector (PMD) for ALICE experiment at LHC

The Photon Multiplicity Detector (PMD) installed in the ALICE experiment at CERN detects photons event by event. The speciality of PMD is that it covers the forward region of the psudorapidity space. Historically PMDs have been used in WA93 [115] and WA98 [116] experiments at the CERN-SPS and are currently in operation in the STAR [117] experiment at BNL and the ALICE [118] experiment at CERN. The detector has been modified significantly in terms of the detection technology i.e, scintillator detector in WA93/WA98 has been replaced by the gas proportional chambers in ALICE (unit cell size $0.22cm^2$) at LHC.

The physics goals of PMD in ALICE are as follows :

1. **Multiplicity Distributions :** Determination of the multiplicity distributions of photon as a function of the centre of mass energy of the collisions.

2. **Elliptic flow :** Probing thermalization via studies of azimuthal anisotropy of photon at the forward rapidity which can be related to the elliptic flow.

3. **Charged-neutral Correlations :** Measurement of a signal of the chiral-symmetry restoration (e.g. the formation of the disoriented chiral

condensates) through the event by event measurement of charged-particle multiplicity (N_{ch}) in a common phase space as of photon multiplicities (N_γ) and study of the observable N_γ/N_{ch} over varying azimuthal coverage.

4. **Fluctuations :** Exploration of the critical phenomena near the phase boundary leading to an enhanced fluctuation in global observables like multiplicity and pseudorapidity density of photons.

PMD is a preshower detector with fine granularity and full azimuthal coverage covering the pseudorapidity region of $2.3 < \eta < 3.9$. Present work describes the fabrication, testing and simulations of the ALCE-PMD. The work consists of understanding the performance of the detector both in hardware and simulations. We discuss the hardware details including fabrication, cooling arrangement and testing in sections 3.1, 3.2 and 3.3 respectively. The simulation details of the response of the detector in pp collisions at $\sqrt{s} = 14$ TeV are discussed in section 3.4.

3.1 PMD : Fabrication and testing

3.1.1 Principle of Photon Detection

The basic principle of photon detection using PMD is similar to the one used in WA93 [115] and WA98 [116] experiments at the CERN SPS. PMD consists of two highly granular sensitive detector planes known as the Charged Particle Veto (CPV) and preshower plane. When viewed from the colliding point, the preshower plane[1] is placed behind a lead converter of three radiation length thickness. The principle of a preshower detector is schematically depicted in Fig. 3.1. A photon produces electromagnetic shower while passing through the converter. These shower particles produce signals in several cells of the sensitive volume of the detector. Charged hadrons mostly affect one cell and produce signals resembling those of the minimum ionizing particles (MIPs). The thickness of the converter is optimized to three radiation length so that the conversion probability of photons is high and the transverse shower spread is comparatively small to minimize the shower overlap in a high multiplicity environment. The CPV plane is a sensitive plane of similar granularity as of preshower plane and placed in front of the converter to veto the charged

[1]preshower plane often used as PMD-plane

particles which improves the discrimination between charged hadrons and photons. The unit detector cells in both the sensitive planes are gas proportional detectors of hexagonal boundaries.

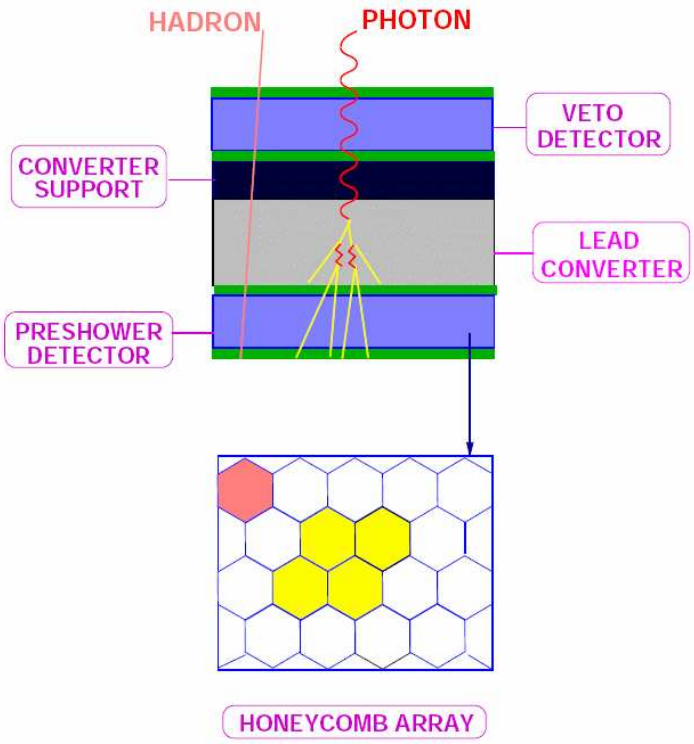

Figure 3.1: The schematic of the principle of a preshower detector for photon detection.

3.1.2 Detector Components

ALICE PMD has modular structures, consisting of 48 gas tight enclosures known as "module" spreading uniformly over two planes. Each module consists of 4608 number of hexagonal detector cells called unit cell separated by copper walls. Fig. 3.2 shows the schematic representation of a unit cell, which is having a hexagonal boundary of cross sectional area of 0.22 cm^2 with a gas thickness of 0.5 cm. The anode wire passes through the center of the cell and the cell works in the proportional region with a gas mixture of argon and carbon-dioxide in

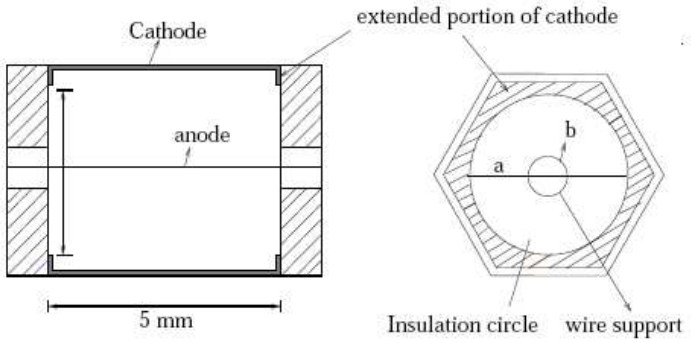

Figure 3.2: Schematic diagram of the cross section of a unit cell in longitudinal (left) and transverse (right) planes.

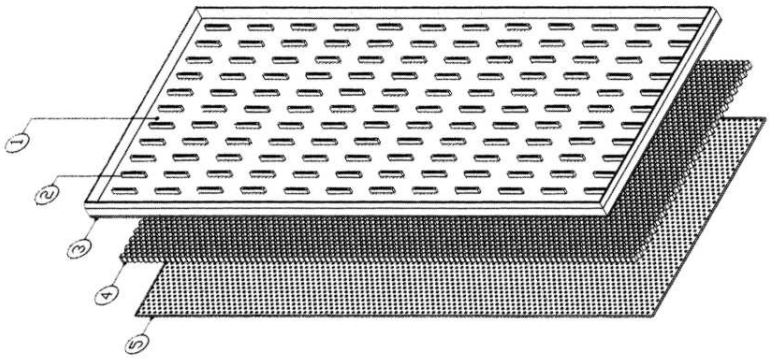

Figure 3.3: A schematic diagram of a unit module. The numbers shown are for 1)top Printed Circuit Board(PCB), 2)Flexible Printed Circuit (FPC) connectors, 3)Edge frame, 4)honey comb cells and 5)bottom PCB.

the ratio of 70 : 30 by mass. The detector consists of $\approx$ 200k cells arranged in arrays of rows and columns spread over *48* modules. The assembly of the cells in a *module* (48×96) is done in a gas-tight volume (enclosure) with an inlet and an outlet for gas-flow. Depending on the orientation of the hexagonal cells in rows and columns, the modules are named as long-type (LM) and short type (SM). Each of the detector planes, i.e, the Preshower (PMD) and the Charged Particle Veto (CPV) can accommodate upto 24 such modules. Details of the procedure of assembly and fabrications are given in [119]. We

have enlisted the detector parameters [120] in the table 3.1. In final data taking position of PMD, 40 modules are installed for the full scale operation covering $2.3 < \eta < 3.5$ and full azimuth.

Parameters	*Values*
Technology	Extended cathode
Number of planes	veto + preshower
Distance from vertex	361.5 cm
η-coverage	2.1-3.7
Active area	$2m^2$
Cell cross-section	0.22 cm^2
Cell depth (gas depth)	5mm
No. of readout channels	182,000
No. of modules	48
No. of cells in a module	4608
No. of HV channels	48
Thickness of Pb-converter	1.5 cm ($3X_0$)
Thickness of SS support plate	0.5 cm
Total weight	1200 kg

Table 3.1: Parameters for ALICE PMD.

3.1.3 High voltage testing of PMD Modules

We have conducted testing of the detector modules at VECC at the time of fabrication and again at CERN prior to installations. The testing at CERN is termed here as the second phase of testing. The setups made for testing at both phases are shown in Fig. 3.4. The testing procedure consists of following steps.

- The module is kept in gas flushing mode for ≈1 hour. The module is tested for gas leakage and repaired if needed. If no leakage current is found in the module, the module is kept in gas-flushing for a longer period of time.
- The module is kept with anode wires not connected to the electronics and tested for several hours with HV set at ∼1700 Volt for studying the increase of leakage current if any.

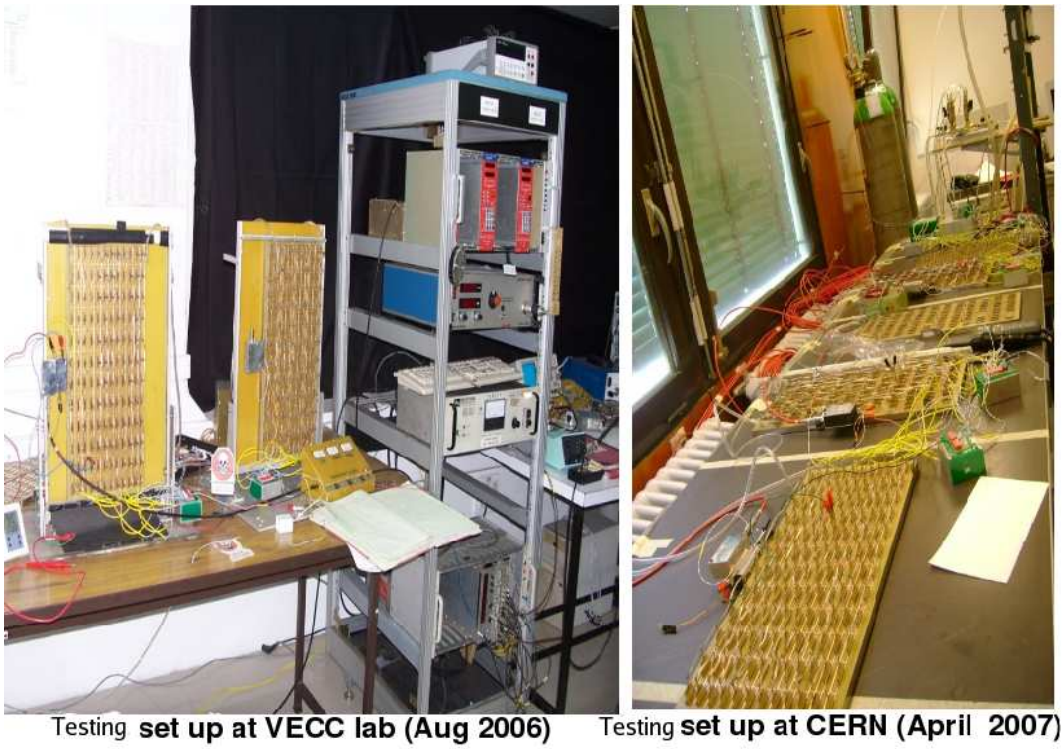

Figure 3.4: High voltage testing set-up for PMD modules.

- The anode wires are then connected to the ground through a "shorting connector". One shorting connector connects the anode wires of a zone of 32 cells. Group of cells showing higher leakage current are investigated further and disconnected, if needed.

There are three types of discharges observed (i) inside the cell, (ii) over the PCB surface and (iii) on the edge of the surface of honeycomb cathode.

The criteria set for testing the modules are, (i) leakage current per module $<$ 5 μA, and (ii) duration of discharge $<$ 1 sec. Fig. 3.5 summarizes module-wise leakage current, the number of cells disconnected in the second phase of testing and gas leakage performance.
Top Row : Modulewise leakage current where the plot on the left is for the short type modules and on the right for long type.
Middle Row : Status of the modules in terms of gas leak. Leaky modules are taken as one (1) and modules with no gas leak are taken as zero(0).
Bottom Row :Number of channels disconnected in the 2^{nd} phase of testing.

Short type modules suffer comparatively less number of cell loss in the test. The modules are certified as good for being stable at 1500 Volt for more than three hours with leakage current of $< 5\mu$A. It should be noted that the testing is a time consuming task and the second phase of testing of all the PMD-modules took about four months in total.

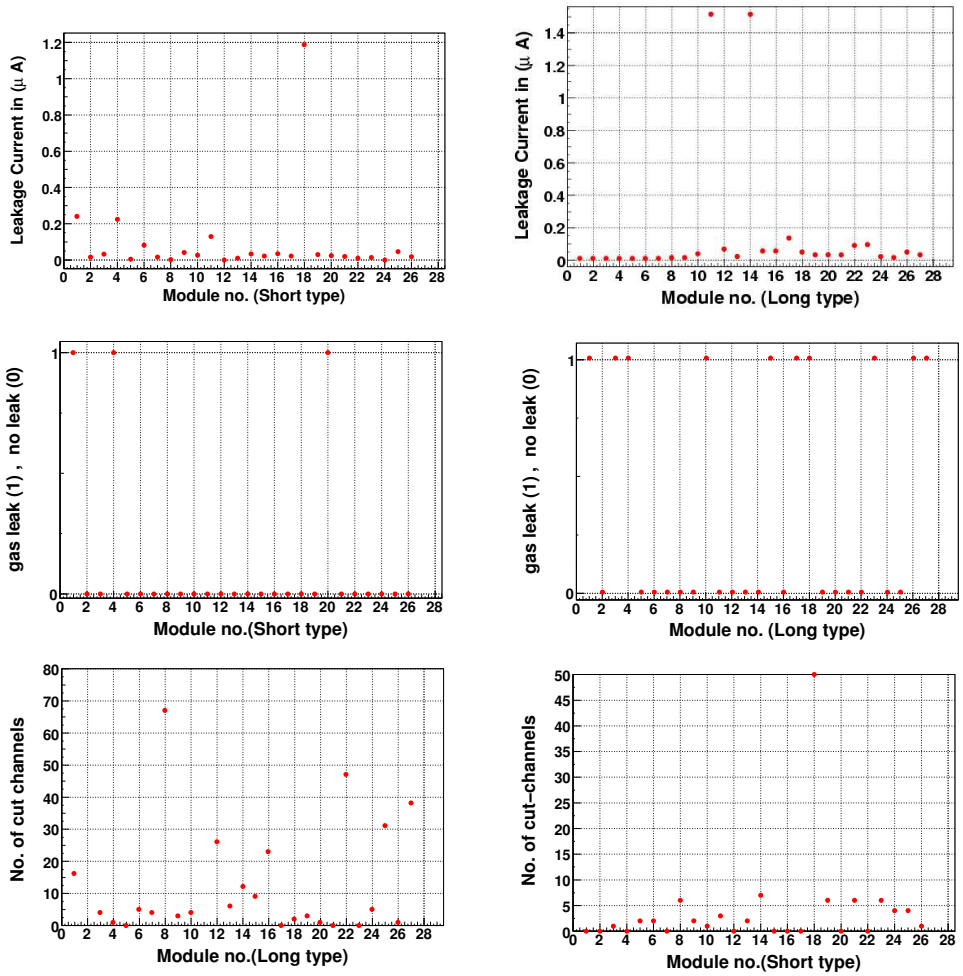

Figure 3.5: Summary of module-wise performance after HV testing prior to the installation. The plots in the panels are for i) *top-row :* the leakage current, ii) *middle-row :* the gas leak status and iii) *bottom-row :* statistics of disconnected channels for the long and the short type modules shown separately.

3.2 Cooling arrangement of PMD

High density readout front end electronic (FEE) boards are mounted on to the detector which dissipate significant amount of heat and a cooling arrangement is therefore necessary for keeping the temperature at an acceptable level. It should also be ensured that the heat is not thrown to other detector systems. To explore the possibility of setting up of a suitable arrangement for cooling

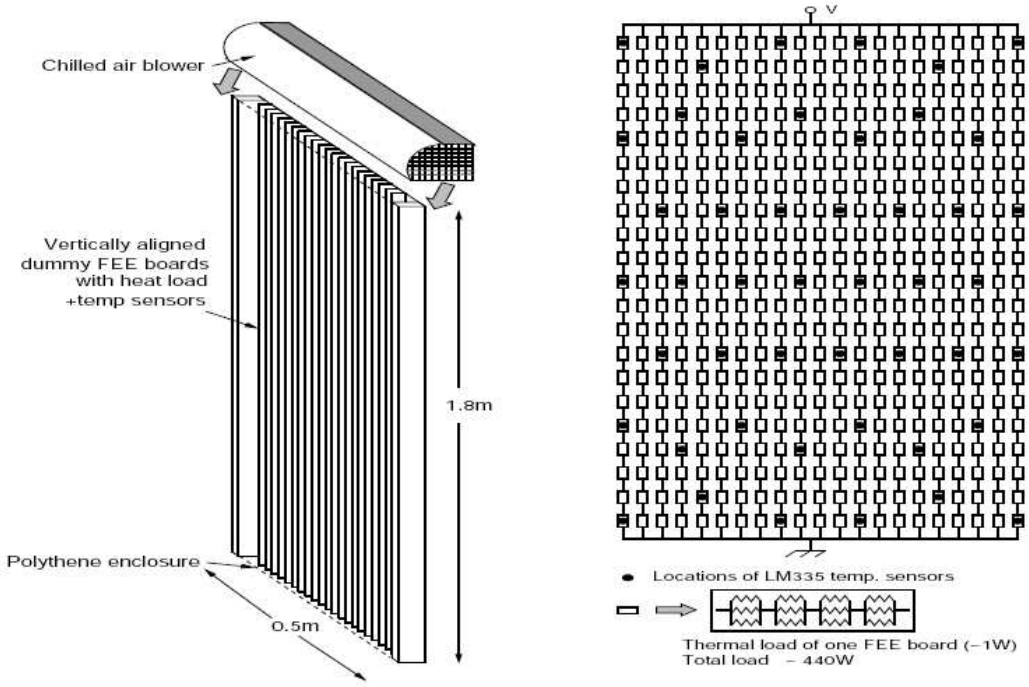

Figure 3.6: Left panel : Schematic representation of FEE board placement structure over the detector surface and the longitudinal passage of chilled air. Right panel : Placement of the dummy FEE boards and the temperature sensors.

the PMD modules, a prototype test has been carried out at VECC. The placement of the dummy FEE boards and the temperature sensors is shown in 3.6 and the dummy setup is shown in figure 3.7 (left). For efficient air flow in contact with the FEE boards, it is desired that all the boards are aligned in the same direction. The density of FEE boards on the PMD surface is also made uniform. This is expected to further help in uniform cooling and prevent the

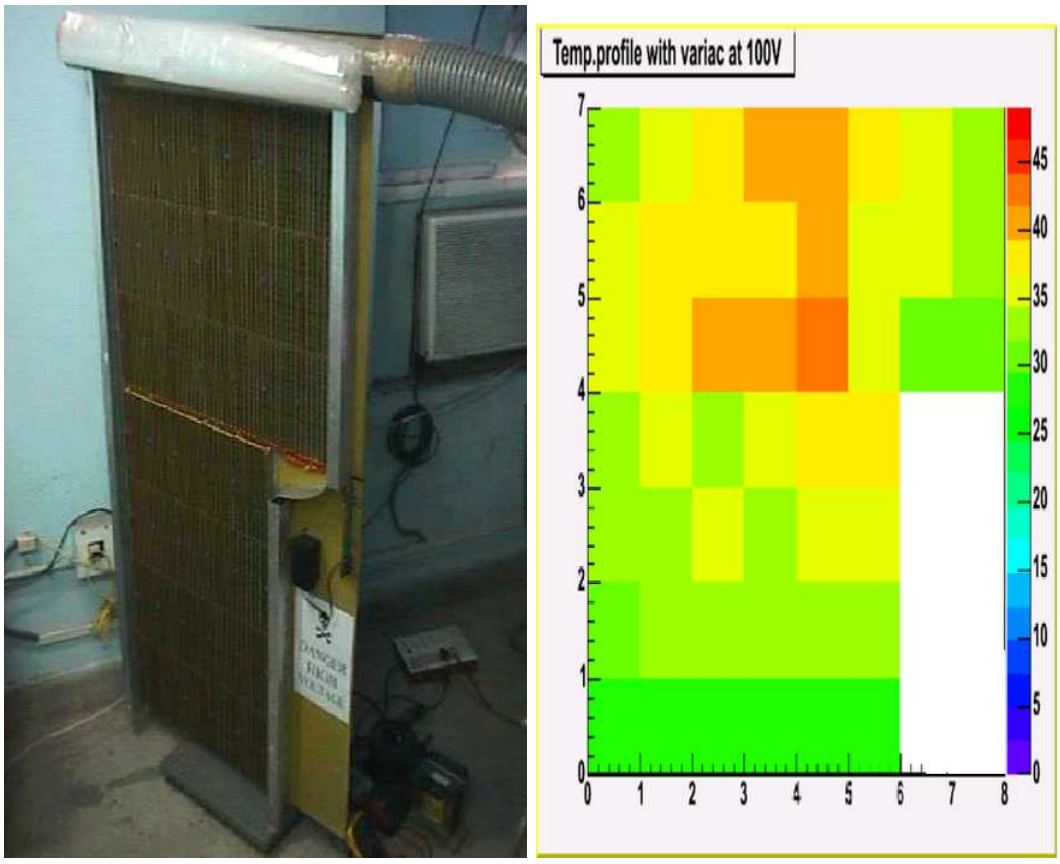

Figure 3.7: Left panel: Picture of the dummy quadrant without the cover sheet. Right panel: Temperature profile of the quadrant

formation of hot spots. Each half of the detector plane has 78 mm wide aluminum side walls. A thin copper-clad FR4 sheet is placed across these walls so as to form an independent shallow enclosure for the front-end electronics. Air ducts positioned on the top opening of these enclosures serve as entry points for forced air cooling. The ducts are baffled to reduce excess vibration due to turbulence.

A Quarter scale model

The feasibility of the above scheme has been tested by a quarter scale model of PMD. The heat load of a 64-channel FEE Board is expected to be approximately 1 watt. This power dissipation is simulated by a set of resistors on a similar sized dummy board. Such dummy boards were fixed on a backing panel

having 21 columns with the same spacing and inclination as in PMD modules. There were 24 FEE boards in each column. The height of this thermal mock-up was kept similar to the height of PMD. This is shown schematically in the left part of Fig. 3.7. Temperatures were recorded after a passage of time sufficient to attain an equilibrium. The temperature distributions over the detector surface was monitored which depends upon the air flow rate and the air passage configurations. Variations of air flow and heating were simulated by changing the fan speed through regulating the variac [2] voltages. In the absence of cooling, temperature of the FEE boards go up to 60^0 C within the enclosure.

Fig. 3.7 (right) shows the temperature profile for the variac voltage set at 120 Volt . The amount of air sucked as a function of variac voltage is shown in Fig. 3.8 (right). The temperatures of the inlet and the outlet air and the air volume is used to make an estimate that about 800 J/s heat is sucked out which remains constant as shown in Fig. 3.8 (left) above 120 Volt.

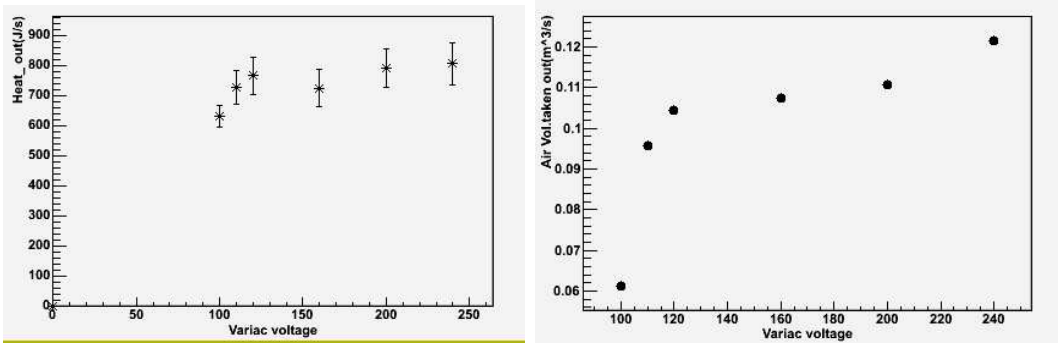

Figure 3.8: Top: Variation of the heat output as a function of the fan speed. Bottom: Heat taken out as a function of variac voltage

After studying the cooling arrangement with the above mentioned model, the required air suction at the inlet is found to be 0.4 m^3/sec to keep the temperature inside the enclosure well below the tolerable temperature of the chips. The temperature of the insulating cover is 2 to 3 degree celsius higher than the ambient temperature which is in the tolerable range for other detectors.

[2] a regulator for changing the fan speed used for air suction in cooling arrangement.

3.3 Test of PMD with pion and electron beams

Two prototypes having 96 cells each, with a cell cross sectional area of 1.0 cm^2 each and gas depths of 8 mm and 10 mm (referred to as Prototype-99-8 and Prototype-99-10, respectively) were used for early tests [119]. The testing were performed at CERN which had a dedicated facility for testing of the detectors in ALICE at the T10 beam line at the Proton Synchrotron (PS).

3.3.1 Objectives of the test-beam

The main objectives of the test-beam were as follows :

- To find out the operating voltage of PMD such that the detector operates in proportional region with an efficiency plateau at $> 95\%$.
- To study the response of the minimum ionizing particles (MIP) and the fired cell multiplicities by MIP.
- To find the cell to cell gain variation of detector module(s).
- To find the detector response to pions and their interactions in the lead plate of the detector.
- To study the cluster properties in the preshower plane.
- To obtain the calibration relation between the response in ADC from the test data and simulated energy deposition. This result is extensively useful to compare experimental and simulated results.

3.3.2 Test beam facility and test setup

A dedicated test beam facility for ALICE at the T-10 beam-line of PS at CERN was used for the purpose. We get electrons and negative pions of momenta varying from 1 GeV/c to 6 GeV/c in this beam area. Test-beam set up in the PS beam-line is shown in Fig 3.9. A Cherenkov detector is placed in front of the PMD for triggering on the electrons. Fig. 3.10 shows the schematic of the layout of various detectors in the test beam set-up. The trigger was defined by

a 5-fold coincidence using two pairs of scintillators placed upstream of PMD and a finger scintillator of dimension 3mm×3mm placed in front of the CPV plane. For the beam of pion to be defined in a straight line and to ensure its passage only through the centre of the selected area of 3mm×3mm (finger scintillator cross section) a five fold coincidence setup was essential. Since the fraction of electrons in the beam is quite low, we have used a 3-fold trigger for higher statistics of electrons.

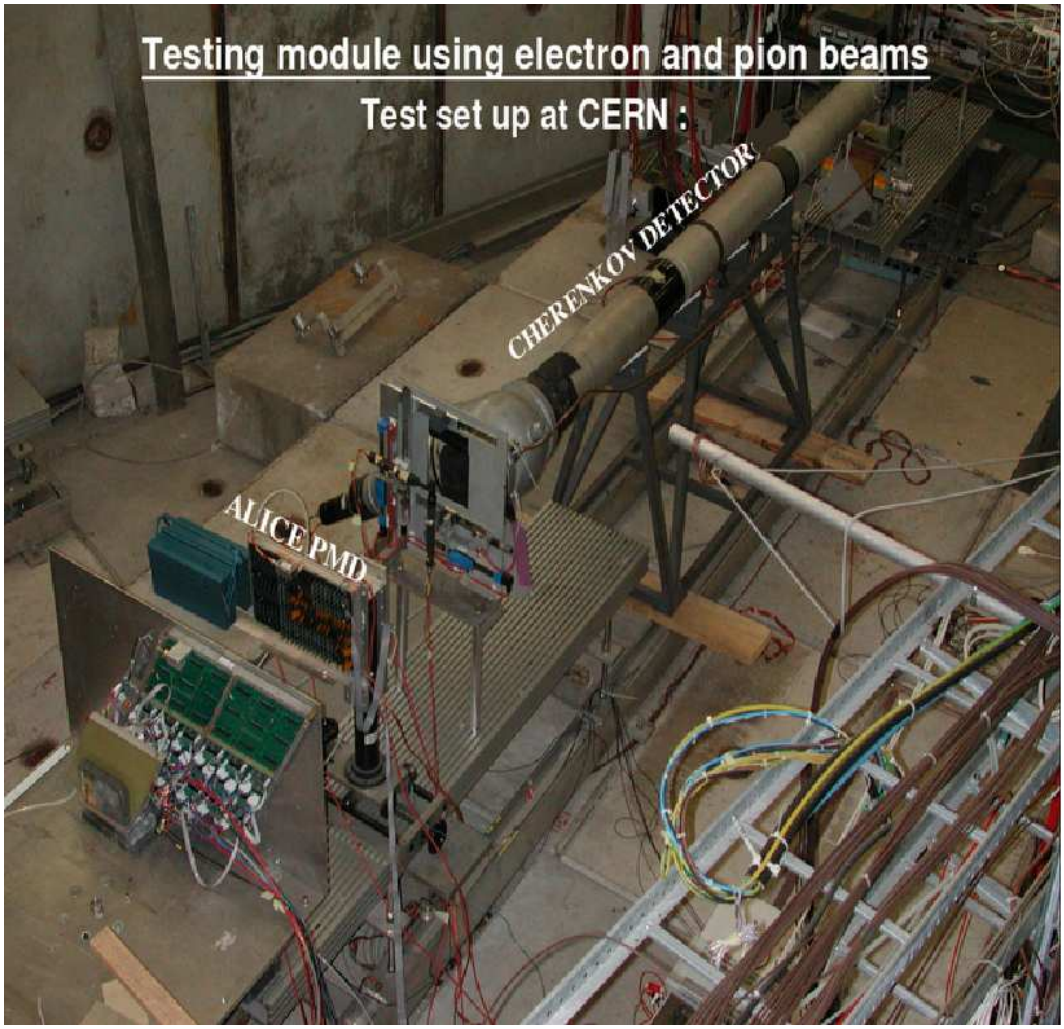

Figure 3.9: Test-beam setup at PS beam line.

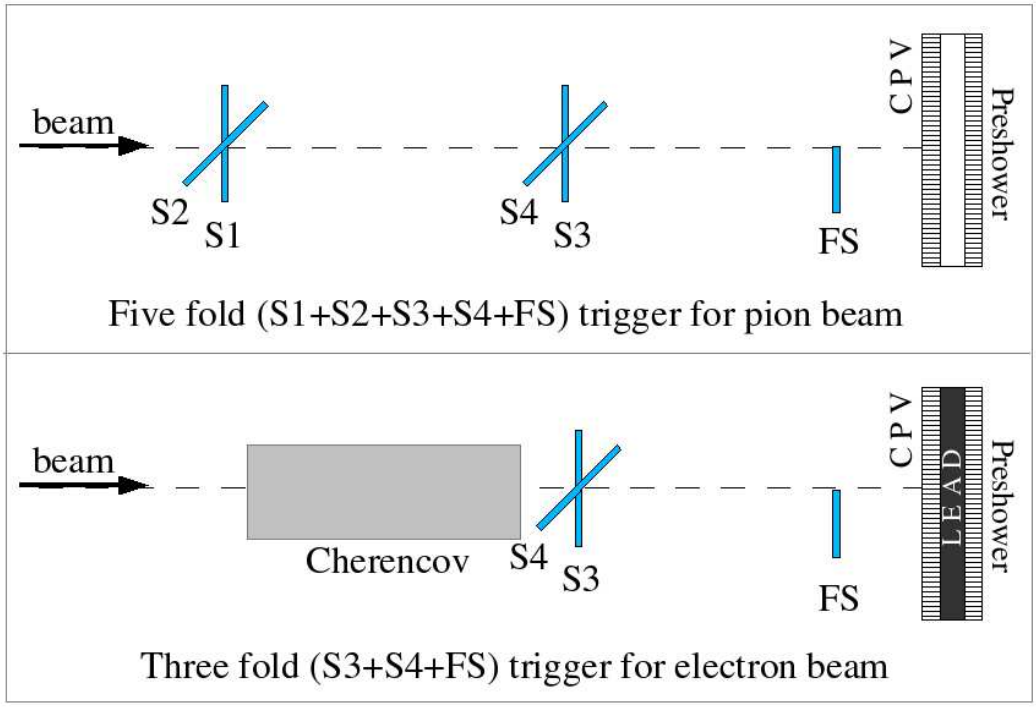

Figure 3.10: The schematic of the trigger setup with electron (bottom) and the pion beam (top) selection.

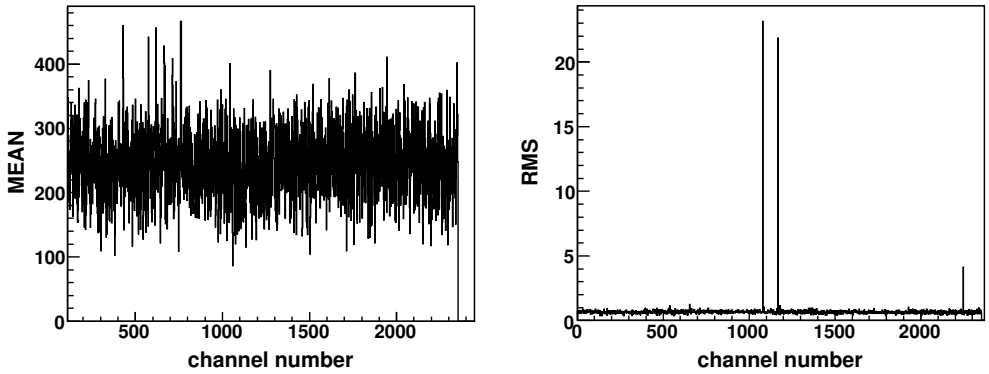

Figure 3.11: Mean and RMS distributions of the pedestals of all the channels in a module.

3.3.3 Pion beam results

Noise estimation in test beam

Due to various reasons, detector cells respond to noise from varying sources. It might be due to the response of an untriggered particle which still sustains at the time of charge collection of a trigger particle arriving in a narrow time window after the untriggered particle. It might also be simply an electronic noise which is expected to be removed at a high RMS cut on the pedestal. To reduce the number of cells firing by noise, we used a cut in the analysis such that the channel signal $>$ (pedestal mean + 5$\times$ RMS) threshold. A typical pedestal and RMS distributions of a module is given in Fig. 3.11 in the left and right panels respectively, where the X-axis represents the readout channel number corresponding to an individual cell of the module. The average pedestal comes out to be around 250 ADC with the RMS near to unity for good channels.

Cell-hit distribution due to pion

The transverse beam profile seen on PMD module has a distribution spanning over a number of cells. We put a constraint on the beam definition for the beam particles to be in a single line by triggering on coincidence of signals for scintillators from the S1, S2, S3, S4 and FS (Fig. 3.10). The "finger" scintillator (FS) had an area smaller than the active area of a cell. Therefore, by putting the finger over the center of a cell, we can count the number of pions falling in the cell precisely. Therefore the *efficiency* of detection of charged particle (π^-) can be calculated as the ratio of the pions detected to the number of incident pions. For obtaining the cell to cell gain variation, a data set with only two fold (S3,S4) coincidence level was used so that a large number of cells respond to the triggering on a large number of pions falling on the detector. This situation might be similar to the situation in the real experiment, where the particles produced in the collisions are not likely falling perpendicular but is distributed uniformly over the detector with angles spreading over a wide range. Fig. 3.12 shows the lego plot for the distribution of the hit cells on the CPV and the preshower sides without lead converter in position. Preshower module is having mostly single cell hit as the finger is adjusted to the center of a preshower-cell. Since the CPV and the PMD side modules do not lie exactly back to back, the finger area is shared by three cells on the CPV plane. As a

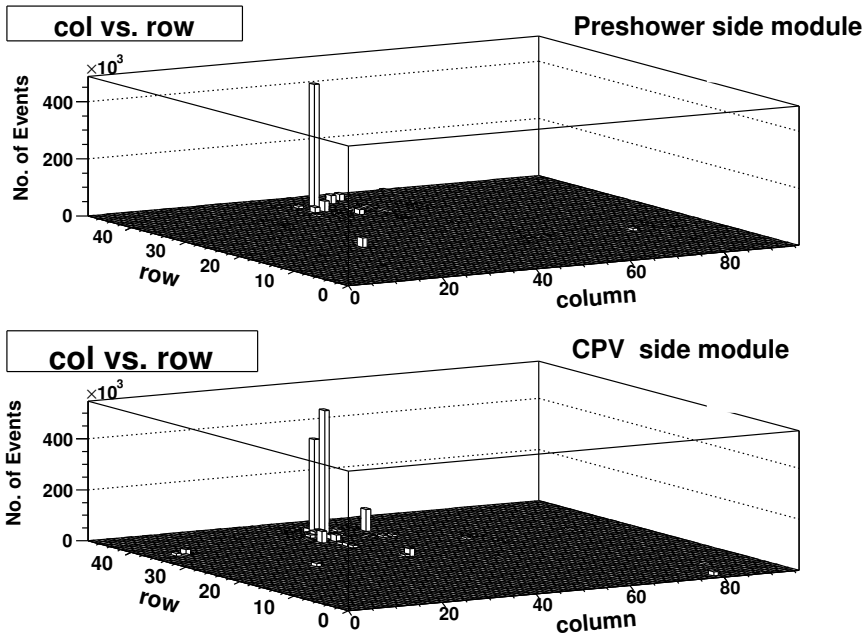

Figure 3.12: 2D distributions of hit cells due to triggered pions incident on two modules placed back to back with no lead converter in between.

result, the lego plot shows one major cell with two neighboring cells appearing prominently for the CPV-side module.

Operating voltage

The response of the detector to incident charged pions was studied using a 5 GeV/c pion beam. Since we are using pion beams in the relativistic range, they ionize the gas depending upon the thickness of the gaseous medium while traversing through the detector and they can be considered as, Minimum Ionizing Particles (MIPs). Typical pulse height spectra for a 5 GeV/c pion beam are shown in fig 3.13 along with fits to Landau distribution for a wide range of operating voltage. It is seen that the value of mean, most probable value (MPV) and RMS of the distributions increase with the high voltage. The distributions are obtained by making clusters by adding central cell to the nearest neighburing cells. In Fig. 3.13 clear Landau type distributions are visible starting from 1200 to 1400 Volt. Fig 3.14 gives the average cluster size due to pions. The average cell multiplicity for pions being close to unity

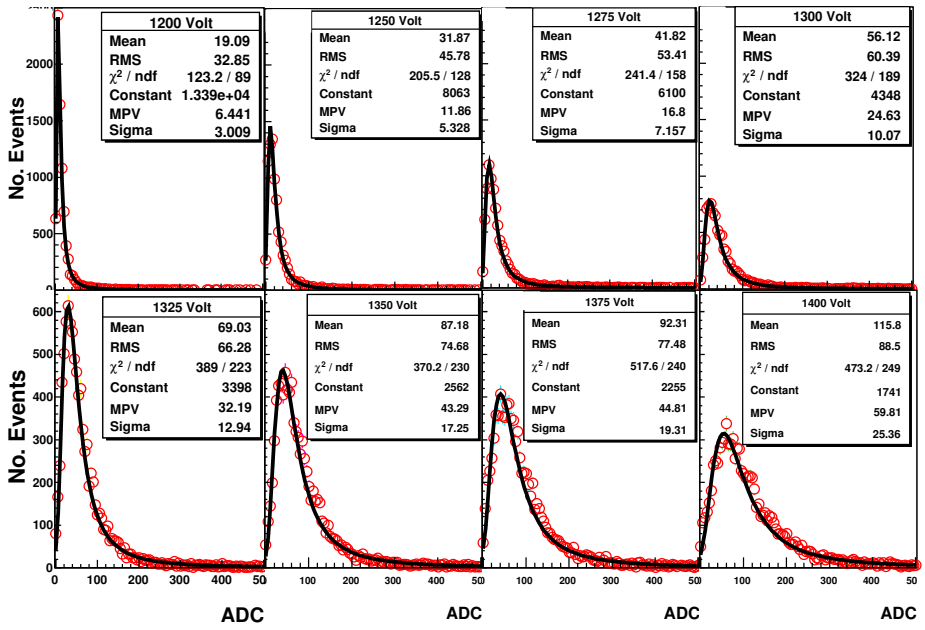

Figure 3.13: Spectra of the ADC distributions of a particular module due to MIP at various operating voltages.

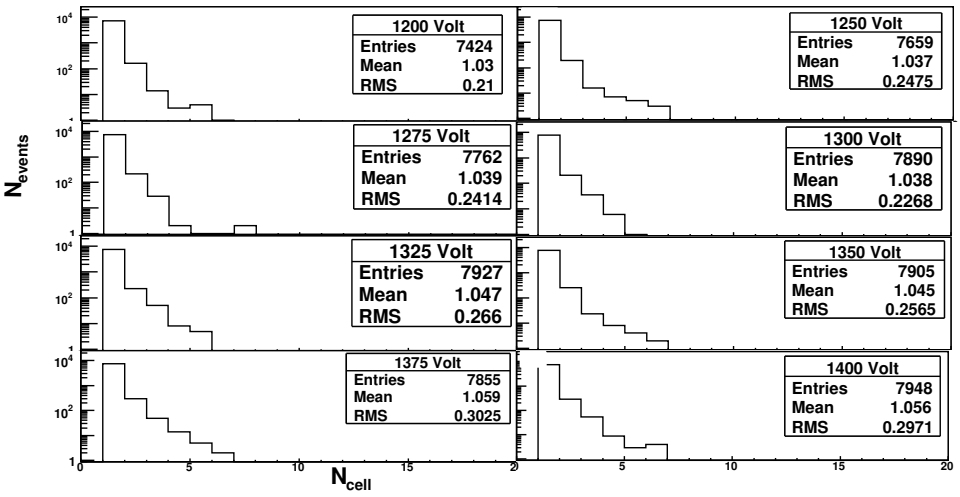

Figure 3.14: Cluster size distributions in terms of the number of hit cell due to single pion. Mean cluster size $\sim$ 1 cell.

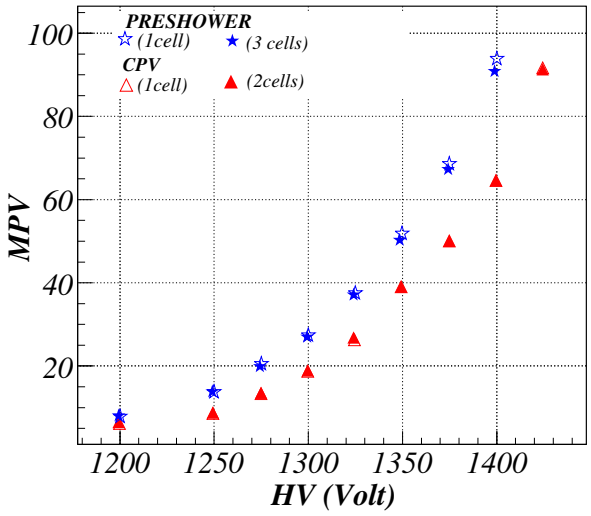

Figure 3.15: Variation of the MPV with the applied Voltage. 1-cell indicate the result from the cell fired largest time, 2-cell indicates the inclusion of the next frequent hit cell and so on for 3-cell.

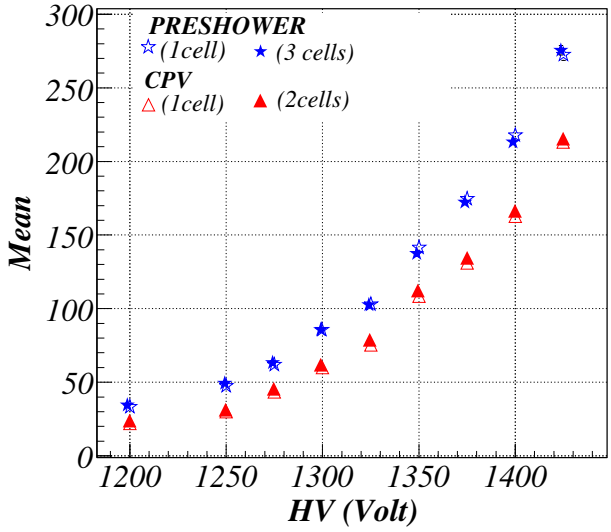

Figure 3.16: Variation of the MEAN of the MIP distributions with applied Voltage.

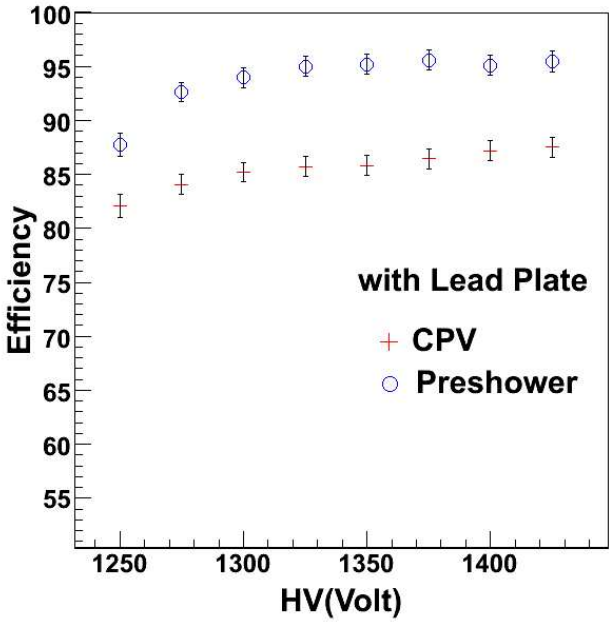

Figure 3.17: Variation of efficiency with detector voltage for two planes.

suggests that the π^- signal is confined to mostly one cell, satisfying one of the basic requirements of the detector. The variation of the most probable value (MPV) of the fitted Landau distribution and the mean of the MIP spectra with operating voltage are shown in Fig. 3.15 and Fig. 3.16 respectively. Detector efficiency increases with the applied voltage as shown in fig 3.17. At 1300 Volt, the efficiency of the preshower plane is $\approx$ 95 %, the plateau region suggests that the operating voltage of 1300 V is safe to use with maximum efficiency. The plateau of the CPV-side module is low due to the effect of the pions falling in the dead region of the detector which reduces efficiency by $\approx$ 15 %. It is better to use the detector at lower operating voltage because the detector is more prone to spark at a higher voltage and the effect of saturation is minimal at lower voltages.

Saturation of the ADC distribution

The electronics used for PMD has a dynamic range extending upto about 300 fC with a gain of approximately 4 mV/fC. Sometime the secondary ionization

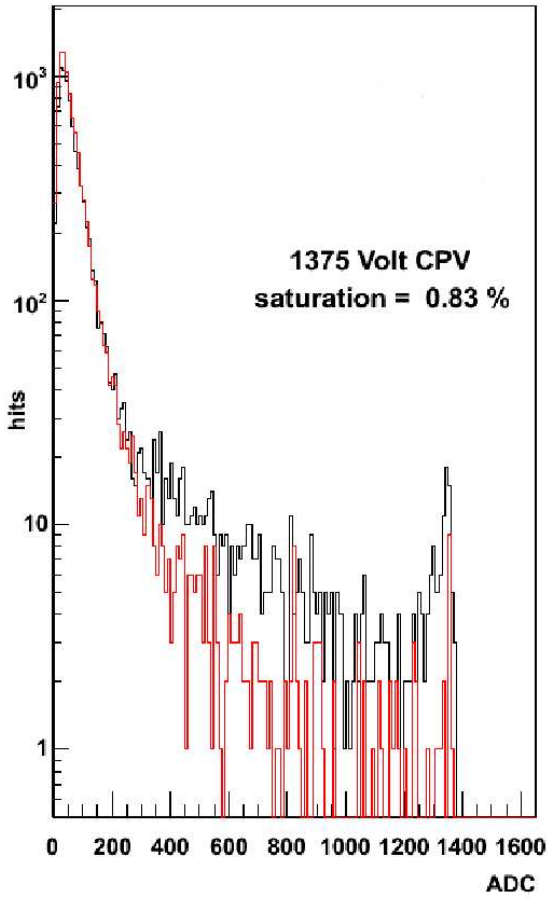

Figure 3.18: Saturation with (black) and without (red) lead converter for 5 GeV π^- beam.

inside the cell is large and gives signal outside the dynamic range. In such a case there will have truncation in the signal at ≈1600 ADC channels. Therefore the pedestal subtracted data will show saturation. This will be more prominent at a higher operating voltage. In case of electron data, the shower profile makes the central cell of the cluster to encounter multiple charged particles. This lead to saturation of the central cell of the cluster more frequently. The Fig. 3.18 shows the saturation effect for 5GeV pion beam. The saturation is more prominent in presence of lead due to the hadronic shower formation (10% of the events), a case mimicking electron, where the central cell is encountered with multiple hits from the electromagnetic shower particles.

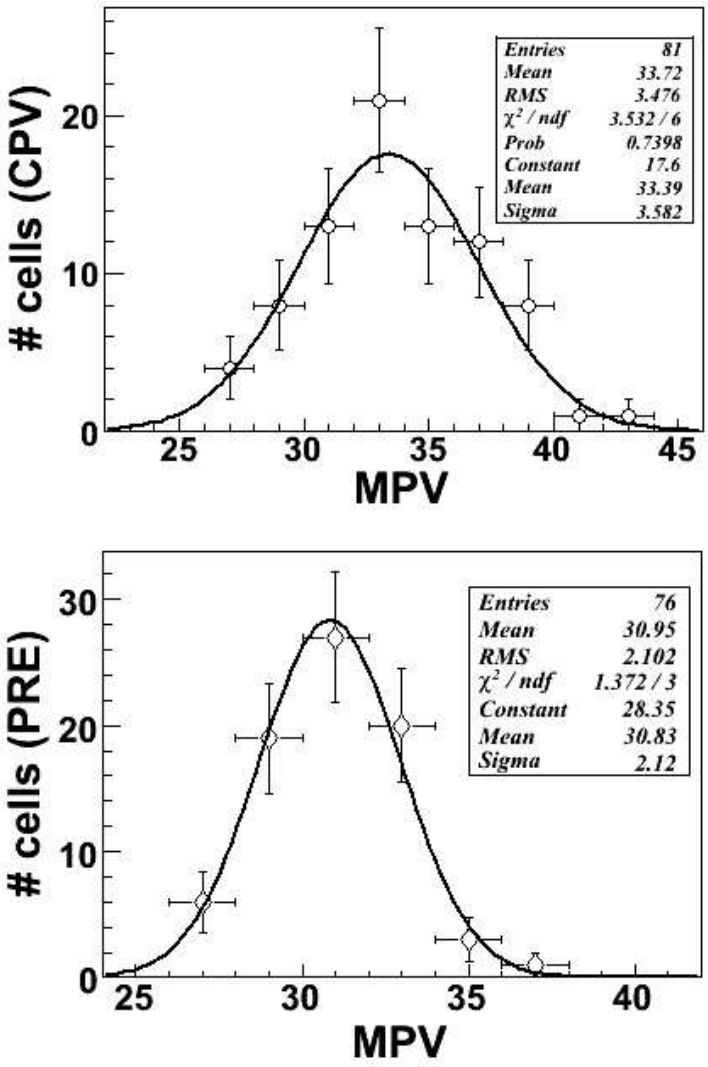

Figure 3.19: The distribution of the MPV values of the Landau fitted MIP distributions for 81 cells in the CPV side module (top) and for 76 cells in the preshower side module (bottom).

Cell to cell gain variation

The response-gains of all the cells in a module are not uniform. Wide beam is triggered with S1 and S2 trigger combination and the ADC distributions of the cells are fitted with landau distributions. Fig. 3.19 shows the distribution

of the MPV of the Landau functions fitted to the MIP distributions for 81 cells in CPV side module and 76 cells in preshower side module. The distributions is gaussian with mean at 33.39 and 30.83 ADC for CPV and PMD sides respectively. It can therefore be concluded from the σ of the fit that there is at most ≈ 15 % variations in cell to cell gain. Observed differences in mean MPV in two planes can be seen to be within the obtained cell to cell gain variations in two cases.

3.3.4 Electron beam results

PMD is to detect photons with energy starting from a few hundred MeV to several GeV. Electrons like photons, produce electromagnetic showers in the convertors. In simulations, energy loss by particles in lead as recorded in GEANT is expressed in terms of keV but in data we have the output in terms of ADC channels. It is therefore necessary to have a calibration relation between the two for converting simulations to data and vice versa. Energy depositions over a wide range is measured using the incident electrons. The analysis shown here is for 2006 test-beam data. In PS run, electrons were fired at 2, 3, 4, 5 and 6 GeV energies. PMD modules were biased with 1375 Volts and 1400 Volts for these sets of energy.

Calibration curve

Analysis shown here is done for 1400V data with 2, 3 and 6 GeV (4 and 5 GeV beams had large pion contaminations) electrons. For analysis of test data we need to devise a procedure for removal of noise. The number of cells in a module above a threshold is obtained for each event and it is expected that the cell multiplicities will reach a constant value after the reduction of noise. It has been found from preliminary observation that there is a large number of clusters in an event which might arise from noise. Firstly, a flat cut of 30 ADC has been used in the cell level. This helped in reducing the number of clusters and thereby reduces the unwanted signals.Pions in general produce hadronic shower at 10% level in the lead convertor. Therefore if electron samples are contaminated with pions, they will produce mostly single cell cluster for the case of contamination. This has been taken care of by considering the clusters consisting of more than one cell for further analysis. Following information are obtained for different electron energies with $3X_0$ lead thickness.

1. Finding the number of clusters per event (one cluster is taken as connected cells in an event.)

2. Selection of the main cluster and finding the number of cells in the main cluster, the fraction of ADC in the main cluster.

3. Finding the average ADC deposition in the main cluster.

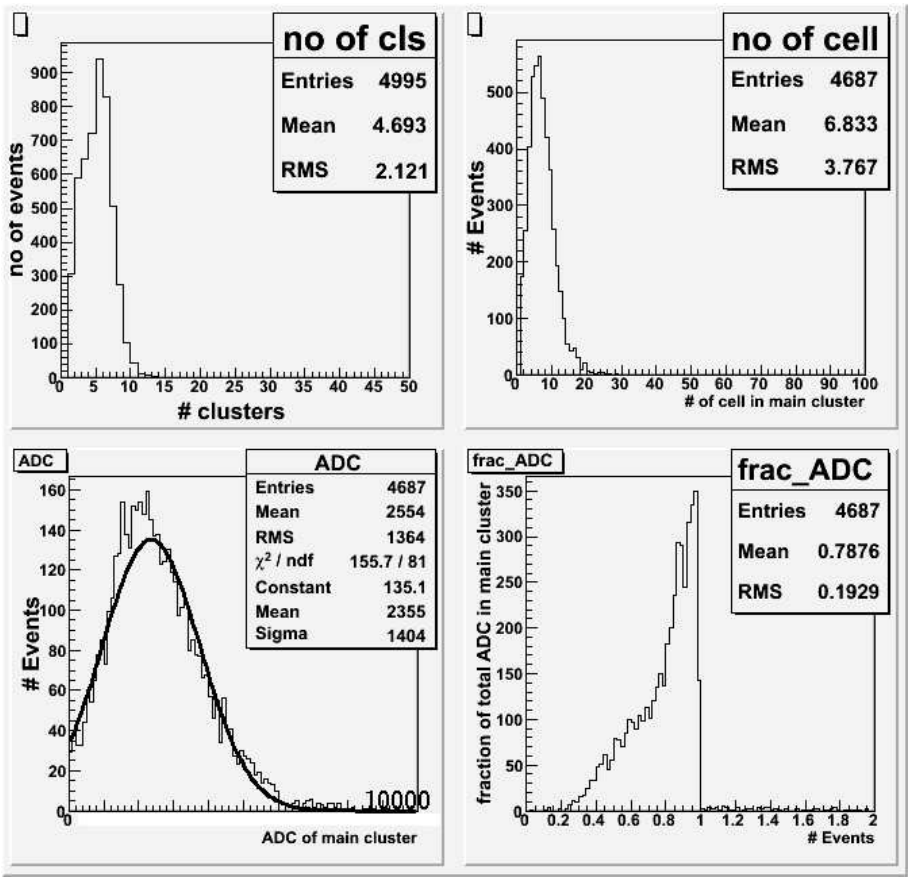

Figure 3.20: Characteristics of the clusters for an electron beam of 3GeV : *top left : the number of clusters per trigger; top right : number of cells in the largest cluster of an event; bottom left : ADC distribution of the largest cluster; and bottom right : the fraction of the total ADC contained in the largest cluster.*

The figure 3.20 shows the distributions of the number of clusters per trigger (top left), number of cells in the largest cluster in an event (top right), ADC distribution of the largest cluster (bottom left) and the fraction of the total

energy	*ADC cut*	*<no of clusters>*	*<ncell>*	*ADC(main cluster)*	*Simulated energy (keV)*
MIP	..	..	..	300	1.61
2GeV	30	2.7	5.3	1976(75%)	11.50
3GeV	30	4.6	6.8	2554 (78%)	15.33
6GeV	30	5.8	9.9	3788(66%)	32.03

Table 3.2: Summary of electron and pion data taken for calibration relation

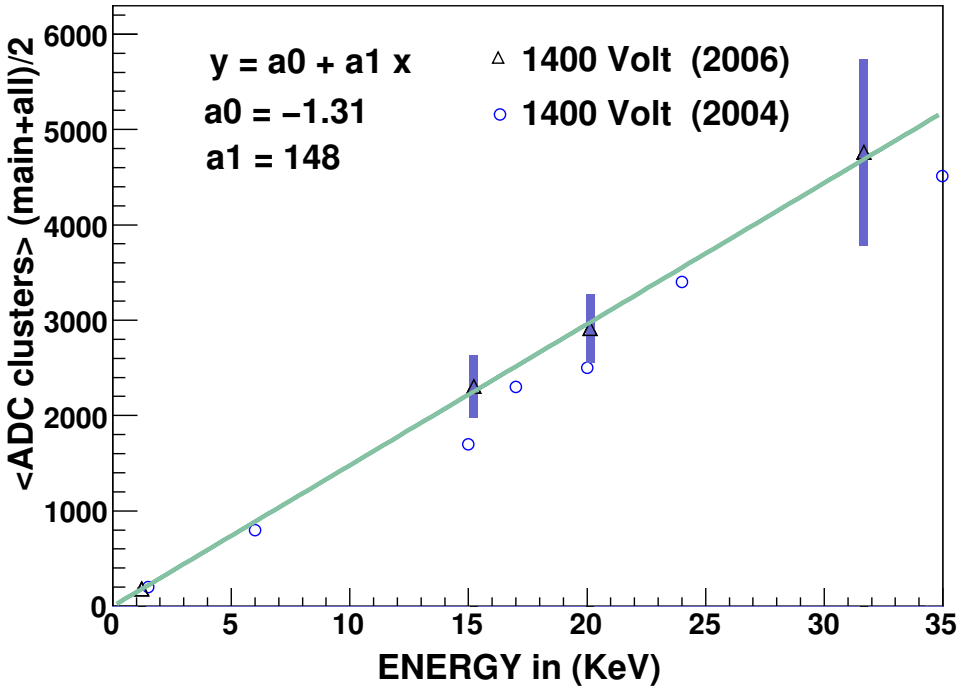

Figure 3.21: Calibration curve at 1400 Volt. Markers with red circle are 2004 data points.

ADC contained in the largest cluster (bottom right) for electrons of 3 GeV energy. Table 3.2 shows a compilation of the corresponding results form the simulation and data. It should be mentioned that the average number of clusters per electron trigger is large thereby suggesting a larger cluster splittings, which might be the effect of a larger noise threshold (30 ADC) which leads to the creation of more disjoint cells and thereby making more clusters. We have therefore taken the main cluster for obtaining the calibration relation.

Figure 3.21 shows in X-axis the average energy deposition in keV obtained from the simulations, while the Y-axis shows the corresponding average cluster energy from data (in ADC). Data are fitted with a polynomial of degree-2 (y = $a_0 + a_1$ x) giving the constant value a_0 = -1.31, and $a1 = 148$. There is however a large sytematic uncertainty in their values which may arise due to the cell to cell gain variations. The calibration relation at lower operating voltage like at 1300V is obtained from 2009 test-beam data which is not discussed here.

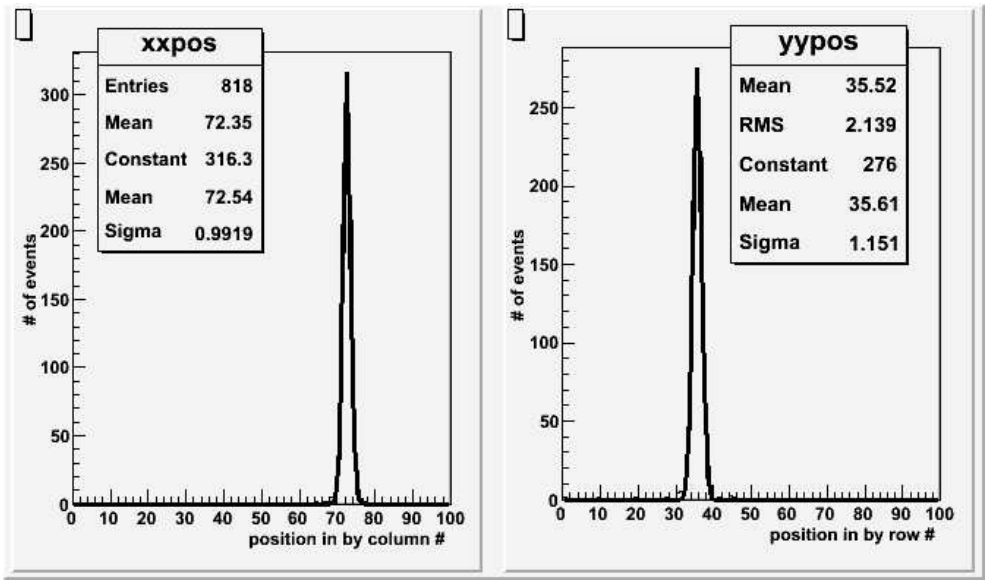

Figure 3.22: The event-wise distribution of the centroid position of the main cluster.

Position determination

Another important study is the precision in determining the position of the electron incident on PMD. The (x,y) coordinates of the incident electron is determined by the area of the finger scintillator which is 0.3cm×0.3cm. Fig.3.22 shows the distribution of the centroid of the main cluster event-wise. Therefore the Gaussian fitted width of the distribution determines the resolution of the position measurement. X-axis in the figure is in units of row and the column number. After applying all the required conversions the widths come out to be $\sigma_x = 0.49$ cm and $\sigma_y = 0.49$ cm for 2 GeV.

At the end, we can summarize the main results from the test beams. Pion beams show clear MIP distributions with an efficiency plateau reaching to ∼95% from 1300 V and beyond. There is ∼0.83% cells on preshower side which are found to be saturated with 5 GeV pion beam for the detector at 1375 V. Cell to cell gain variations are within 15%. Electron beam results comes out with a calibration relation (polynomial of degree 2) at 1400 volt with a constant term of a_0 =-1.31 and slope of a_1 = 148.

3.4 PMD performance in simulations for pp collisions at $\sqrt{s}$ = 14 TeV

We have performed detailed simulation of the PMD response for pp collisions at $\sqrt{s_{NN}}$ = 14 TeV, the highest energy of pp run at LHC. The work consists of two steps (i) to study the response in the event generator level using PYTHIA [121] and (ii) to study the response with the detector using full Geometry and Tracking (GEANT) [122, 123, 124]. PYTHIA was tuned for a Minimum Bias trigger condition and the particles from the generated events were transported by GEANT which incorporated all the possible interactions in the active volume of the materials in the ALICE detectors [118, 125, 126, 127]. The study was performed with various detector configurations (e.g, 1. only PMD present in ALICE, 2. PMD along with the all other detectors in position (Time Projection Chamber (TPC), Inner Tracking System(ITS), Silicon Pixel Detector (SPD), Photon Spectrometer (PHOS), Time of Flight (TOF), Electromagnetic Calorimeter(EMCAL), Forward Multiplicity Detector(FMD)).

For step (ii), we adopted a procedure for reconstruction of PMD hits. The particles interacting with the converter deposit energy in one or more cells of PMD. The energy deposited by all the incident particles hitting a single cell were summed up and was converted to ADC-channels, which are known as DIGITS. Digits are like the measurements of cell ADCs in the real experiment. We then find clusters formed by adjacent affected cells. The procedure is called "clustering". A cluster represents the response of a single incident particle, may be photon or/and hadron. Clusters are described by some basic properties like number of constituent cells, cluster strength in terms of ADC and the cluster profile like gaussian fitted width. A cluster can be associated to an incident particle (track) from which it is originated and the method of connecting a track to a cluster is termed as "*association*". While associating a cluster to an incident particle based on an algorithm, it might be seen that the particle may

give rise to more than one clusters or a particle might not produce any cluster. Therefore the association is to be done on an one to one cluster basis where the same track might be forming many clusters. Thus the prominent cluster is to be called the main cluster and the smaller ones as split clusters. After "clustering" and "association", it is the task to discriminate photon clusters from other clusters mostly formed by charged particles.

"*Discrimination*" can be done by putting threshold on cluster ADC and cell multiplicity of a cluster in the preshower plane. The alternate way is to form a CPV and PMD correlations, i.e, vetoing a charged particle using results from the CPV plane. Algorithms like artificial neural network (ANN) can be applied for this purpose.

Finally one can obtain the efficiency of photon detection and the purity of photon like clusters. These quantities will be used to correct measured multiplicities to final ones.

3.4.1 Events from PYTHIA for pp@14 TeV

Particles on PMD

The basic aim of PMD is the detection of photons and their spatial distributions at forward rapidities. LHC is to run for pp collisions at a maximum of $\sqrt{s}$ = 14 TeV. There are several Monte Carlo event generators like PYTHIA [121], HERWIG [128], PHOJET [129], which could be used for detector simulations incorporating realistic scenarios of particle production based on the present level of understanding. PMD has a full ϕ-coverage in the η range extending from 2.3 to 3.5. Therefore, we discuss photons in this pseudorapidity coverage. Photons generated by PYTHIA in pp collisions at LHC energy can be divided into the following categories,

1. decay photons coming from π^0, η, etc.
2. direct photons coming from the Compton scattering between a quark and a gluon and by the annihilation mechanism of a quark and antiquark.
3. fragmentation photons originating by the fragmentation of a quark and a gluon.

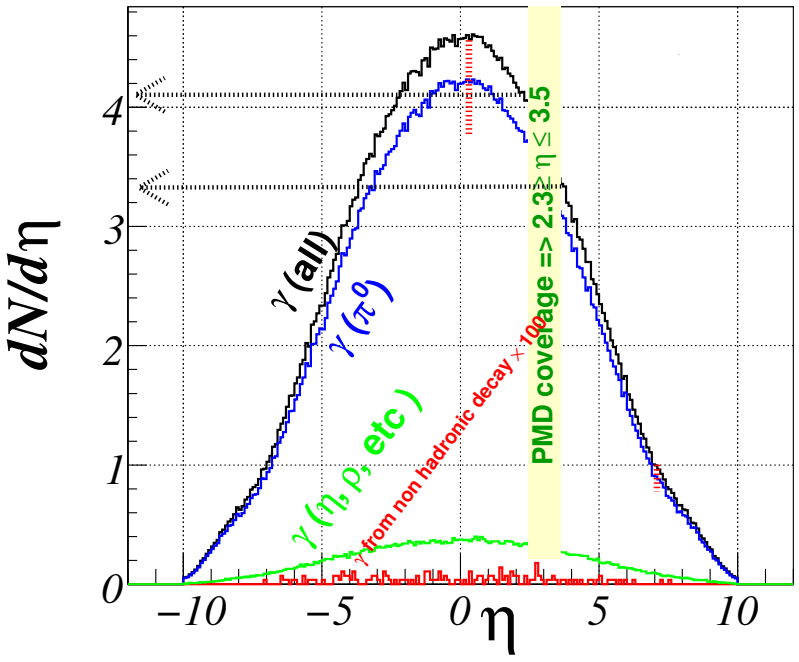

Figure 3.23: Pseudorapidity distribution of photons in pp collisions at $\sqrt{s}$ = 14TeV.

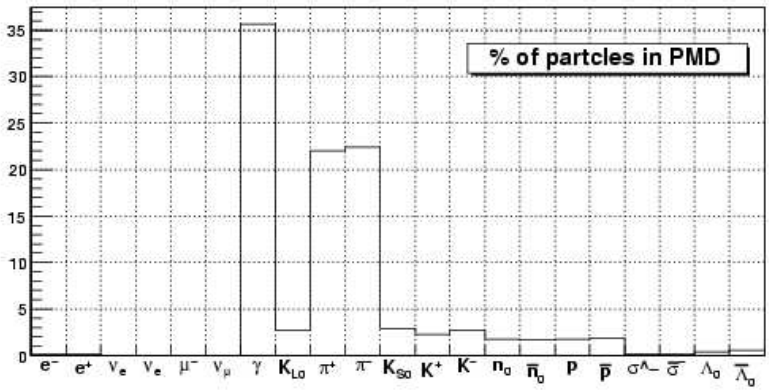

Figure 3.24: The composition of the particles incident in the PMD coverage as generated by PYTHIA.

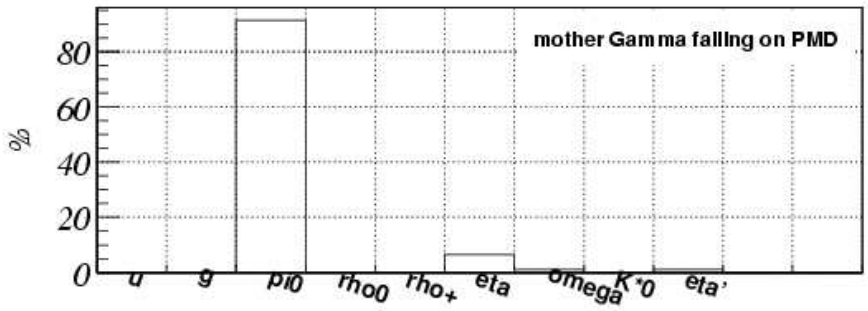

Figure 3.25: The sources of photons in PMD.

PMD detects all these photons as signals. The detector will have background from the charged particles like $\pi^{\pm}, K^{\pm}, e^{\pm}$. The Fig. 3.23 shows the pseudorapidity distribution of photons in pp collisions at $\sqrt{s} = 14$ TeV. Most of the photons are the decay products of π^0. Fig. 3.24 shows the distribution of different particles in PMD pseudorapidity coverage. 36 % of the particles incident on PMD are photons which are originating from π^0 decay (≈90%), η (≈5%). The contribution of single photons is less than 1% as shown in Fig. 3.25.

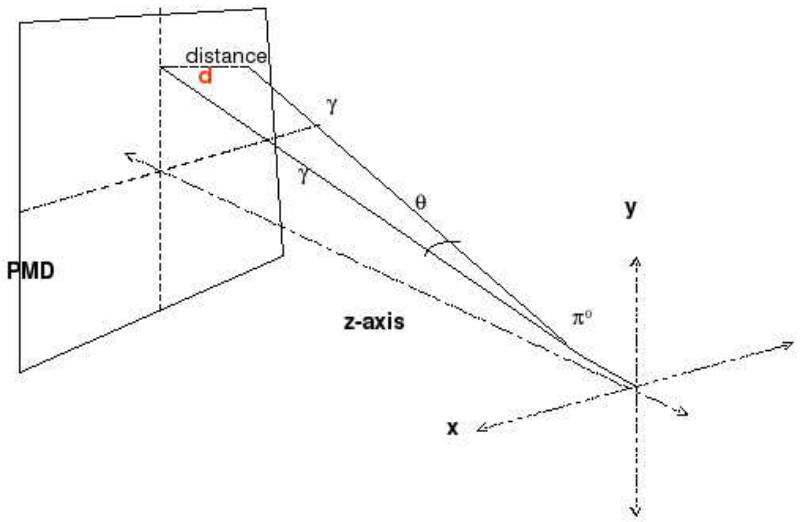

Figure 3.26: The schematic of the decay of π^0 to photons incident on PMD

Decay photons from π^0

When π^0s decay into two photons, both of them may or may not fall on the PMD plane even though the π^0 lies inside the detector acceptance. The opening angle between the two photons depends upon the momentum of the photons and that of the parent π^0. The Fig. 3.26 shows the schematic of the π^0-decay where both the photons fall in the PMD coverage. The opening angle is indicated by "θ" and the distance over the detector plane is indicate by "d" (cm). Fig. 3.27 (left) shows the mean value of the opening angle which corresponds to "$< d >$" = 26.47 cm as shown in Fig. 3.27(right). This means that PMD will be able to detect two decay photons from π^0 decay (when falling on PMD) as separate clusters.

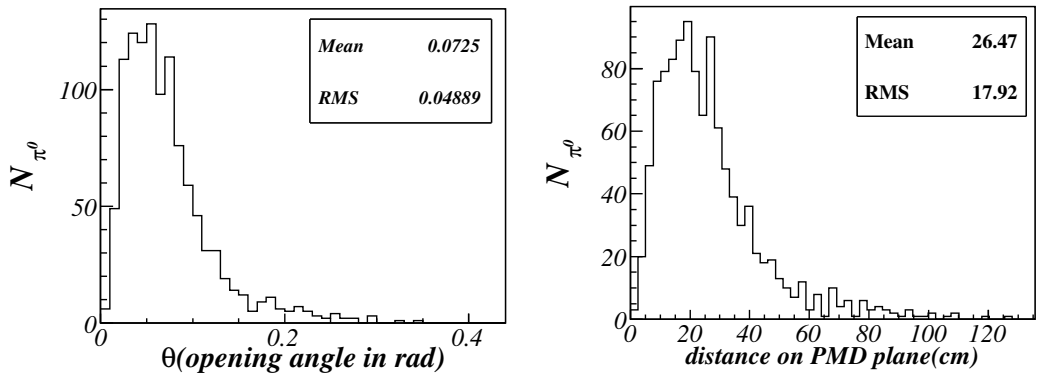

Figure 3.27: The distribution of the opening angle (left) and distance of separation (right) of two decay photons on the PMD surface

3.4.2 Performance of the reconstruction procedure of PMD

Photon Conversion Efficiency and photon Loss in Reconstruction

Incident photons form electromagnetic showers (electron and positron) in the lead converter placed in front of the PMD plane. These shower particles are detected by the PMD plane. Fig. 3.28(top) shows the dN/dp_T distributions of the incident photons in PMD which produce hits on PMD plane. The average conversion efficiency defined as the ratio of the number of photons producing

hit to the incident number of photons is ≈87.7 %. The photon conversion efficiency depends on the transverse momentum of the incident particles. The low p_T photons are having lower conversion efficiency as is shown in Fig. 3.28 (bottom). It shows that at $p_T \approx 200$ MeV the value is around 80 % which finally increases to 90% at $p_T > 1.0$ GeV and above.

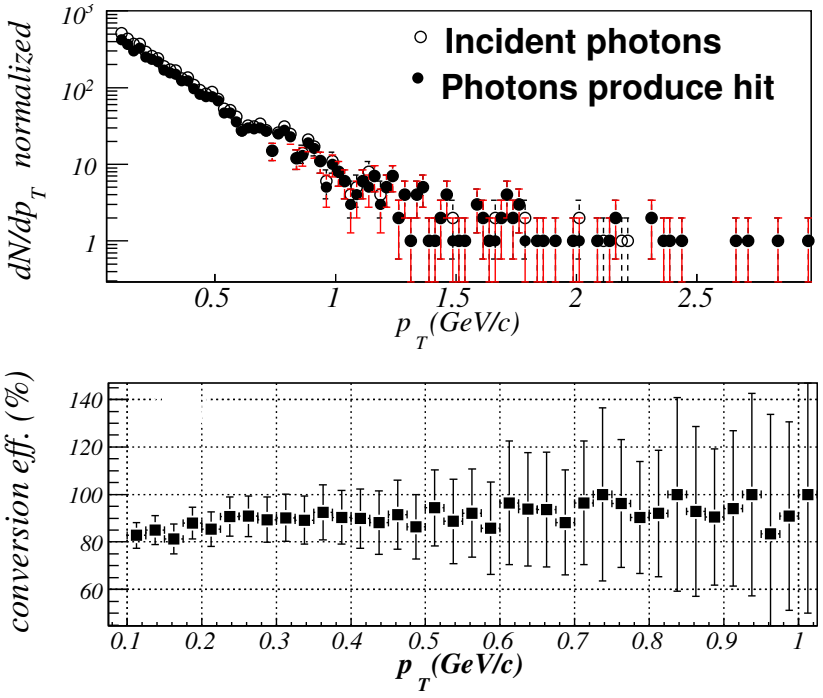

Figure 3.28: dN/dp_T distributions of photons incident and detected on PMD (top). The conversion efficiency with p_T (bottom).

Photon loss at reconstruction of clusters

The reconstruction of photons in simulation include summing of the hits into digits and then formation of clusters. The cluster finding procedure is based on a nearest neighbour algorithm. In the first pass, a search is made for local maxima. After the search for all the maxima on the entire detector, the energy depositions in cells, which are common to more than one local maxima, are redistributed assuming a gaussian energy deposition profile. In the process of

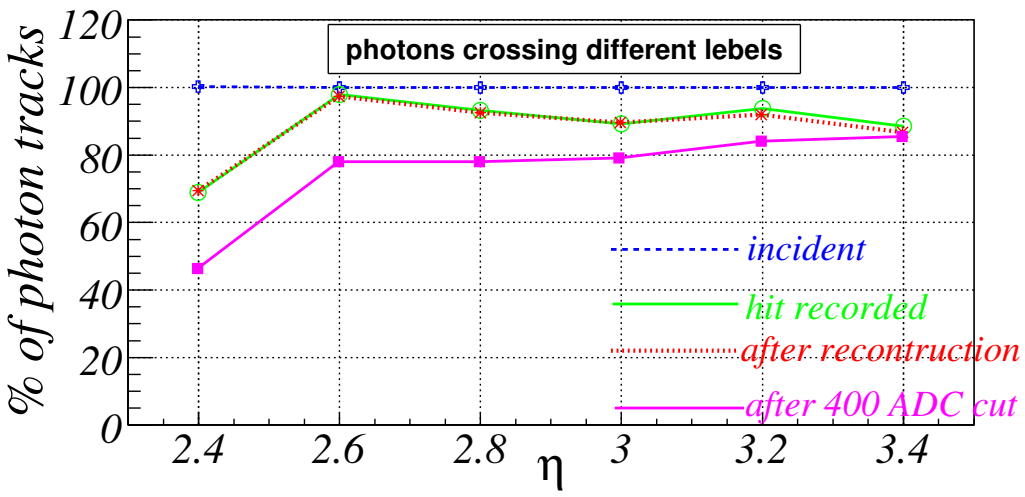

Figure 3.29: Photon loss at the hit level and the reconstruction level.

reconstruction, there might be an overlap between the showers produced by two or more incident particles and therefore the reconstruction needs to take care of splitting of the clusters formed by the overlapping showers. This overlapping is more pronounced at higher multiplicity where the occupancy of the detector is large. For pp collisions, the occupancy is not large enough to result in splitting of a cluster. In simulation, a procedure of *association* is needed to be done for an incident particle to a cluster formed after reconstruction. The association algorithm used here is as follows. If a cell is being hit my multiple tracks, the track having maximum energy deposition is assigned to the cell. The track ID of the cell having the maximum energy among the cells of a cluster, is assigned as their track of origin for the cluster. It works well for pp as it is clear from Fig. 3.29 that the % of photons which are converted in lead is being retained even after reconstruction (the blue and the read line almost overlap each other). The pink line demonstrates the percentage of photons having cluster ADC above 400 giving an qualitative idea that choosing the clusters with some ADC threshold will result in reduction of photon detection efficiency. This type of cluster threshold is required for distinguishing photons from hadron like clusters which will be used to obtain the efficiency and purity of photons in a quantitative way.

Photon cluster identification, the efficiency and purity of photon detection

We discuss here two methods for identifying photon clusters, first by using the clusters only from the preshower plane and next by using the clusters from the CPV plane along with the PMD plane.

Cluster properties of photons and hadrons have some basic differences. Each cluster has a definite size and shape. The size of the cluster in terms of their ADC value, the spread of the shower expressed in terms of the number of cells in the cluster (N_{cell}), is convenient to use for their separation. The cluster shapes can also have different spatial ADC distributions, i.e, whether the energy is localized mostly within a single cell of the cluster, or tends to be distributed equally over the cells of the cluster. The cluster shape can be

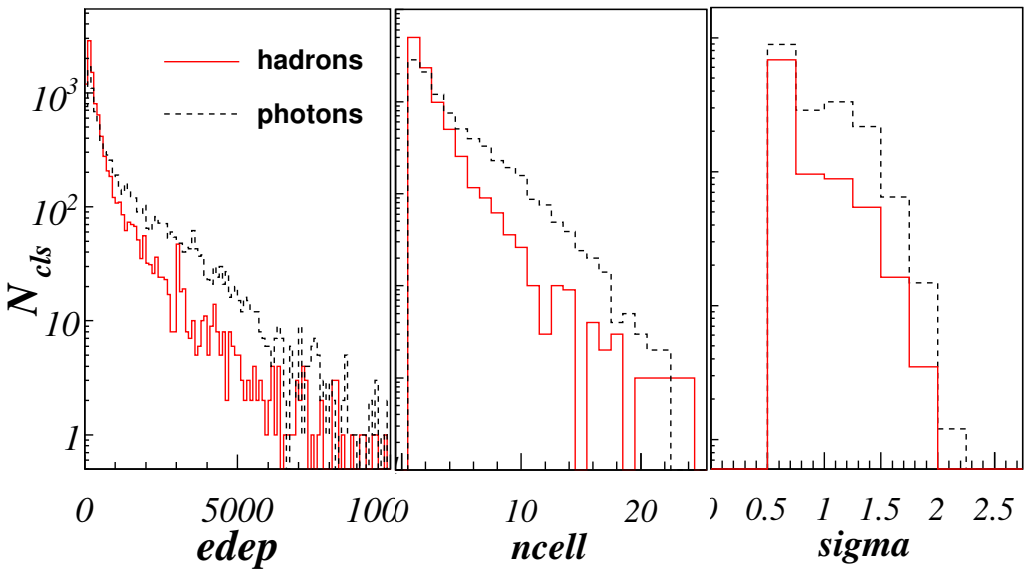

Figure 3.30: Cluster parameter distributions for photons and hadrons.

defined by the σ of the distributions, when fitted by a 2D-Gaussian. The Fig. 3.30 shows the ADC, N_{cell} and σ distributions of photons and hadrons clusters in pp collisions using events from PYTHIA. Clearly there is a distinct difference in the distributions showing that the photon clusters deposit more energy, number of cells for photon cluster is larger and σ of the photon cluster

attain a higher value. In this discussion, while defining a photon like cluster we set a threshold on the ADC value and the number of cells in the clusters. This will automatically reject clusters which are mostly formed by hadrons. Therefore the photon-like clusters will have background from the clusters originating from photons and from the multiple clusters formed by a photon track.

The photon counting efficiency, ε_γ and fractional purity of the photon sample, f_p are defined by the following relations,

$\varepsilon_\gamma = N_{\gamma,th}/N_{\gamma,inc}$,
$f_p = N_{\gamma,th}/N_{\gamma,like}$, where
$N_{\gamma,inc}$: number of incident photons from the event generator.
$N_{\gamma,th}$: number of photon clusters above the hadron rejection threshold.
$N_{\gamma,like}$: total number of clusters above the hadron rejection threshold.
Efficiency and purity of the detected photons depend on the chosen threshold

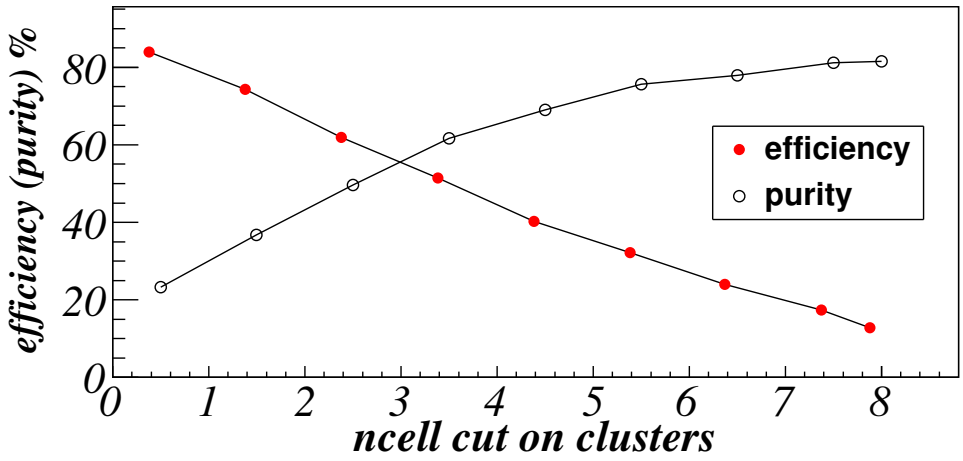

Figure 3.31: Variation of efficiency and purity with ncell threshold with a fixed ADC threshold of 100.

of ADC and the ncell [3] as shown in Fig. 3.31 and Fig. 3.32. We need to optimize the ncell and ADC thresholds for obtaining reasonable efficiency and purity. With ncell > 1 and ADC > 400, the efficiency and purity in the η coverage of PMD is shown in figure 3.33. These results are applied to the data used to obtain the corrected final pseudorapidity distribution of photons.

[3] n(/N)cell is the number of cells in a cluster

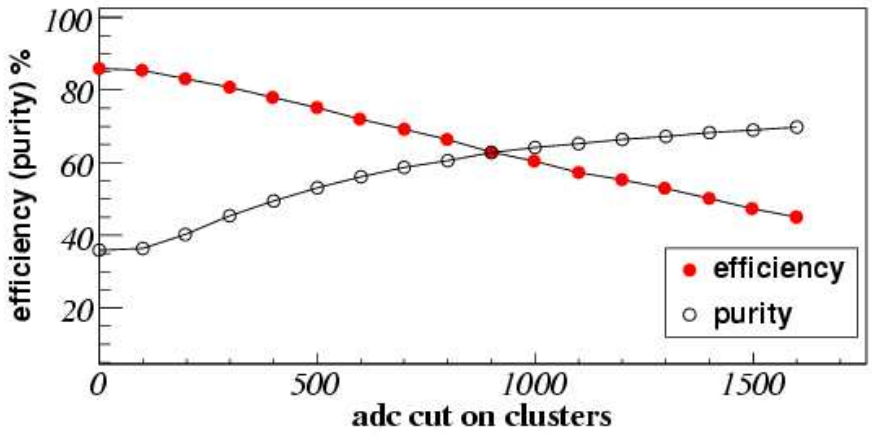

Figure 3.32: Variation of efficiency and purity with ADC threshold of clusters keeping a ncell cut of > 1.

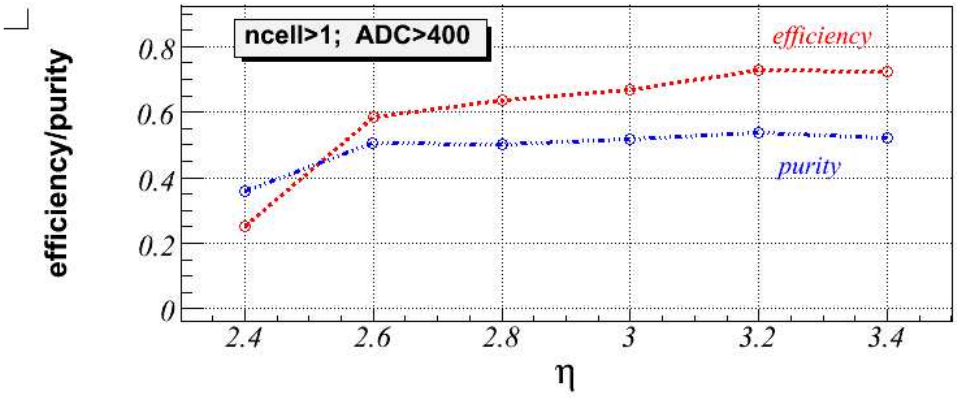

Figure 3.33: Efficiency and purity with ADC > 400 and ncell > 1.

Track reconstruction efficiency

Deviations of cluster (η and ϕ) from the incoming track (η, ϕ) are defined as the pseudorapidy deviation ($\Delta\eta = \eta_{track} - \eta_{cluster}$) and the azimuthal angle deviation ($\Delta\phi = \phi_{track} - \phi_{cluster}$). The combined effect of deviations in η and ϕ can be written as $R = \sqrt{(\Delta\phi)^2 + (\Delta\eta)^2}$. The Fig. 3.34 and Fig. 3.35 show $\Delta\eta$ and $\Delta\phi$ distributions of hadrons and photons respectively satisfying gamma like clusters criteria. The effect of material in front of the PMD is dominantly visible for hadrons as a bump at higher $\Delta\eta$ (Fig. 3.34 left). The

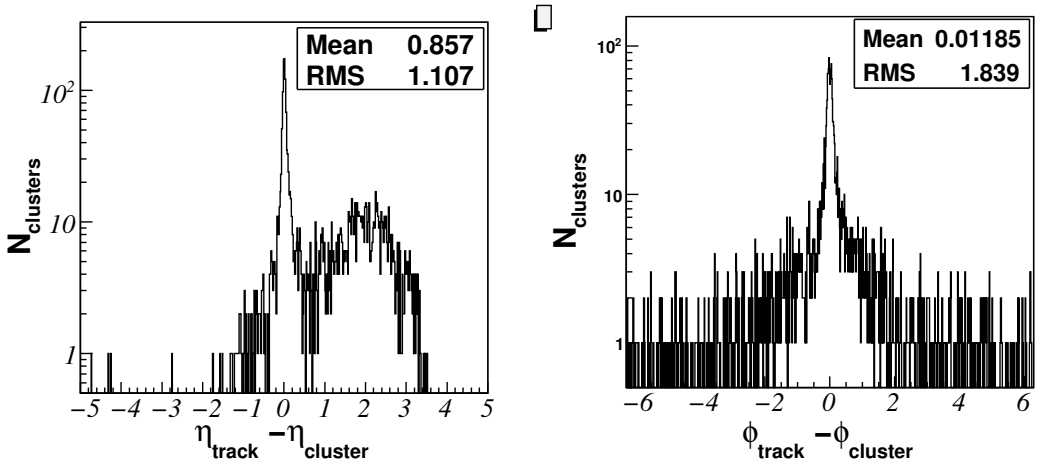

Figure 3.34: The $\Delta\eta$ and $\Delta\phi$ distributions of hadrons

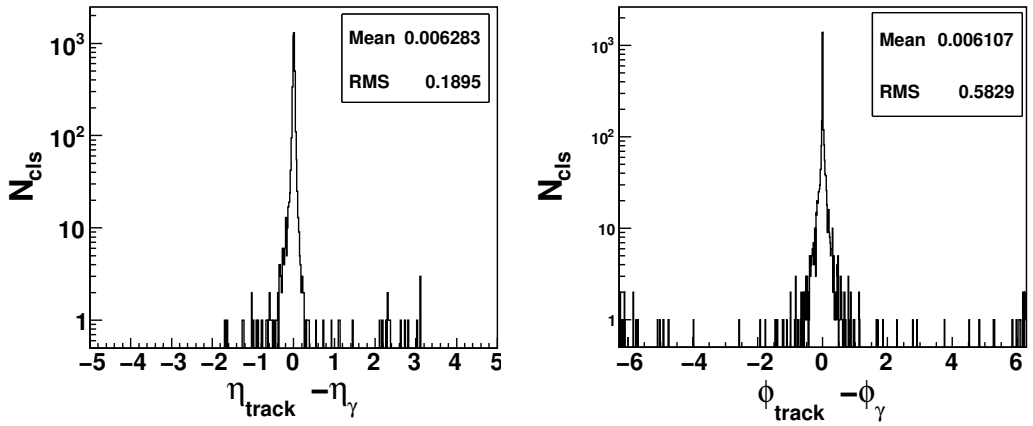

Figure 3.35: The $\Delta\eta$ and $\Delta\phi$ distributions of photons

effect of materials on photon detection is two fold. Mainly, the material for higher radiation length absorbs low p_T photons and convert them into showers of electrons and positrons of lower p_T. These again interacts with the converter of PMD and either get absorbed or form small showers which might not cross the threshold criteria of photon-like clusters. The hadrons on the other hand undergo hard interactions and the products are not likely to be absorbed in the material. The Fig. 3.36 shows the interaction nature of photons and

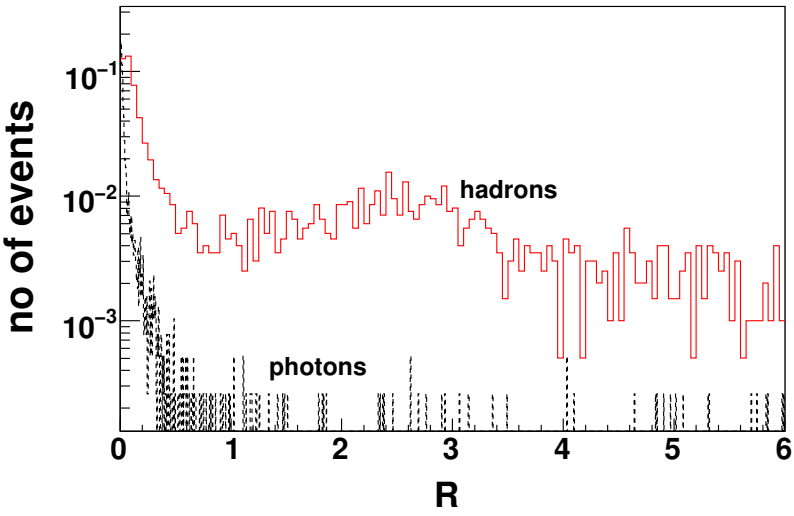

Figure 3.36: The R distributions for photons and hadron clusters.

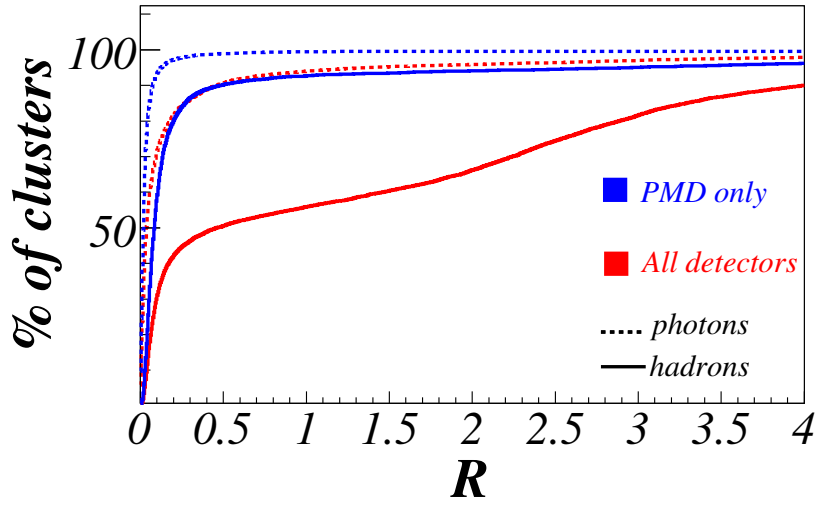

Figure 3.37: The R distributions for photons and hadron clusters with and without material in front of PMD.

hadrons represented by R, where it is found that the absorption of clusters for hadronic interactions are having wider R, thereby showing wider nature of the hadronic cluster. The Fig. 3.37 shows the R distributions, with and without any material in front of PMD.

Discrimination using CPV plane

We have discussed here a method of using the CPV clusters for removing charged particles on PMD plane, thereby improving the efficiency and purity of photon detection. Vetoing the PMD clusters by CPV clusters is performed by dividing the x-y region of the detector into small square pads. If there is a CPV cluster and a preshower cluster falling in the pad region, the cluster is rejected. The size of the square region is varied in order to optimize the efficiency and purity. Fig. 3.38 shows the schematic of a zone created by

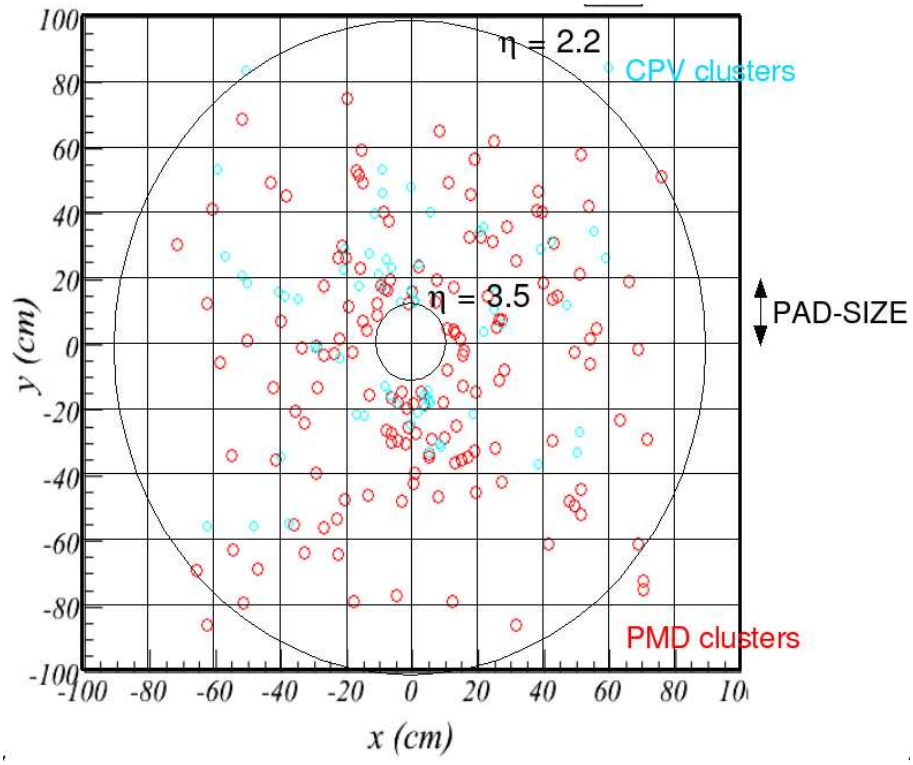

Figure 3.38: Clusters on CPV and PMD planes laid on a matrix divided into a region of square pads

dividing into pads. Variation of efficiency and purity for various pad sizes is shown in Fig. 3.39. In this study, simulations are done by PMD alone in the setup and by including all other ALICE detectors. In later case more materials will cause large background due to conversion. As expected, the efficiency reduces with the pad size and the purity increases as the photon clusters get merged and more number of CPV clusters veto charged clusters on the PMD

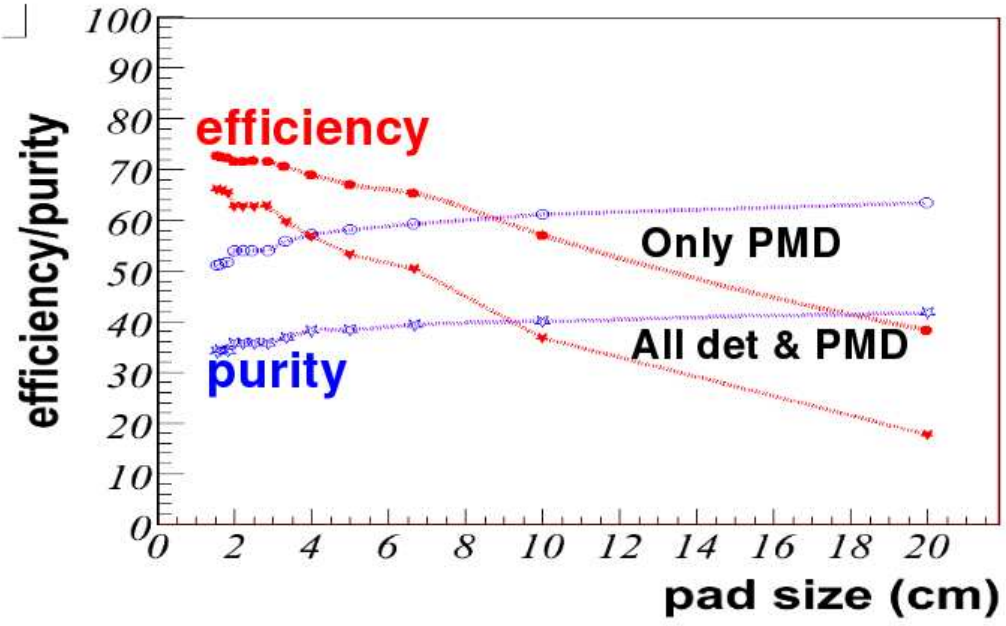

Figure 3.39: Efficiency and purity at different pad sizes for PMD only and in presence of all other ALICE detectors.

plane. For pp collisions with a pad-size of 4cm×4cm, the efficiency and purity reaches 70 % and 55% respectively.

With the presence of other detector materials the situation worsens quickly where the efficiency and the purity drop dramatically. In such cases the use of cluster properties in addition to the vetoing technique may be useful.

3.5 Conclusion and Summary

The Photon Multiplicity Detector in ALICE has been described with relevant information on detector design and fabrication. The testing procedure with the application of High Voltage is described and the performance of the detector in terms of its leakage current has been discussed.

The early testing of the modules in beam test was an essential part of the detector development process. A complete study of the detector and its response

to MIPs and electrons have been performed with the test beam data of 2006 and 2009.

Keeping in mind the data taking by PMD in 2009 pp collisions at $\sqrt{s}$= 14 TeV, we have performed a detailed study of the detector performance using PYTHIA. PMD is a preshower detector and hadrons having a finite interaction probability at the level of 10%, the hadronic showers in preshower form photon like clusters. The detection of the photons on the basis of the cluster properties in the preshower plane alone gives $\sim$ 60% efficiency and $\sim$ 50% purity of photon detection. An effort of using CPV-PMD cluster correlation in vetoing out the hadronic clusters is made in the last section of this chapter. With a pad-size of 2$\times$2 cm^2 $\sim$ 70% efficiency and $\sim$ 35% purity are obtained. It is being suggested the CPV-preshower correlation along with the cluster properties might give rise to better efficiency and purity.

Chapter 4

Jet properties from dihadron correlations in pp and dAu collisions

[1]

In this chapter, we discuss the topic of correlation among the produced particles from dijets. Here the term "*di-hadron correlation*" represents the azimuthal angle correlation of the associated particles with respect to a trigger particle. The trigger particle is taken as the leading particle (particle with highest p_t) in the event and all the other charged particles are taken as the associated particles. This technique has been used extensively in larger colliding system like $Au + Au$, where it has been shown that the trigger particle is likely to emerge from the surface of the colliding medium (fireball) and represents the leading particle of a jet, while the away jet passes through the medium and might get quenched. Systems like $d + Au$ and $p + p$ are used as reference systems for $A + A$ collisions[2]. In this work, we have studied the reference systems e.g. $p + p$ and cold nuclear matter i.e, $d + Au$ by the method of azimuthal correlation.

The analysis has been performed on two datasets from the STAR experiment,

- High Tower (HT) datasets where π^0 is taken as the trigger particle,

[1] In this chapter for denoting transversity we have used "t" instead of "T" which is used in all other chapters. e.g $p_T, k_T, ... \rightarrow p_t, k_t, ...$

[2] "A" stand for heavy any heavy ion, e.g. Au, Pb, etc.

- Minimum Bias (MB) dataset taking charged particles as the trigger particles.

In this discussion, the correlation functions are named as π^0-ch and ch-ch correlation where π^0 and charged particles (mostly $\pi^{\pm}$) are used as trigger particles respectively. This chapter consists of a description of the formalism used for extracting the jet parameters in section 4.1, the data cleanup procedure and analysis details in section 4.2, the extraction of the parameters explaining the jet properties using both π^0-ch and ch-ch correlation techniques in section 4.3, the centrality dependence of jet parameters for dAu collisions 4.4. A simulation study of the correlation results using PYTHIA and HIJING in section 4.5 and a summary of comparison of the results of acoplanarity with the earlier measurements in section 4.6.

4.1 The intra-jet transverse momentum (j_t) and the jet acoplanarity (k_t)

In heavy-ion collisions at RHIC energy ($\sqrt{s_{NN}} = 200$ GeV) a large fraction of the produced particles is expected to originate from the initial hard scattering of the nucleonic constituents. Partons participating in the hard scattering traverse the medium formed in the collision and eventually fragment into a cluster of particles, called *jets*. Due to the presence of a hot and dense medium formed in the high energy heavy ion collision, the partonic energy loss is expected to result in a softer fragmentation function of the produced particles [130, 131, 132] and partons may even be completely absorbed. Indeed, there are several interesting observations at RHIC which are considered as signatures of the presence of such a hot and dense medium. The results prominent among them are (i) suppression of the particle spectra at large p_t in central Au+Au collisions. [133, 134] and (ii) suppression of the yield of the awayside peak in azimuthal correlations in central Au+Au collisions when compared to the peripheral or pp collisions [135]. For understanding these results in terms of the formation and modification of jets in the media, investigations are needed on smaller systems (e.g. p+p and d+Au collisions). While in principle, one could use the method of topological jet reconstruction [136, 137, 138, 87] in these systems to study the fragmentation process in detail, in the present study we prefer to use the two-particle azimuthal correlations. One of the reasons is that it is very difficult, if not impossible to reconstruct the jets unambiguously in AA collisions. Measured azimuthal correlations on the other hand show clear

signatures of di-jet events: there are two distinct peaks, a *near-side peak* at $\Delta\phi = 0$ and an *away-side peak* at $\Delta\phi = \pi$. Two quantities commonly used to characterize the properties of jets are (i) j_t, the transverse momentum of the jet fragments relative to the jet axis and (ii) k_t, the transverse component of the momentum of the hard scattered partons. It has been found that both in p+p and p+A collisions, j_t remains constant, while k_t increases substantially in p+A in comparison to p+p. A larger k_t in p+A collisions suggests the existence of an additional nuclear k_t which has been attributed to the multiple scattering of the particles in the nuclear medium [87]. It is therefore of fundamental importance to measure k_t in the pA system at RHIC energy and compare the results from pp collisions. In this study we have extracted j_t and k_t for pp and dAu collisions at $\sqrt{s_{NN}} = 200$ GeV.

4.1.1 Partonic k_t in nuclear medium

Nuclear modification of the intrinsic k_t of partons due to multiple hard scattering in the nuclear media can be expressed as $\langle k_t^2 \rangle_{total} = \langle k_t^2 \rangle_{pp} + \langle k_t^2 \rangle_{nucl}$, where $\langle k_t^2 \rangle_{nucl}$ is expected to have a $A^{1/3}$ dependence. On the basis of multiple scattering only, $\langle k_t^2 \rangle_{nucl}$ is expected to be $\simeq 0.7$ GeV^2 [100]. Nuclear modification of $\sqrt{\langle k_t^2 \rangle}$ can be measured by the reconstruction of jets or by the measurement of correlation functions of the produced particles in p+A collisions and compare the values obtained in p+p collisions. In this paper, we discuss the measurement of $\sqrt{\langle k_t^2 \rangle}$ using the correlation method only.

4.1.2 Extraction of $\sqrt{\langle j_t^2 \rangle}$ and $\sqrt{\langle k^s{}_t^2 \rangle}$ using dihadron correlations

The method of two particle correlations aims to find the jet structure on the transverse plane, the plane perpendicular to the collision axis. The trigger particle carries the largest fraction of the jet energy, it therefore provides a reasonable approximation of the axis and the momentum of the near side jets. Jet plane is defined as the plane containing the beam line and centre of momenta of the jets. Particles emitted from the jet are expected to lie near the jet plane and naturally the trigger particle lie very close to the jet-plane. Therefore in order to study the properties of the awayside jet, all the variables are defined with respect to the momentum of the trigger particle and the trigger plane.

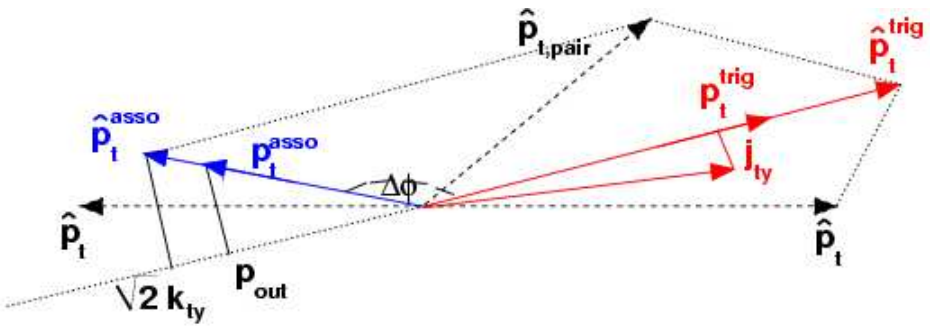

Figure 4.1: Two hard scattered partons on a plane perpendicular to the beam axis. Two partons with transverse momentum $\hat{p}_t$ in the parton's centre of mass frame are having transverse momentum $\hat{p}_t^{trig}$ and $\hat{p}_t^{asso}$ inlab frame. The net value of the transverse momentum of the partons are $\hat{p}_t^{pair}$. In experiments we measure a trigger particle of momentum p_t^{trig}, a part of one of the parton's momentum and p_t^{asso} for the associated. of parton.

Fig. 4.1 shows the schematic of two hard scattered partons in a plane perpendicular to the beam axis. Two partons each with transverse momentum $\hat{p}_t$ in the partons centre of mass frame are having transverse momenta $\hat{p}_t^{trig}$ and $\hat{p}_t^{asso}$ in the lab frame. The net value of the transverse momentum of the partons are $\hat{p}_t^{pair}$. Experimentally, we measure a trigger particle of momentum p_t^{trig}, a part of parton's momentum and the associated particles of momentum p_t^{asso}.

The jets are having net transverse momentum of $\langle p_t^2 \rangle_{pair} = 2\,\langle k_t^2 \rangle$. The average transverse momentum component of the away-side particle $p_t^{\vec{asso}}$ perpendicular to the trigger particle $p_t^{\vec{trig}}$ in azimuthal plane in labeled as p_{out}. p_{out} contains the information of the acoplanarity and a width incorporated by the jet fragmentation. Jet fragmentation gives rise to each of the fragmented particles a momentum perpendicular to the jet axis ($j_\perp$). The average of $j_\perp$ provides the jet parameter j_t. Fig. 4.1 shows the schematic of the jet fragmentation transverse momentum component j_{ty} of the trigger jet.

For the trigger particle and the associated particles emerging from the same jet, the width of the the near-side correlation distribution can be related to.

$$\sigma^2 = \langle \Delta\phi^2 \rangle = \langle (\frac{j_{ty}}{p_t^{asso}})^2 + (\frac{j_{ty}}{p_t^{trig}})^2 \rangle \tag{4.1}$$

and with the approximation $j_{ty}^2 << {p_t^{trig}}^2$; $\sqrt{\langle j_t^2 \rangle}$ can be expressed in the form [104],

$$\sqrt{\langle j_t^2 \rangle} = \sqrt{2} \frac{p_t^{asso} p_t^{trig}}{\sqrt{(p_t^{asso})^2 + (p_t^{trig})^2}} {\sigma_N}^2 \tag{4.2}$$

The acoplanarity factor, $p_{out} = p_t^{asso} sin\Delta\phi$ is the transverse momentum of the awayside particle of momentum $\vec{p}_t^{asso}$ perpendicular to trigger particle of momentum $\vec{p}_t^{trig}$ in the azimuthal plane and k_{Ty}. p_{out} can be expressed in the form

$$\langle |p_{out}| \rangle^2 = x_E^2 [2\langle |k_{Ty}| \rangle^2 + \langle |j_{Ty}| \rangle^2] + \langle |j_{Ty}| \rangle^2 \tag{4.3}$$

, where $x_E = -\frac{\vec{p}_t^{asso} . \vec{p}_t^{trig}}{{p_t^{trig}}^2} = -\frac{p_t^{asso} cos\Delta\phi}{p_t^{trig}}$ and $\Delta\phi = \phi_{trig} - \phi_{asso}$. $\sqrt{\langle {k^s}_t^2 \rangle}$can be expressed in the form [104],

$$\sqrt{\langle {k^s}_t^2 \rangle} = \frac{\langle z_t(k_t, x_h) \rangle \sqrt{\langle k_t^2 \rangle}}{\hat{x}_h(k_t, x_h)} = \frac{1}{x_h} \sqrt{\langle p_{out}^2 \rangle - \langle j_{ty}^2 \rangle (1 + x_h^2)}. \tag{4.4}$$

Here we use σ_N as the near side correlation width, z_t is the fraction of the parton/s transverse momentum carried by a particle while fragmenting from it, $\hat{x}_h = \hat{p}_t^{asso}/\hat{p}_t^{trig}$, $\langle z_t \rangle = \langle p_t/\hat{p}_t \rangle$, and $x_h = p_t^{asso}/p_t^{trig}$

In our study we measure the LHS term in eq.4.4 where $\sqrt{\langle k_t^2 \rangle}$ is wrapped with the correction factors associated to the fragments. We have extracted the correction factors by using PYTHIA simulations and obtained $\sqrt{\langle k_t^2 \rangle}$ for pp and dAu collisions.

4.2 Data cleanup and Analysis details

4.2.1 Dataset and trigger selection

The $d + Au$ dataset for the year 2003 and the $p + p$ dataset for the year 2006 have been used for this analysis. The trigger conditions used for these two datasets are as follows :

Minimum bias trigger This trigger condition is satisfied by the presence of at least one neutron in the ZDC located in the gold beam direction. In addition, the trigger is also provided by the coincidence of at least one of the 18 small BBC tiles on both sides of the interaction points. This trigger condition is used for ch-ch analysis.

High Tower trigger The high tower trigger condition requires *the minimum bias trigger* condition and in addition, it requires signal from a BEMC tower above a certain threshold on energy deposition. Depending on the applied threshold, high tower triggers are divided in various categories as shown in table 4.1. We have used HT-2 trigger for our present analysis.

Dataset	*threshold for HT-1 [GeV]*	*threshold for HT-2 [GeV]*
d+Au 2003	*2.5*	*4.5*
p+p 2006	*2.6*	*5*

Table 4.1: High tower trigger conditions for different datasets.

4.2.2 Charged track selection criteria

For the charged tracks reconstructed by the TPC, following conditions are used as quality criteria for selection of a valid track.

i) The distance of closest approach (DCA) taken less than 1 cm.

ii) Track should have at least 20 hits in TPC.

iii) The pseudorapidity ($|\eta|$) of the track is < 1.0.

4.2.3 Event Cleanup

This analysis uses the reconstructed charged tracks from the TPC and the reconstructed neutral clusters from BEMC as described in section 4.3. For dAu data FTPC-EAST is used for centrality selections. Though BEMC has been developed for identifying the neutral mesons like π^0 and η by using the shower shape analysis from SMD signals, we are using only the clusters from BEMC towers which originate mostly ($\sim 90\%$) from π^0. Therefore, in the entire analysis, we will name *cluster-charge* correlations as π^0-*charge* correlations. We will use only TPC tracks for *charge-charge* correlations.

Background arising from the false trigger is more significant while considering neutral clusters in the analysis. They arise from the response of the noisy BEMC-towers, interaction of beam particles with the upstream materials and overestimation of the neutral energy from the neighboring charged

tracks falling inside the cluster-towers. Removal of false triggers in the π^0 trigger is more difficult when compared to the removal of false charged-particle trigger. In the later case, the track reconstruction has the advantage that it removes the tracks uncorrelated to the vertex. The method of cleaning of the BEMC signals are described in subsequent sections in detail.

Tower selection and cluster formation

BEMC towers are prone to malfunctioning and therefore special care has been taken so as to monitor the BEMC behavior online from time to time during data taking. For each run, ADC spectra of all the towers are analyzed to identify the common failure like malfunctioning of the readout board and/or the crates. The result of this quality assurance step is a time-stamped status table, which is used as an input to the physics analysis. The towers marked as bad from online monitoring are excluded from further analysis. This however reduces the detector acceptance but this will not affect our analysis since we derive per-trigger yield, which is obtained by normalizing from the available good trigger towers.

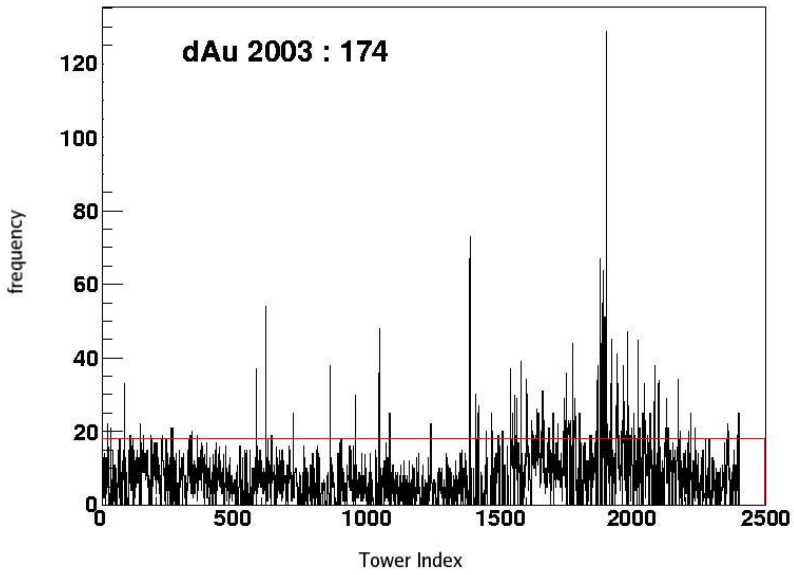

Figure 4.2: Trigger tower channel frequency distributions for 2003 dAu datasets.

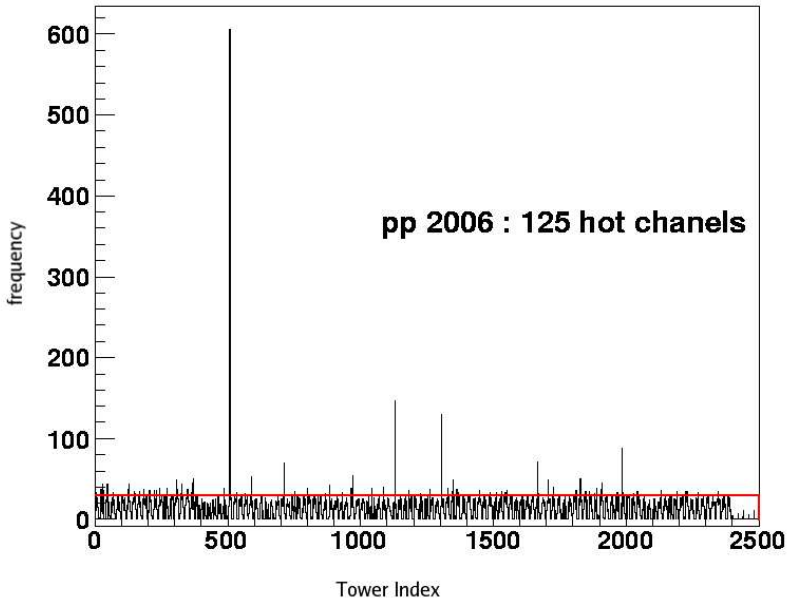

Figure 4.3: Tower frequency distribution for 2006 pp dataset.

In addition to the online analysis we also define BEMC noisy *hot towers* separately which often produce signals without any energy deposition by a real particle. In such cases, the hit frequency of the affected channels are above the mean frequency of all the channels. We have therefore performed detailed analysis for identifying the hot towers based on the tower frequency distribution. This is performed by studying the frequency of all the towers and the towers lying 3σ away from the mean frequency are assigned as bad. Fig. 4.2 and 4.3 show the hit frequency distributions of towers for dAu-2003 and pp-2006 data sets respectively. The identified hot towers are then removed from further analysis. About 6.8 and 2.0% of the towers are found to have bad status for dAu and pp, dataset respectively. The entire event is rejected if one of the towers in the trigger cluster is found bad.

Event selection based on vertex position :

Beam crossing position is tuned in such a way that the *interaction -vertex* lies close to the nominal vertex position inside the STAR-TPC. Vertex positions in the Z-direction (Z_{vertex}) are distributed around the nominal interaction point

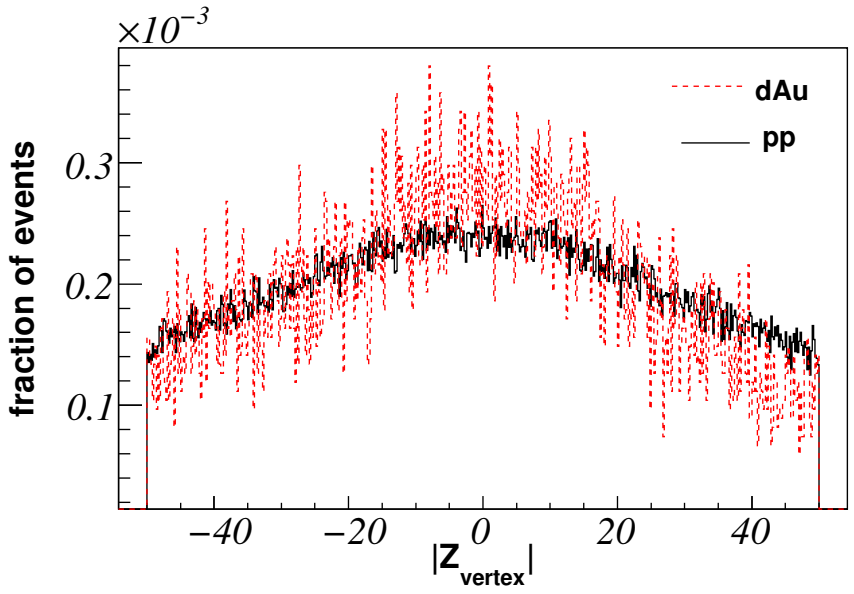

Figure 4.4: z_{vertex} distributions for pp and dAu collision events.

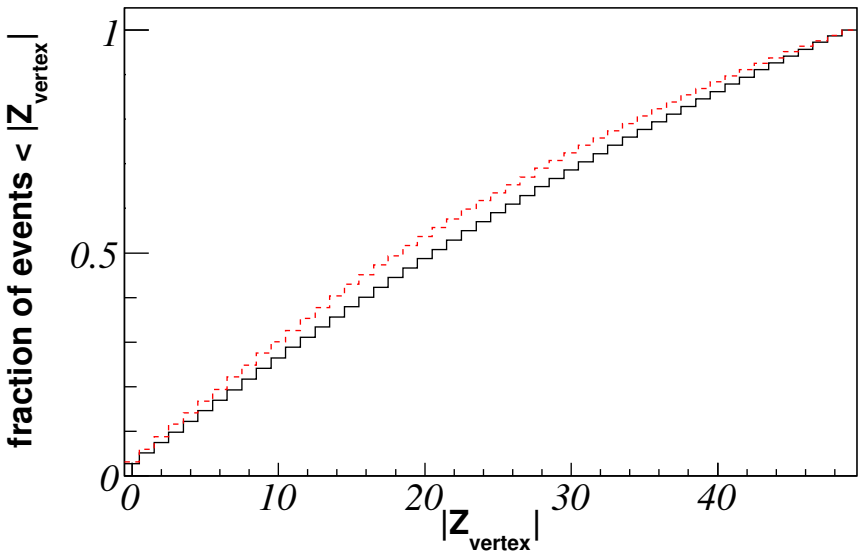

Figure 4.5: the fraction of events at various $|Z_{vertex}|$ relative to the events with $|Z_{vertex}| < 50cm$ for pp and dAu.

at Z-value = 0 cm as shown in Fig. 4.4. The precision of Z_{vertex} measurement is better than 1 mm. For a higher Z_{vertex} position, the TPC tracking efficiency drops since the track length becomes asymmetric on two sides of the vertex. Moreover for higher $|Z_{vertex}|$, BEMC remains no longer projective and the energy resolution of BEMC worsens. Therefore for good quality dataset, smaller $|Z_{vertex}|$ is desirable. This selection on the other hand reduces the event statistics. We have used $|Z_{vertex}| < 30cm$ in the analysis. The Fig. 4.5 shows the fraction of events at various $|Z_{vertex}|$ value relative to the events with $|Z_{vertex}| < 50cm$ showing that 70% data retained at $|Z_{vertex}| < 30cm$ from the set of events with $|Z_{vertex}| < 50cm$.

Event selection based on the event by event ratio of neutral to charged particle energy

One of the several ways to cleanup the events is to make use of the correlation between neutral and charged particle energy.

- The hit multiplicities of BEMC and TPC are expected to have an event by event direct proportionality. For events where BEMC is noisy, however, TPC track multiplicity should be lower compared to the BEMC hit multiplicity.
- For the low multiplicity events in pp where TPC hit multiplicity is low, consideration of total E_T for the neutral and total p_T for the charged particles might be more useful in event characterization. Therefore we discuss a method based on these quantities in detail below. It is clear from the Fig. 4.6 (left panel) that often BEMC gives higher total neutral E_T as compared the total of p_t charged tracks.

We have therefore used a variable "$NbyT$" $= \frac{\Sigma E_t}{\Sigma E_t + \Sigma p_t}$ for identifying the bad events. ΣE_t is summed over all the neutral clusters in the BEMC and Σp_t is the total p_t of all charged tracks within $|\eta| < 2.8$. The distribution of "$NbyT$" is shown in the Fig. 4.7, where the dAu data shows a hump near NbyT $\approx$ 1. By putting a NbyT$<$ 0.6, we removed the events containing the excessive neutral energy.

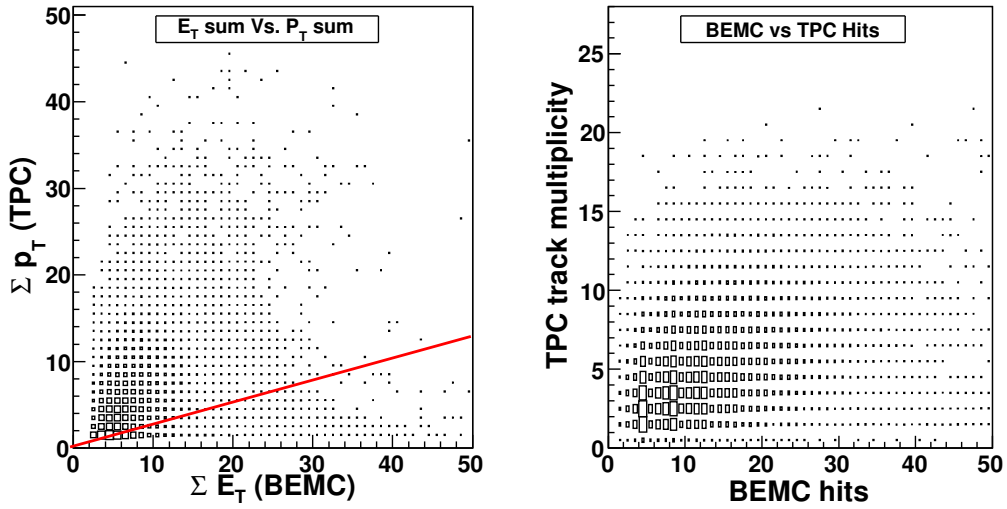

Figure 4.6: Left : Correlation between ΣE_t(BEMC) and Σp_t(TPC). We are expecting to reject the events below the solid line. Right : Correlation between the TPC track multiplicity and the BEMC-hit for 2003 $d + Au$ data.

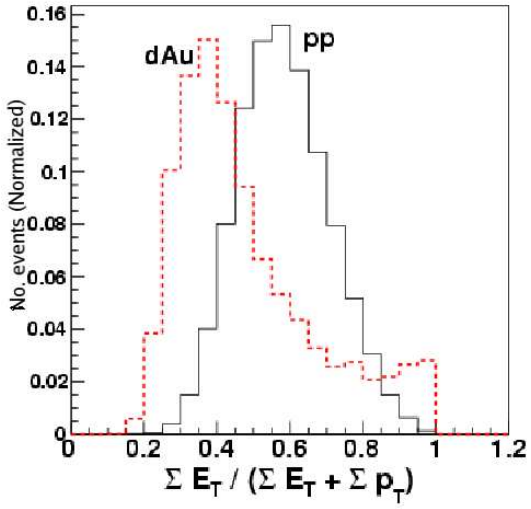

Figure 4.7: Event by event distribution of the ratio of the neutral to total energy. The events with a ratio below 0.6 are taken for further analysis.

4.2.4 π^0-trigger selection

Selection of pseudorapidity of neutral clusters as trigger particles

The trigger particles are π^0's reconstructed from the BEMC which span the range of $|\eta| < 1.0$. The Fig. 4.8 and Fig. 4.9 show the multiplicity of TPC

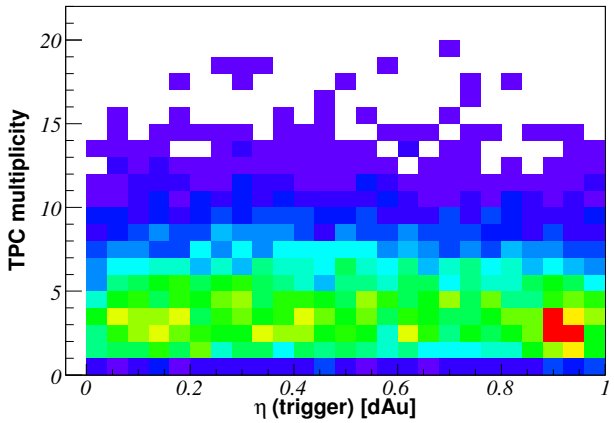

Figure 4.8: 2D distribution showing the TPC track-multiplicity with $p_t > 1$ GeV potted against the η's of trigger clusters from BEMC in dAu collisions.

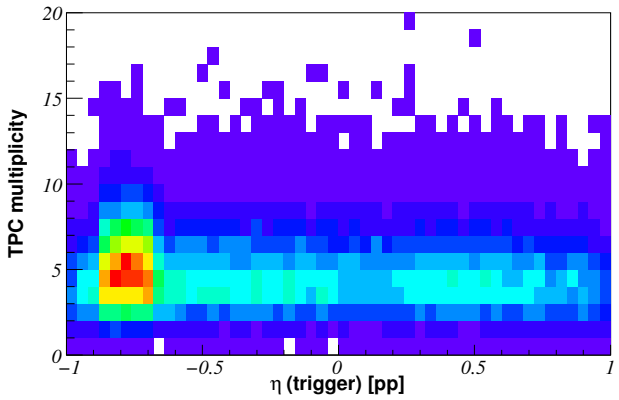

Figure 4.9: 2D distribution showing the TPC track-multiplicity with $p_t > 1$ GeV potted against the η's of trigger clusters from BEMC in pp collisions.

tracks corresponding to various η's of the triggered clusters. A patch is seen on a negative high η-region of trigger particles in pp collisions, where TPC track multiplicity is low. This patch of relatively larger entries of trigger π^0's indicate a noisy region. It is therefore necessary to make a selection on η region. From the kinematics point of view, the selection of η region for a specific range of p_t is also significant since it choses different x ($= \frac{2p_t}{\sqrt{s}}e^{-\eta}$) region. We have therefore used $|\eta|(trigger) < 0.7$ for trigger particles. The same range of η is taken for both in π^0-ch and ch-ch analysis.

Vetoing of the BEMC clusters by projecting the charged tracks

The composition of the jet fragments can be summarized as,

neutral particles :- mostly π^0, η, γ, where $\approx 90\%$ are coming from π^0.

charged particles :- mostly $\pi^{\pm}$, $K^{\pm}$, $e^{\pm}$, where $> 90\%$ are from $\pi^{\pm}$.

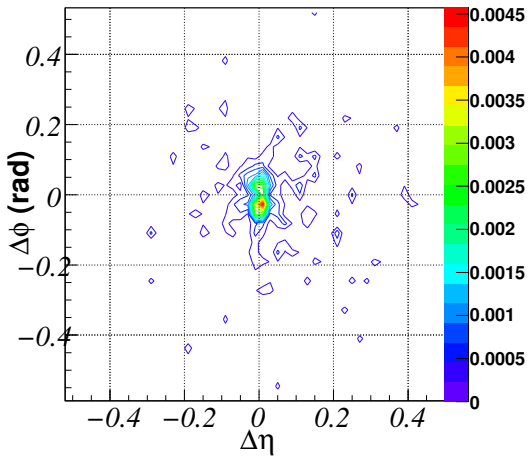

Figure 4.10: $\Delta\eta$-$Delta\phi$ correleration between the neutral cluster and the associated charged tracks ($p_t^{asso} > 1$ GeV) before removal of towers by projected track matching.

BEMC responds to the neutral particles like π^0, η and γ but the interactions of the charged particles in the calorimeter produces ∼10 % of the total signals. These charged particles are electrons and a smaller fraction is from charged

hadrons, which deposit energy via electromagnetic and hadronic shower formations respectively. A cluster is vetoed if a charged track projected from TPC is pointed to the center of the cluster. The Fig. 4.10 shows the distribution of $\Delta\phi = \phi_{tower} - \phi_{track(p_t>1.0GeV)}$ vs. $\Delta\eta = \eta_{tower} - \eta_{track(p_t>1.0GeV)}$ for all the towers. It is seen that tracks are projected mostly at the center of the cluster thereby making the vetoing more effective. The effect of rejection of towers on the basis of TPC track projection can have two effects in terms of minimization of systematic errors. Firstly the contribution of the electrons and charged tracks to the trigger particles is reduced. Secondly, the removal of the energy of the charged tracks from the neutral cluster energy improves the energy resolution [139]. There might be some effect on imposing the vetoing criteria in terms of the yield in near side. This effect will be discussed later.

4.2.5 Cluster versus tower for trigger selection and systematic error

A tower with $E_t > 4.5$ GeV is taken as the seed for cluster finding. Starting from the highest E_t-tower as seed, upto three adjacent towers with non-zero energy deposition are taken as members of the cluster. It is found [139] that the energy is underestimated by about 14% for neutral pions and 9% for single photons when we take energy deposition on the highest tower in the cluster. The energy content of the cluster is ∼99% of the incident π^0 for clusters of maximum size of four towers.

For estimating the systematic errors due to the selection of trigger candidate on various quantities extracted in this analysis, we have adopted two approaches for obtaining the trigger tower:, one based on cluster and the second one based on high tower. The energy difference is ≈ 10% on two approaches as shown in Fig. 4.11. Taking into account the leakage of energy from high towers to its neighbors, the difference in yields in two analyses are taken as a systematic error involved from the analysis technique. This systematic error is below 5% for most of the cases while going from lower to higher E_t^{trig} both for near and away-side correlation peaks. However, systematic errors involved for $E_t^{trig}>$ 8.5 GeV/c and $p_t^{asso} > 1$ GeV/c are larger. Errors on widths and therefore on $\sqrt{\langle j_t^2 \rangle}$ and $\sqrt{\langle k_t^2 \rangle}$ are less than 5%. Relative systematic uncertainty in the reconstruction efficiency is of the order of 5 which affects the yields.

Errors shown in all the figures are statistical only. The errors are larger for higher E_t^{trig} and p_t^{asso} as the statistics reduces. Systematic errors for π^0-charged

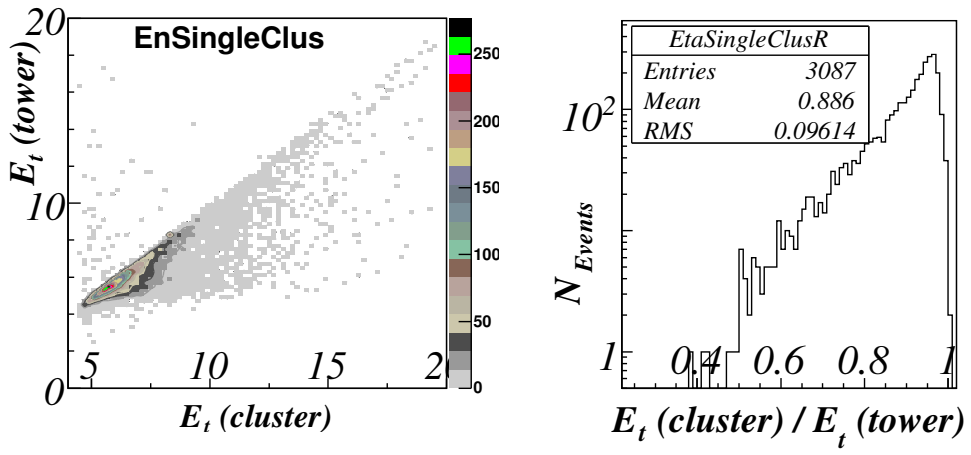

Figure 4.11: E_t in the cluster vs. the E_t of the trigger tower in corresponding clusters for pp-2006 data(left). The distribution of the the ratio of the π^0 energy in the two cases mentioned above shows an average 88% energy in a single tower.

correlations have been estimated from the following considerations apart form the sources mentioned earlier. (a) errors involved due to non-uniformity in EMC response (b) errors associated to the use of different analysis techniques. The non-uniformities in EMC response were minimized by excluding all towers which were giving relatively larger number of triggers ('hot towers'). The inclusion of the hot towers as trigger candidates mostly affect the associated particle yield as this quantity enters in the denominator of the correlation function. To test the effect further, we have subdivided the whole set of accepted modules in three categories with large enough statistics in each category to be able to make a stable conclusion. It was found that the systematic error obtained from the deviation of the mean yield in 3-category of modules is about 10%.

4.3 Dihadron correlation functions for pp and dAu

We discuss here the method and terminology we used in the analysis of two-particle azimuthal correlations. We denote the *trigger particle* as the parti-

cle/cluster having highest p_t^{trig} (or E_t^{trig}) in the event. The second particle in the pair referred to as the *associated particle* has to satisfy the condition $p_t^{threshold} < p_t^{asso} < p_t^{trig}$. As mentioned earlier, as a trigger particle we use either the cluster of towers in BEMC or the charged tracks from TPC. The associated particles are always charged particles measured by the TPC for both types of trigger particles. To explore the properties of the correlation function in detail, a large variety of p_t (E_t) cuts imposed on trigger and associated particles are used and discussed below.

The azimuthal correlation function for a combination of the trigger and associated particles is defined as

$$D(\Delta\phi) = \frac{1}{N_{trig}} \frac{1}{\epsilon} \int d(\Delta\eta) N(\Delta\phi, \Delta\eta), \tag{4.5}$$

where $\Delta\phi = \phi^{trig} - \phi^{asso}$, N_{trig} is the number of particles satisfying the conditions imposed on the trigger particle, and ϵ is the reconstruction efficiency of theassociated charged particles. For the p_t range of associated particles used in this analysis ($p_t > 1$ GeV/c) the reconstruction efficiency is about 89% independent of p_t and centrality.

4.3.1 Division of data in p_t^{trig} and p_t^{asso} bins

We mention below the division of the datasets used in this analysis according to the $p_t(E_t)$ of the trigger and associated particles.

π^0-charged particle correlations[3]

1. For studying the associated particle dependence of the correlation functions, we have taken the p_t^{asso} ranges of 1-2, 2-3, 3-4, 4-6 and 6-10 GeV/c for each E_t bin of 6.5-8.5, 8.5-10.5, 10.5-12.5 and 12.5-18.5 GeV/c

2. For studying the trigger E_t dependence, we have considered p_t^{asso} in the range $1.2 < p_{ta} < p_t^{trig}$ for E_t bin of 6.5-8.5, 8.5-10.5, 10.5-12.5 and 12.5-18.5 GeV/c.

Charged particle-charged particle correlations

p_t^{trig} bins of 2.5-4.5 4.5-6.5, 6.5-8.5 and 8.5-12.5 GeV/c are taken for studying the dependence on trigger particle p_t. p_t^{asso} is taken as $1.2 < p_{ta} < p_t^{trig}$.

[3]In the discussions to follow, we have sometime have sometimes used p_t^{trig} even for π^0-trigger particle. E_t^{trig} is however used always for neutral-cluster trigger.

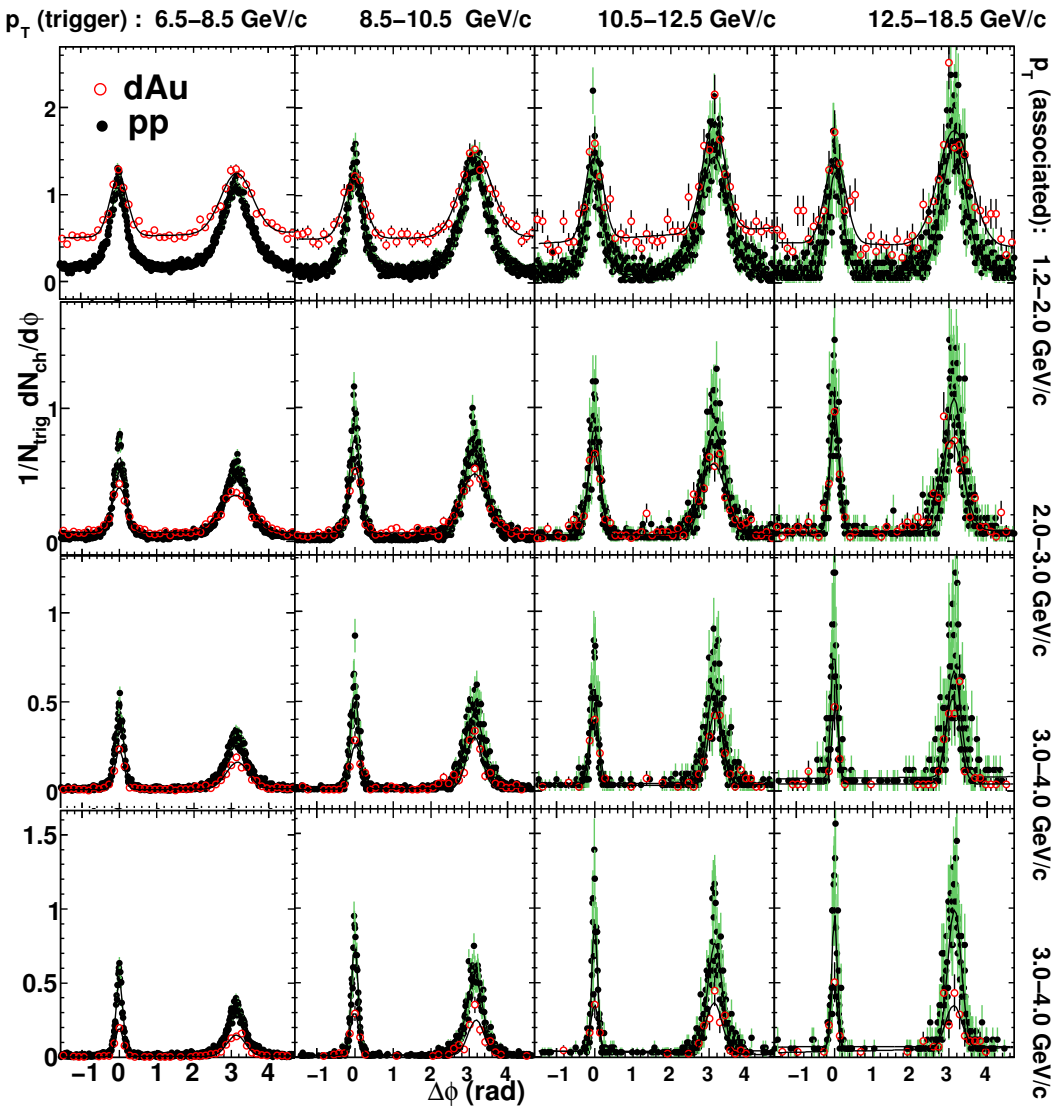

Figure 4.12: Raw correlation functions without background subtraction for d-Au (open circles) and p-p (solid circles). Four columns are for four trigger particle ranges 6.5-8.5, 8.5-10.5, 10.5-12.5 and 12.5-18.5 in GeV/c. Associated particles for each trigger particle bin are separated in 1.0-2.0, 2.0-3.0, 3.0-4.0 and 4.0-5.0 GeV/c in four rows. The correlation functions show two peaks, one on the near side of the trigger particle at $\Delta\phi = 0$ and the other at $\Delta\phi = \pi$. The correlation functions are fitted with a functional form comprising of 2-Gaussians and a linear function (**STAR Preliminary**).

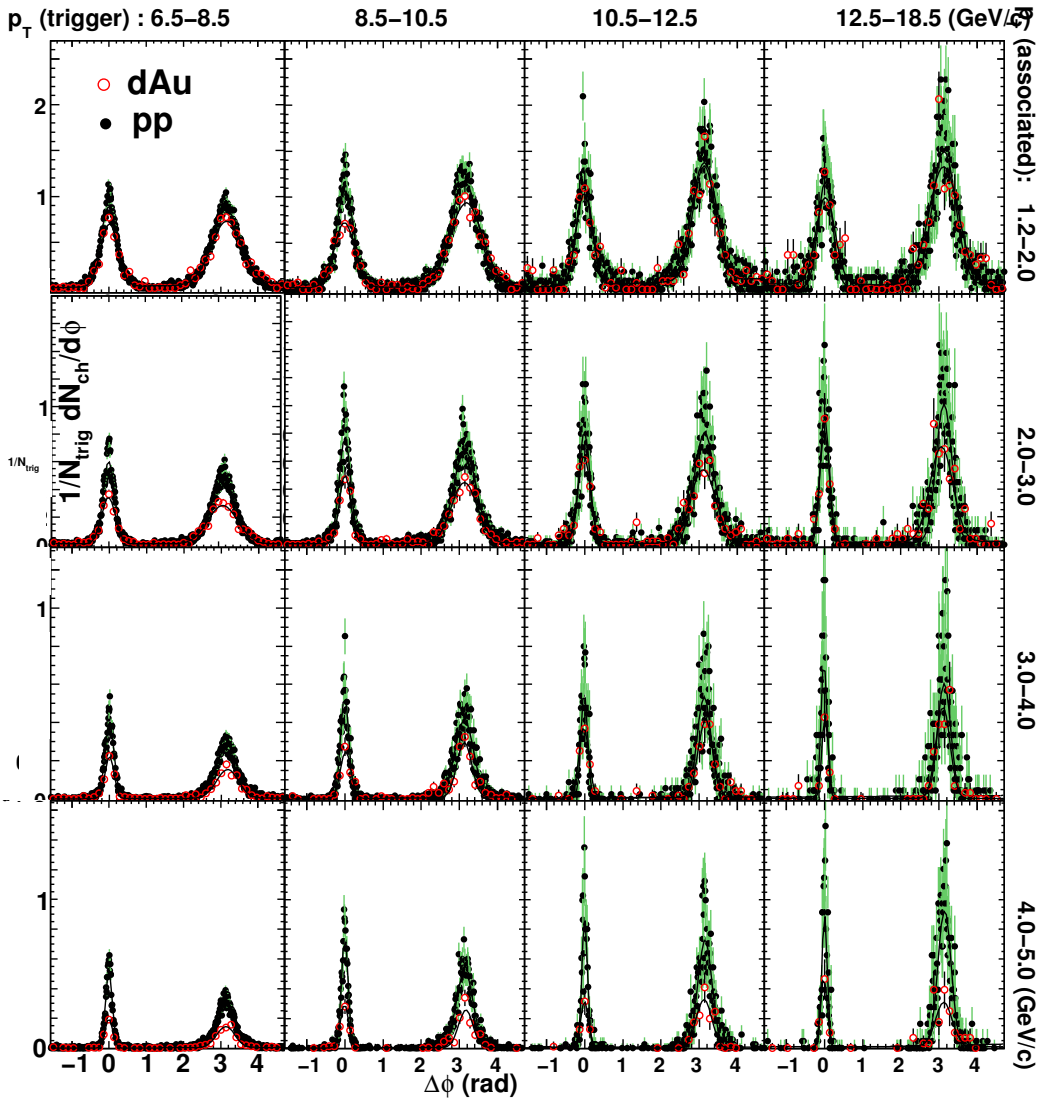

Figure 4.13: The constant background has been subtracted from the correlation functions (Fig.4.12) and the peaks have been extracted. The description of the plots are the same as with the raw correlation plot (Fig.4.12). The near and away side jet widths, and associated particle yields have been calculated from the fitted correlation functions (**STAR Preliminary**).

4.3.2 Correlation functions

Fig. 4.12 shows the π^0-ch correlation functions before background subtraction for pp and dAu collisions. The columns represent different $p_{t,trig}$ bins and the

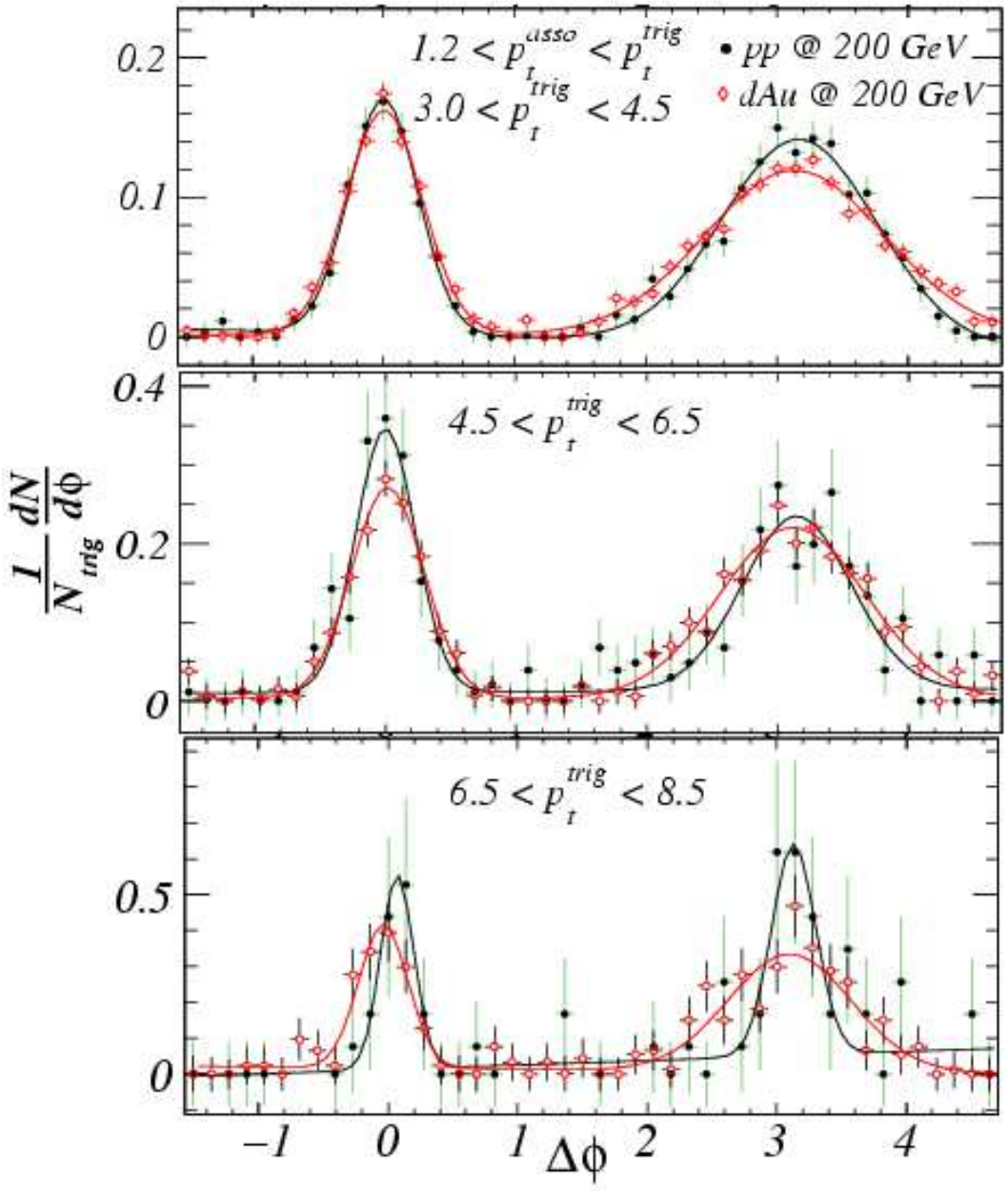

Figure 4.14: ch-ch correlation functions for pp and dAu after background subtraction (**STAR Preliminary**).

rows represent varying $p_{t,asso}$. The correlation functions show distinctly two peaks arising from the charged fragments of two hard scattered partons. The correlation functions are then fitted with the functional form

$$f(\Delta\phi) = Y_{near}\frac{e^{-(\Delta\phi)^2/2\sigma^2_{near}}}{\sqrt{2\pi}\sigma_{near}} + Y_{away}\frac{e^{-(\Delta\phi-\pi)^2/2\sigma^2_{away}}}{\sqrt{2\pi}\sigma_{away}} + B \qquad (4.6)$$

where B represents the combinatorial background from the underlying events and the peaks are the contributions from di-jets. Due to the production of softer particles by participant scaling, the background is higher for dAu collisions and reduces with higher p_t^{asso}, the region being dominated by jets. Fig. 4.13 represents the background-subtracted correlation functions for pp and dAu collisions. Fig. 4.14 shows the charged-charged correlation functions for pp and dAu data superposed to each other.

4.3.3 Width of the correlation functions

For extracting the additional information related to the properties of di-jets in pp and dAu collisions, we studied the width and per trigger associated particle yield for near and away side correlation peaks for different systems. Fig. 4.15 and Fig. 4.16 represent the variations of the width with p_t^{asso} and p_t^{trig} respectively for both the near and away side peaks. The away-side peaks are wider compared to those of the near side due to the fact that,

1. the near side jets always carry the high p_t trigger particle parting considerable amount of the jet energy in contrary to the unbiased nature of fragmentation of the away side-jet, and

2. relative position of the away-side jet axis with respect to the axis of the near side jet has an acoplanarity factor defined by the intrinsic k_t and its smearing.

As expected from the considerations of fragmentation, widths get reduced with p_t^{asso}, since the high-p_t component of the fragments lie closer to the jet axis.

Widths for the same p_t^{asso} systematically increase with increasing p_t^{trig} for both near and away side peaks. Our π^0-ch results are overlaid in Fig. 4.15 and Fig. 4.16 to the correlation results from PHENIX and ch-ch correlation results from STAR. As shown in the figure, the reach of $p_t^{trig}$is extended considerably by the present π^0-ch correlation results.

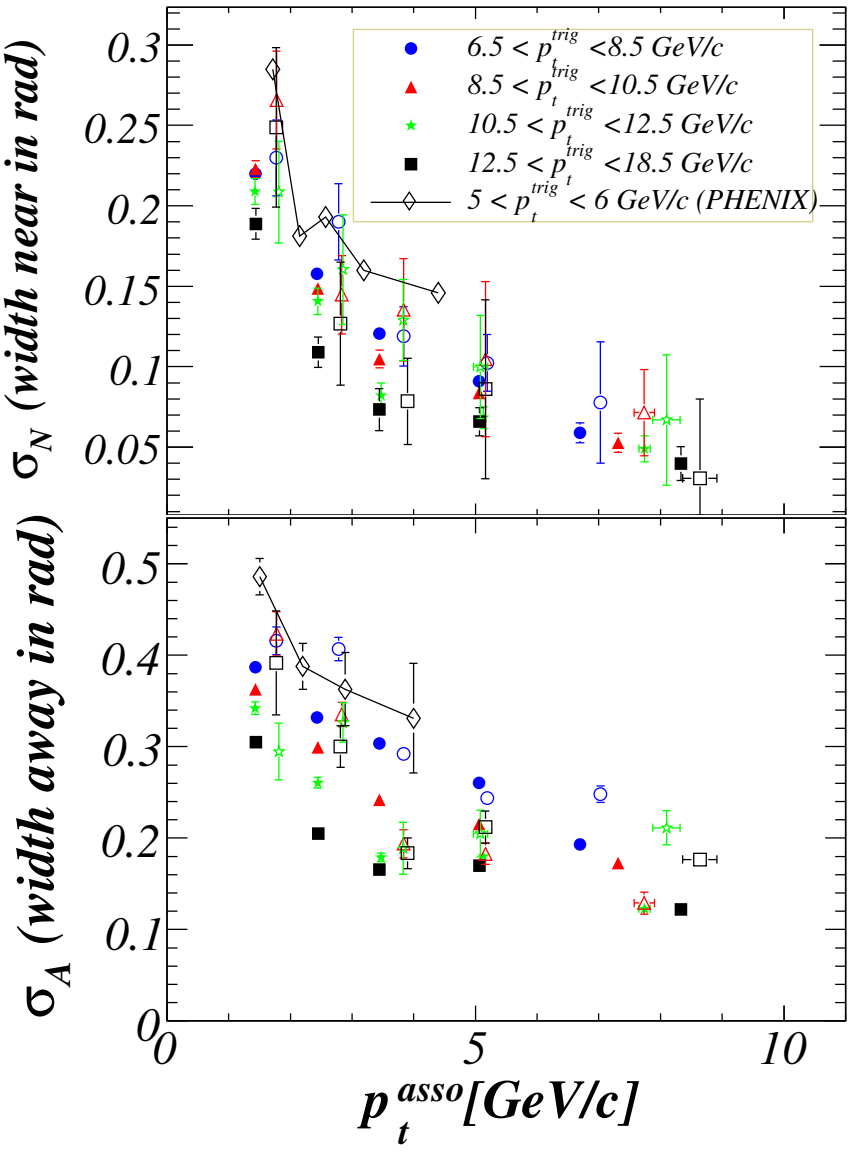

Figure 4.15: Widths of the near and the away side jet peaks as a function of the p_t^{asso}. For both near and away side peaks, the width decreases with p_t(associated) indicating the more energetic particles are lying close to the jet axis (**STAR Preliminary**).

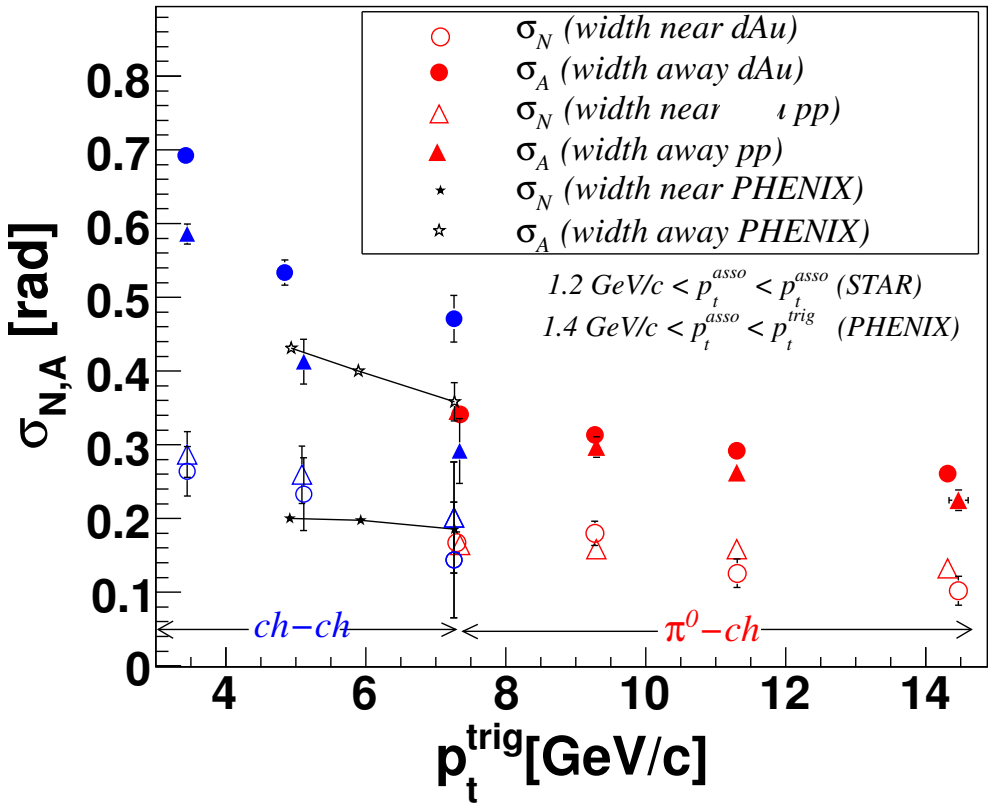

Figure 4.16: Widths of the near and the away side jet peaks as a function of p_t^{trig} (**STAR Preliminary**).

4.3.4 Associated particle yields of the near and away side jets

Another parameter which quantifies the effect of the formation of jets is the per-trigger associated particle yield. While the yield represents the multiplicity of the produced charged particles due to fragmentation, widths represent the cone in which the fragments lie. A possible modification of the per-particle yield might be expected for the partons while passing through the nucleus. As shown in Fig. 4.17 and Fig. 4.18, per-trigger yield increases with $p_t^{trig}$and reduces with p_t^{asso} . Higher p_t^{trig} represents higher-energy jets giving higher yield and lower yield with increasing p_t^{asso} shows the typical fragmentation function with lower yield at higher Z = p_t^{asso}/p_t^{trig}. The rate of increase of near side yield is relatively small compared to that of the away side because the

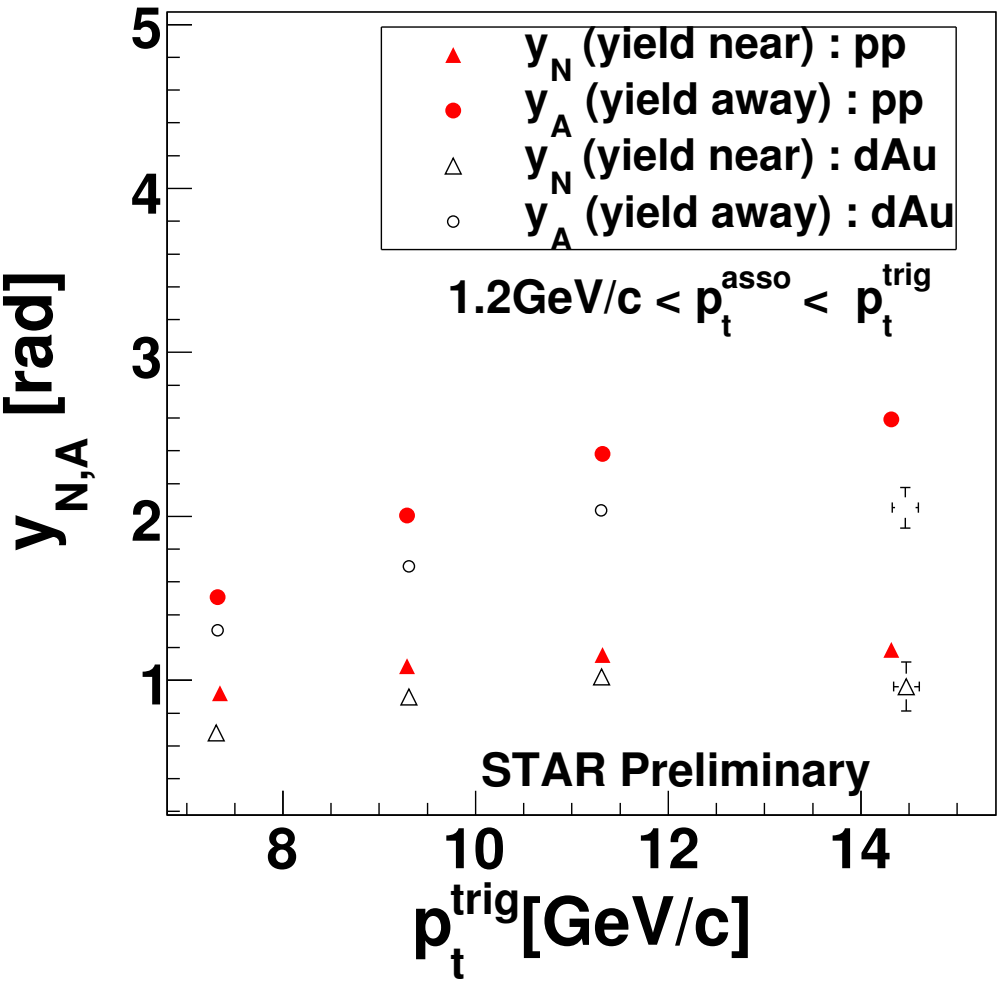

Figure 4.17: Per trigger associated particle yield as a function of the p_t of the trigger particles. Yield increases with p_t^{trig} for higher energy jets (**STAR Preliminary**).

trigger particles carry a larger fraction of the near side jet energy. There is no noticeable difference between the pp and dAu yields ruling out any major modification of jets in dAu.

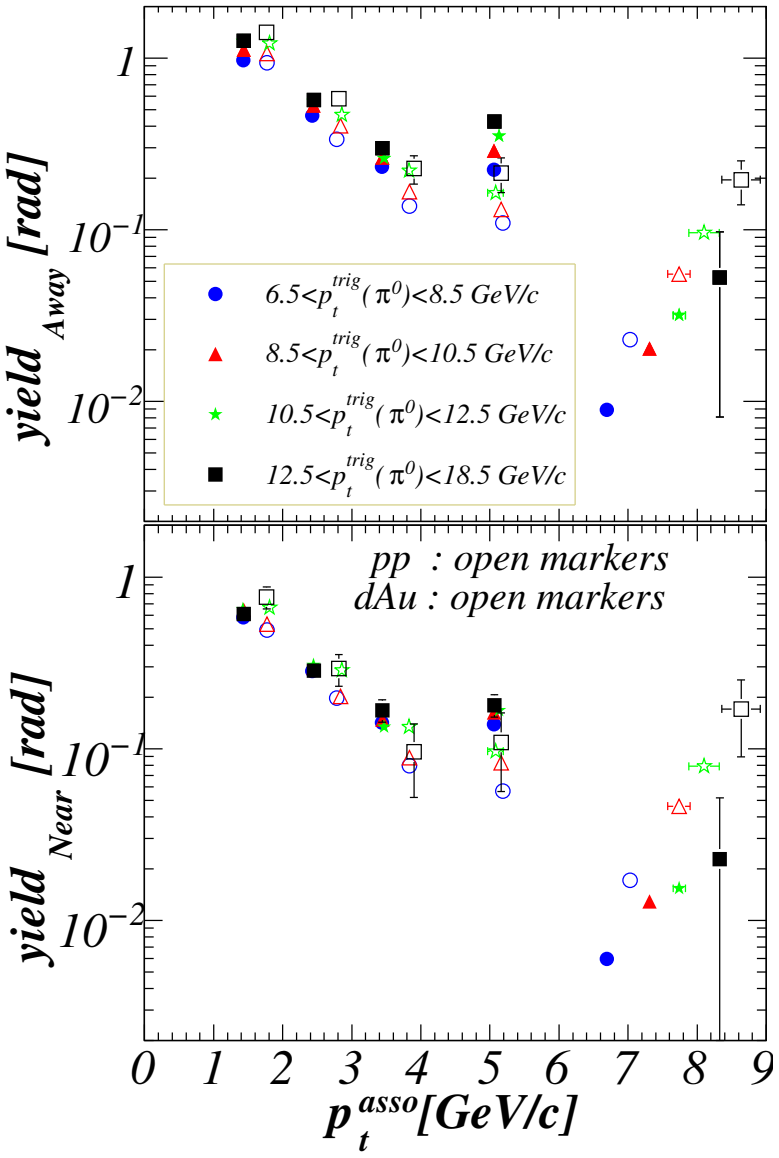

Figure 4.18: Per trigger associated particle yield as a function of the p_t of the associated particles for pp and dAu (pp in open markers and dAu in closed markers). Yield decreases with p_t^{asso} both for pp and dAu indicating the Z-dependence of the fragmentation function (**STAR Preliminary**).

4.3.5 $\sqrt{\langle j_t^2 \rangle}$

The average transverse momentum of the fragments of a jet perpendicular to the jet axis, $\sqrt{\langle j_t^2 \rangle}$ is calculated according to the equation 4.2 using the respective widths from the gaussian fitted correlation functions. Fig. 4.19 shows the variation of $\sqrt{\langle j_t^2 \rangle}$ with p_t^{asso} (top) and p_t^{trig} (bottom) for pp and dAu collisions. Dependency of the $\sqrt{\langle j_t^2 \rangle}$ with p_t^{asso} (top) is given for the four region of trigger particle p_t. The open symbols is for the dAu collisions where the X-axis is shifted by +0.2 GeV/c for better visualization. As shown in the data, $\sqrt{\langle j_t^2 \rangle}$ is similar in magnitude for pp and dAu collisions and both systems demonstrate the seagaul effect showing the increase of $\sqrt{\langle j_t^2 \rangle}$ with p_t^{asso} and saturation at a mean value of $\approx$ 600 MeV. The $\sqrt{\langle j_t^2 \rangle}$ alone with the stastical errors for pp and dAu datasets are given for the both $\pi^0 - ch$ and ch-ch triggered datasets in the table 4.2. The dataset consists of minimum bias and high tower datasets. $\sqrt{\langle j_t^2 \rangle}$ has been found to be somewhat lower for high tower datasets. The selection of trigger events with a given charged to neutral particle ratio might be responsible for the difference.

system	$\sqrt{\langle j_t^2 \rangle}$ ($\pi^0 - ch$) in MeV	$\sqrt{\langle j_t^2 \rangle}$ (ch-ch) in MeV
pp	576 $\pm$ 11	598 $\pm$ 28
dAu	513 $\pm$ 46	565 $\pm$ 44

Table 4.2: $\sqrt{\langle j_t^2 \rangle}$ values for pp and dAu

4.3.6 $\sqrt{\langle k^{s2}_t \rangle}$

The acoplanarity of the hard scattered partons, appears as $p_{out} = p_t^{asso} \sin(\Delta\phi)$ in di-hadron correlations. Using eq. 4.4 and $\sqrt{\langle j_t^2 \rangle}$, $\sqrt{k^{s2}_t}$ is calculated for pp and dAu dataset. Fig. 4.20 shows $\sqrt{k^{s2}_t}$ with respect to p_t^{asso} and p_t^{trig} as extracted using eq. 4.4 and $\sqrt{\langle j_t^2 \rangle}$. The acoplanarity obtained here is folded with the two fragmentation parameters $\langle \hat{x}_h \rangle^{-1}$ and $\langle z_t \rangle$, which are strongly dependent on the p_t^{asso} value since high p_t particles reflect the jet direction more precisely . Therefore for low p_t^{asso} , the acoplanarity factor increases as shown in Fig. 4.20 (top). If the fragmentation functions in pp and dAu collisions are assumed to be same form the relative difference of $\sqrt{\langle k^{s2}_t \rangle}$ (dAu-pp) can be used to quantify the effect of the nuclear matter in k_t broadening.

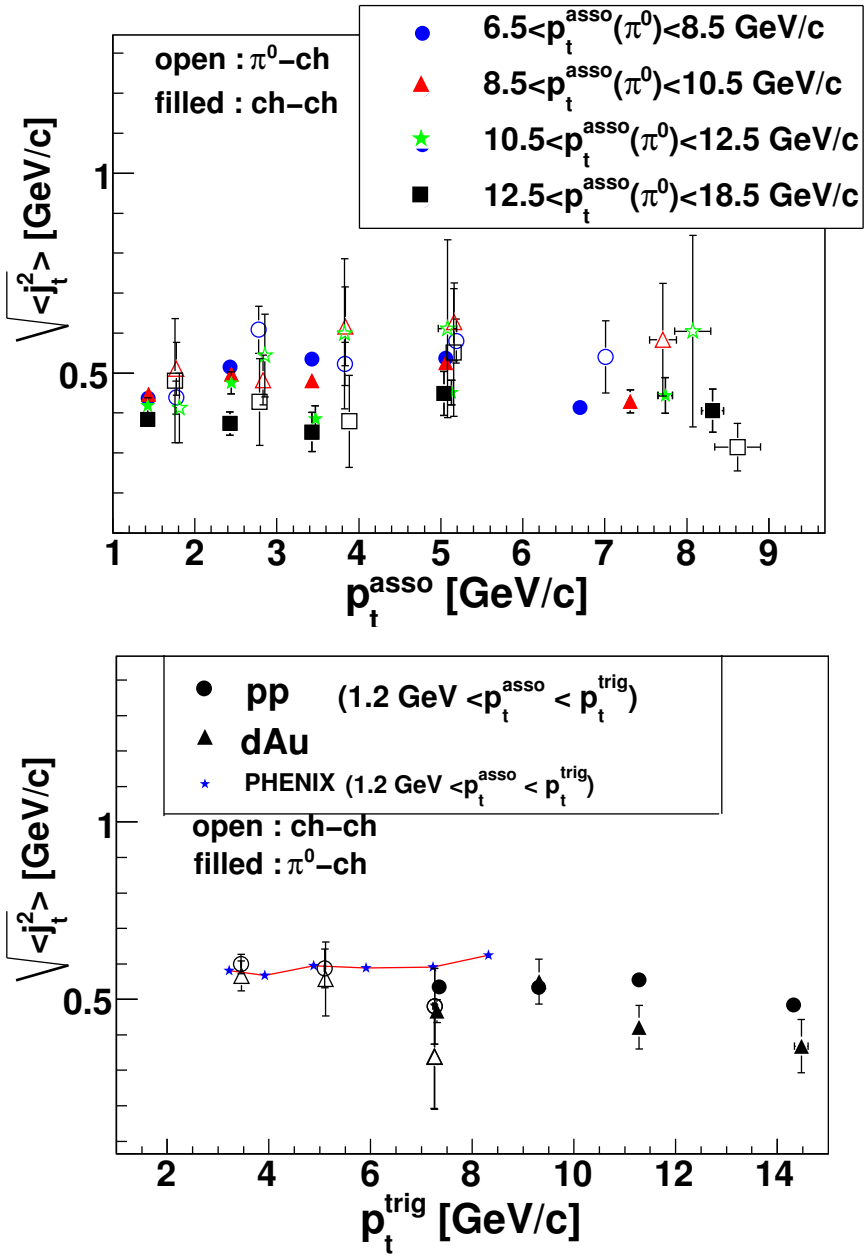

Figure 4.19: Variation of $\sqrt{\langle j_t^2 \rangle}$ with p_t^{asso} (top panel) for three p_t^{trig} bins. Variation of $\sqrt{\langle j_t^2 \rangle}$ with p_t^{trig} is shown in the bottom panel (**STAR Preliminary**).

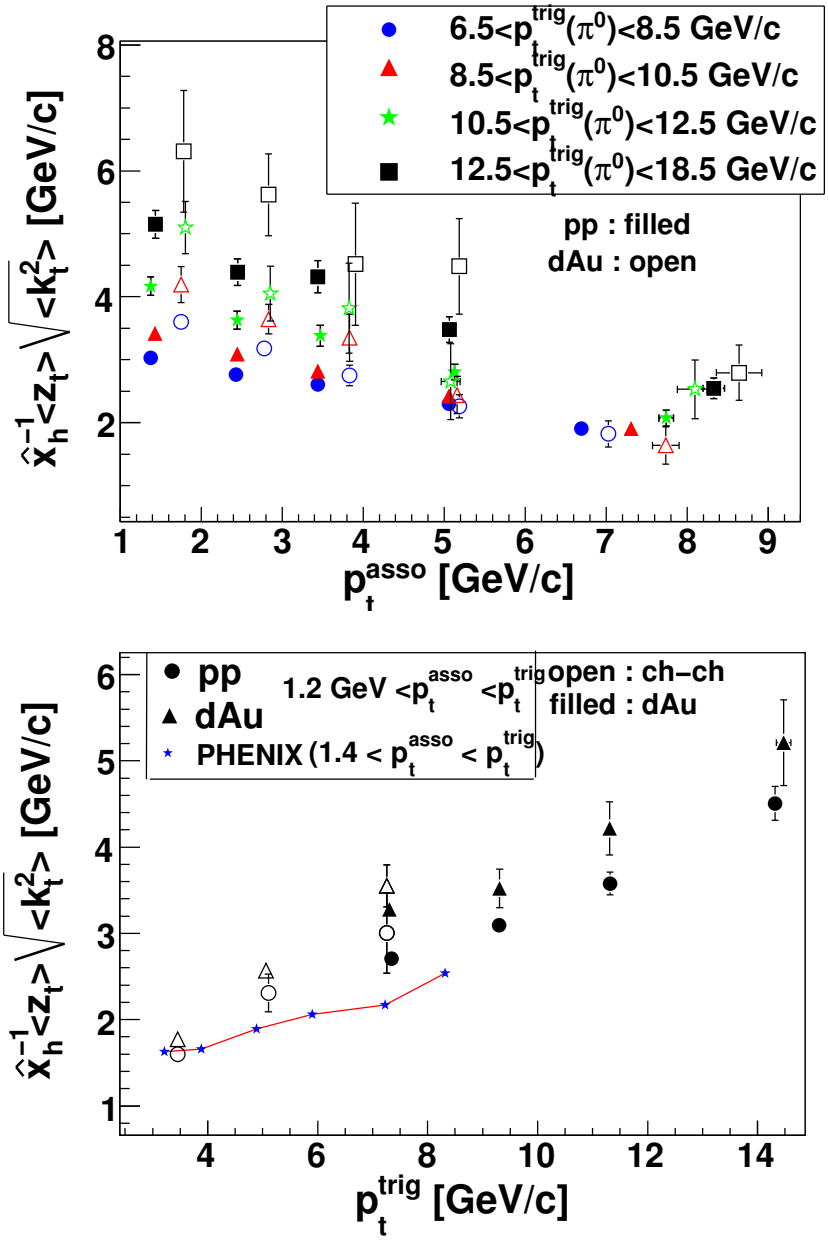

Figure 4.20: Variation of $\sqrt{\langle k_t^{s2}\rangle}$ with p_t^{asso} (top) for the three p_t^{trig} bins. Variation of $\sqrt{\langle k_t^{s2}\rangle}$ with p_t^{trig} is shown in the bottom figure (**STAR Preliminary**).

4.3.7 Correction factors for extracting $\sqrt{\langle k_t^2 \rangle}$

The correction factors needed for obtaining $\sqrt{\langle k_t^2 \rangle}$ from $\sqrt{\langle k^{s2}_t \rangle}$ are obtained by using PYTHIA event generator. PYTHIA is an event generator based on the Lund string fragmentation model [121]. We use PYTHIA for generating 2→2 hard scattering processes. In HT datasets, we are selecting a specific kinematic region objects and the simulated dataset has been generated accordingly. This has been guaranteed by matching the trigger-particle p_t distributions from simulation and data.

p_t-hard	7-9 GeV/c	9-11 GeV/c	11-15 GeV/c	15-25 GeV/c	25-35 GeV/c
x-section	2.299×10^{-02}	5.504×10^{-03}	2.220×10^{-03}	3.895×10^{-04}	1.021×10^{-05}

Table 4.3: x-section at different p_T hard bins.

As per production x-section as shown in table 4.3, high p_t trigger bins have a smaller event statistics compared to the low p_t bins. Therefore for obtaining x_h^{-1} and $\langle z_t(k_t, x_h) \rangle$ with small errors at high p_t bins, we have generated sufficient simulated datasets at different jet p_t bins. Simulated datasets generated in different p_t-hard bins (7-9, 9-11, 11-15, 15-25, 25-35 GeV/c) and the corresponding x-sections are shown in the table. 4.3. We have then followed a procedure where we first calculated the correction factors for corresponding p_t-hard bins and then obtained a weighted correction factor by collecting all the factors in various p_t-hard bins, as per eq. 4.7 below,

$$f = (f_1 \times x_1 + f_2 \times x_2 + f_3 \times x_3 + ..)/(x_1 + x_2 + x_3 + ..) \qquad (4.7)$$

$f_1, f_2, f_3,$ ..... are the correction factors and $x_1, x_2, x_3,$ .... are the relative x-sections for different p_t-hard bins. Fig.4.21, Fig.4.22 and Fig. 4.23 show the variations of $\langle z_t \rangle$ and $\langle \hat{x}_h \rangle^{-1}$ and $\langle z_t \rangle \times \langle \hat{x}_h \rangle^{-1}$ as a function of p_t^{trig} for all the p_t-hard bins. The reach of p_t^{trig} for a particular bin extends maximum upto the upper limit of the $p_t{}^{hard}$ bin.

While calculating the correction factors using the above mentioned five bins, we find a jump in the value of *"f"* $= \langle x_h \rangle^{-1} \times \langle z_t(k_t, x_h) \rangle$ as shown in Fig. 4.24 while crossing from one p_t-hard bin to the other. It happens due to the fact that *"f"* follows the lowest p_t-hard bins available in the p_t trigger ranges.

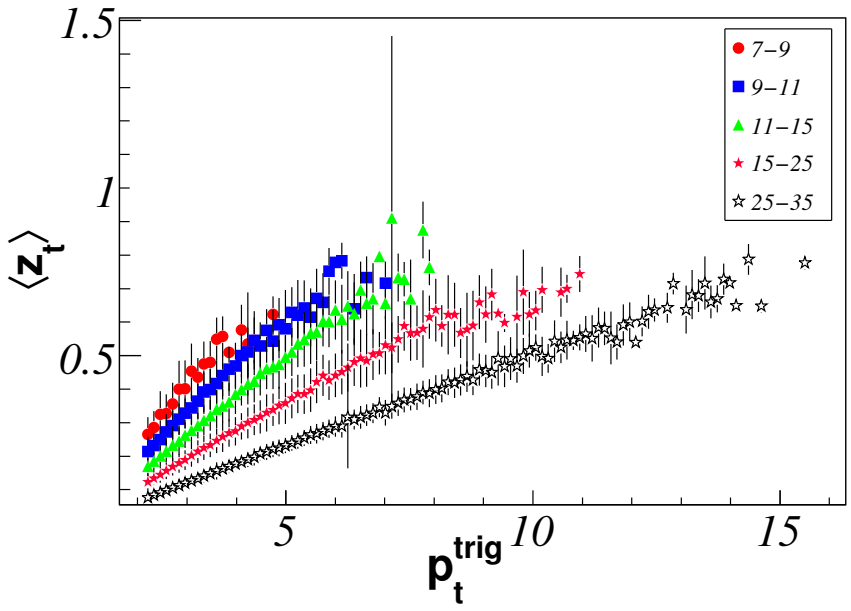

Figure 4.21: z_t obtained in five p_t hard bins.

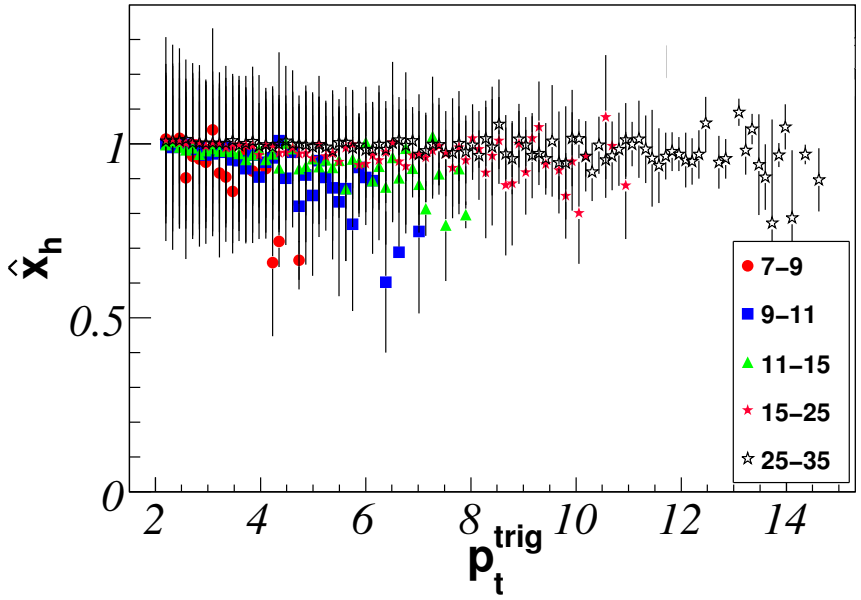

Figure 4.22: $\langle \hat{x}_h \rangle$ in five p_t-hard bins as obtained from the PYTHIA simulations.

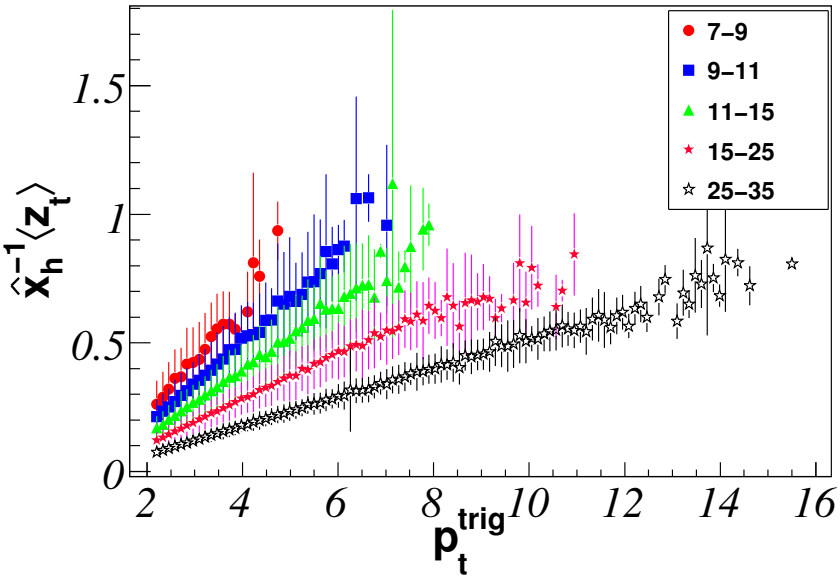

Figure 4.23: $\langle z_t \rangle \times \langle \hat{x}_h \rangle^{-1}$ in five p_t-hard bins.

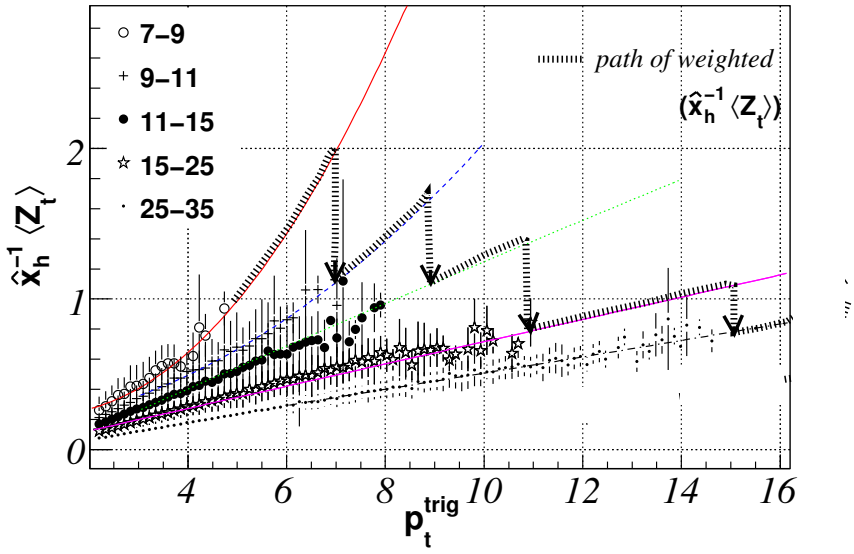

Figure 4.24: The schematic of $\langle Z_t \rangle \times \langle \hat{x}_h \rangle^{-1}$ summed over p_t-hard bins. The path followed by $\langle Z_t \rangle \times \langle \hat{x}_h \rangle^{-1}$ having a discrete jump at the end of the each bin.

The *"f"* values at various p_t^{trig} are therefore parametrized as a function of p_t-trigger for obtaining the small size p_t-hard bins as follows :

Step-I (fitting $\langle x_h \rangle^{-1} \times \langle z_t \rangle$ vs. p_t^{trig}) : Polynomial of degree two ($f = a_0 + a_1 x + a_2 x^2$) has been used for the points in each of the p_t-hard bins.

Step-II (a_0, a_1 *and* a_2) : Dependency of a_0, a_1, *and* a_2 as a function of the p_t hard bin has been studied (where the upper limit in p_t^{hard} bin is taken as the value in X-axis), where a_0, a_1 *and* a_2 are fitted with degree of polynomial-2. In this step therefore, we obtain a relation for getting the correction factor "f" as a function of upper limit of p_t^{hard} bin.

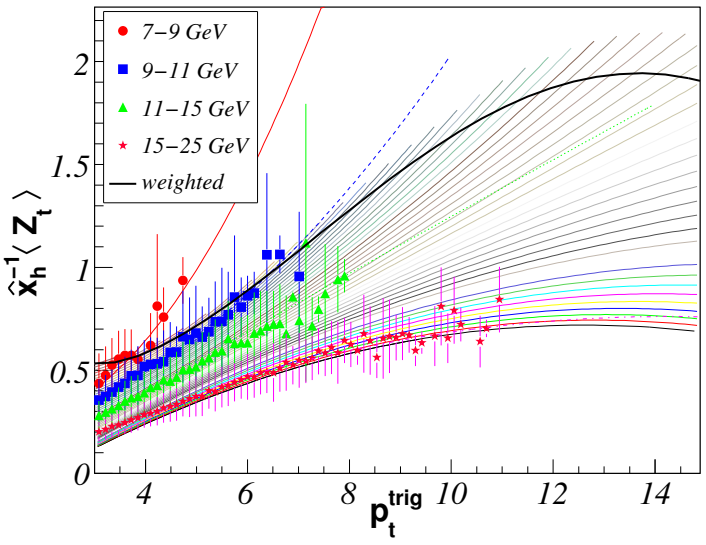

Figure 4.25: Method of extraction of the correction factors from PYTHIA. Events are generated in the five bins of $p_t{}^{hard}$. The parameters from the p_t^{trig}-trigger dependent correction factors with p_t^{trig} are used to generate a set of distributions with very fine bin interval in p_t^{trig} (shown by a set of lines). Final weighted correction factor is obtained from this set of continuous lines.

Step-III ($\langle x_h \rangle^{-1} \times \langle z_t \rangle$ at smaller p_t-hard bins) : This is a reverse procedure. For any upper limit of the p_t-hard bins (bin size $\rightarrow$ 0), a_0, a_1 and a_2 and thereby the correction factors can be found from parameterization in step-II. Finally the x-section weighed *"f"* for nearly continuous limit have been extracted using eq. 4.7. The solid lines in Fig. 4.25 shows the final values.

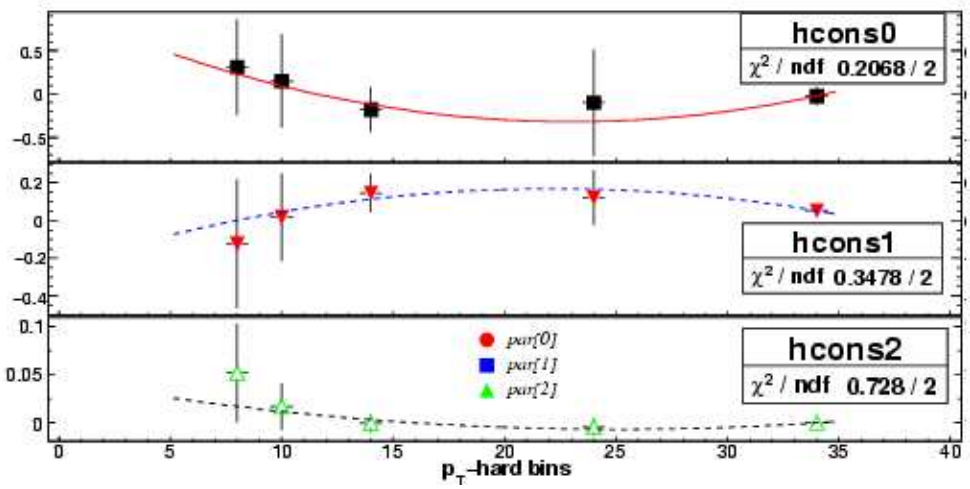

Figure 4.26: a_0 (top), a_1 (middle) and a_2(bottom) for all the p_t-hard bins for fitting $\langle x_h \rangle^{-1} \times \langle z_t(k_t, x_h) \rangle$ with polynomials of degree-2. This is for a specific case (pol2-pol2) where a_0, a_1 and a_2 are fitted again with pol2.

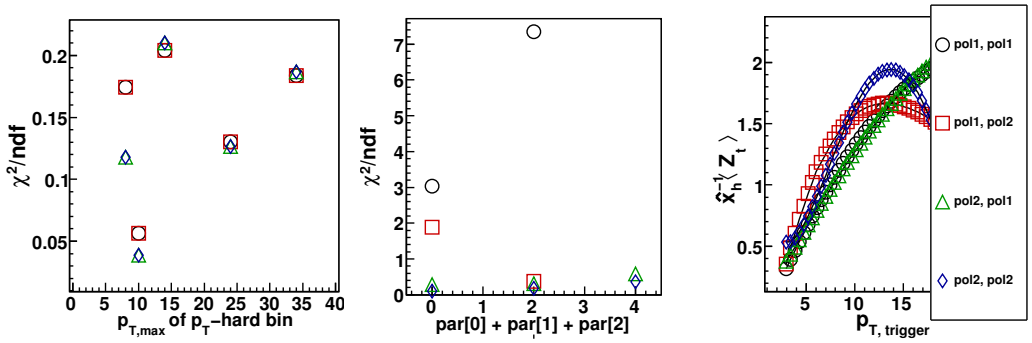

Figure 4.27: χ^2/NDF for all four ways of fitting and the combination of the results for the cases, pol2-pol2 and pol2-pol1 are taken for the analysis.

Step-IV (Systematics from fittings) : Fitting the functions is the step-I is dome with polinomial of degree-1 and degree-2. Similarly the corresponding fit parameter-functions (a_0, a_1 and a_2) in step-2 is fitted with with polinomial of degree-1 and degree-2. Thus fitting can be done in four ways (pol1-pol1, pol1-pol2, pol2-pol1 and pol2-pol2). Fig. 4.26 shows the parameters a_0, a_1 and a_2 in pol2-pol2 case and Fig. 4.27 (right) shows

the final values in all the cases. Fig. 4.27 (left and middle) shows the χ^2/NDF vlaues for all the cases.

p_t^{trig}	3.5	4.5	5.5	6.5	7.5	8.5	9.5	10.5	11.5	12.5	13.5	14.5
f	2.02	1.63	1.32	1.09	0.93	0.81	0.72	0.65	0.61	0.57	0.55	0.54
$f(sys)$	0.096	0.052	0.056	0.076	0.097	0.113	0.123	0.125	0.119	0.106	0.083	0.052

Table 4.4: The correction factors with systematic errors derived from the difference in pol2-pol2 and pol2-pol1 results

The table. 4.4 shows the correction factors with systematic errors derived from the difference in pol2-pol2 and pol2-pol1 results which have minimum χ^2/NDF as shown in Fig. 4.27. Fig. 4.28 shows the final values of $\sqrt{\langle k_t^2 \rangle}$ after ap-

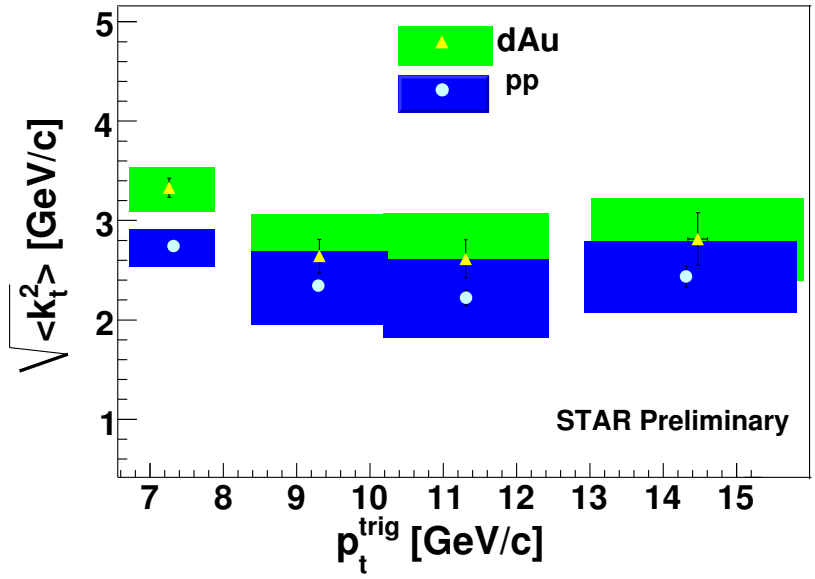

Figure 4.28: The final values of $\sqrt{\langle k_t^2 \rangle}$ for pp and dAu at $\sqrt{2}$ = 200 GeV after applying all corrections (**STAR Preliminary**).

plying all the corrections. Within the trigger range within p_t^{trig} = 6.5-18.5 GeV/c, we obtain $\sqrt{\langle k_t^2 \rangle}$ (pp) = 2.80±0.04(stat)±0.27(sys) and $\sqrt{\langle k_t^2 \rangle}$ (dAu) = 3.4±0.03(stat)±0.31(sys). This is ≈20 % enhacement in dAu compared

to pp. This is to be kept in mind that we have used the same fragmentation parameters for pp and dAu. The largest uncertainty enters in extracting $\sqrt{\langle k_t^2 \rangle}$ is from the fragmentation parameters. We have not made any attempt to apply different fragmentation functions for the two cases. Central

4.4 Centrality dependence of width, $\sqrt{\langle j_t^2 \rangle}$ and $\sqrt{\langle k^s{}_t^2 \rangle}$

The degree of multiple scattering in the nuclear medium (in dAu collisions) due to the interaction of the hard scattered partons can be studied by studying the jet properties as a function of the centrality of the collisions. collisions are

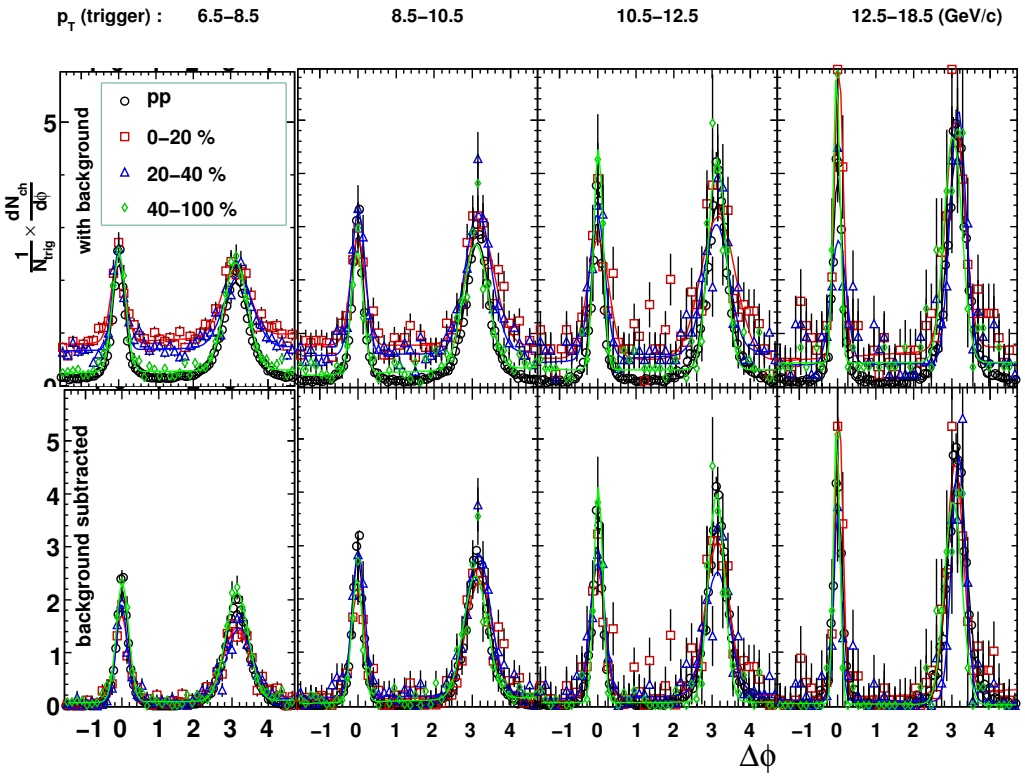

Figure 4.29: Correlation functions for dAu at different centralities (**STAR Preliminary**).

centrality	0-20%	20-40%	40-100%
FTPC east ref. Mult.(r)	r≥17	10≤r<17	r<10

Table 4.5: Reference multiplicity for dAu collisions based on FTPC-EAST reference multiplicity.

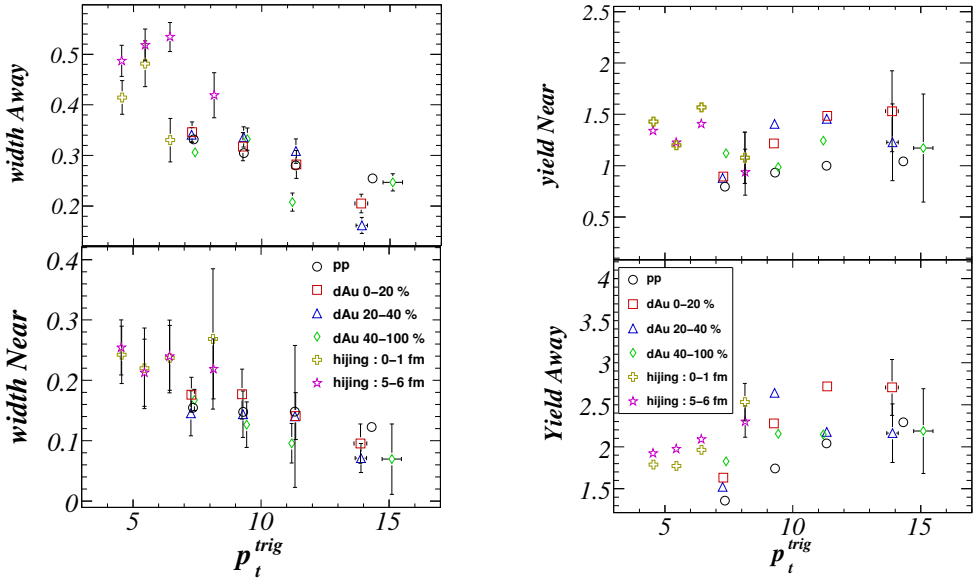

Figure 4.30: The centrality dependence of near and the away side correlation widths (left). The centrality dependence of the near and the away side jet yield(right) (**STAR Preliminary**). HIJING results are superposed in both the cases.

supposed to have more multiple scattering compared to that of the peripheral collisions, which might be reflected in the increase in width and broadening of $\sqrt{k^{s2}_t}$. The centrality in dAu datasets are determined from the Forward Time Projection Chamber in the East side of STAR (FTPC-east).

The FTPC-east reference multiplicity bins defining the centrality is shown in the table 4.5. We have used three centrality classes 0-20%, 20-40% and 40-100% as the most central, mid-central and peripheral collisions respectively. The correlation functions are shown in Fig. 4.29 for different centralities. We

have used four predefined p_t^{trig} ranges with $p_t^{asso} > 1.2$ GeV and pp results are superposed for comparison. For 0-20% centrality bin, the constant background is higher compared to the peripheral and pp cases, As shown in Fig. 4.30 $\sqrt{\langle j_t^2 \rangle}$ for all centralities remains same within error. The near side width, yield, and p_{out} behave alike. The awayside-yield and $\sqrt{k s_t^2}$ are found to be somewhat higher for 0-20% and 20-40% central cases compard to pp and 40-100%-centrality for the p_t^{trig} bin 6.5-8.5 GeV, showing at about (3.4-2.7)/2.7 $\sim$ 20% effect of nuclear modifications.

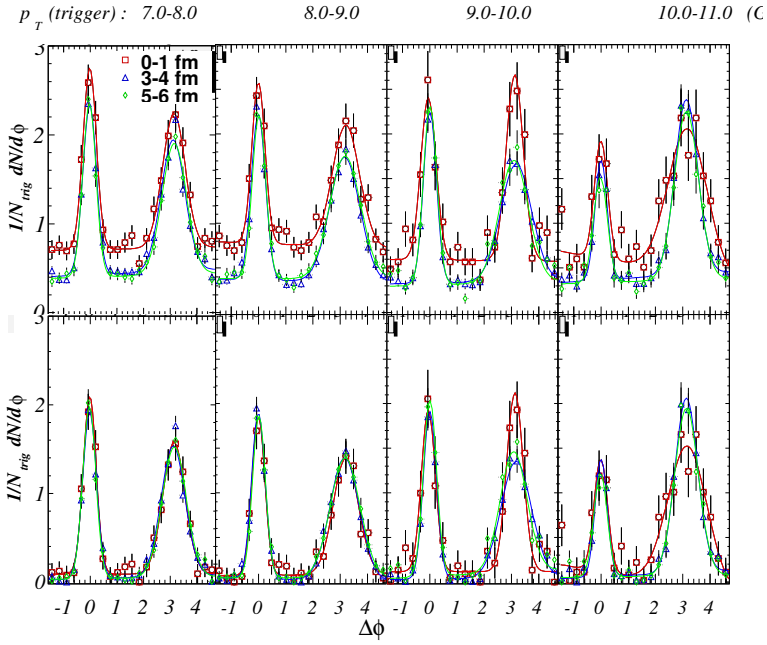

Figure 4.31: correlation functions with and without background subtraction for various impact parameters

4.5 Jet and correlation simulations with event generators

4.5.1 simulations with HIJING

HIJING event generator is used for dAu collisions with jet p_t set at 12.5 GeV at different impact parameters 0-1, 3-4, and 4-5 fm corresponding to the central to

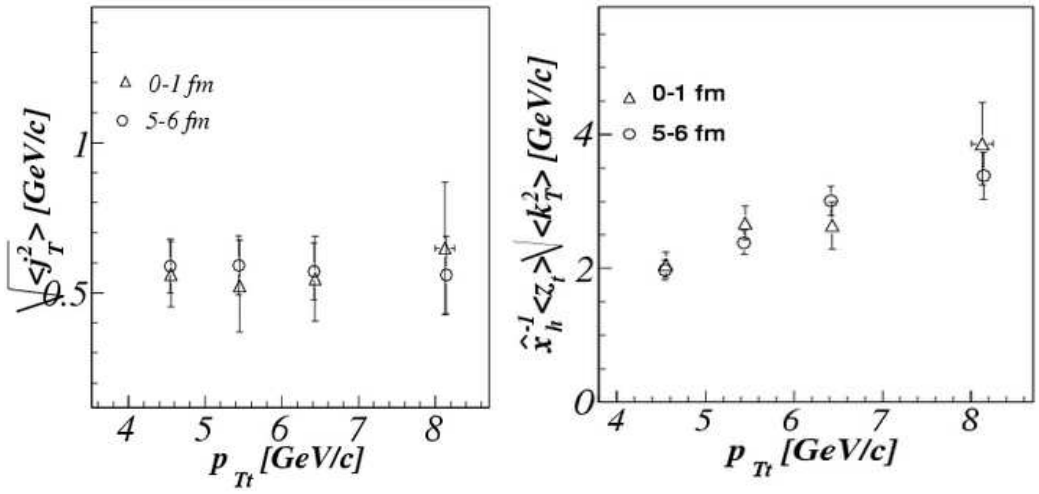

Figure 4.32: $\sqrt{\langle j_t^2 \rangle}$ (Left panel) and $\sqrt{k^{s2}_t}$ from HIJING for impact parameters 0-1 fm and 5-6 fm

peripheral collisions. HIJING does not contain multiple scatterings of partons in nuclear medium. The correlation function from simulation for different centralities is shown in Fig.4.31. $\sqrt{\langle j_t^2 \rangle}$ and $\sqrt{k^{s2}_t}$ for most central and peripheral collisions fall within error as shown in Fig.4.32.

4.5.2 $\sqrt{\langle k_t^2 \rangle}$ from PYTHIA with events passing di-jet selection criteria

The simulation is motivated to connect the results by correlation method to the results found from direct the jet reconstruction. Jet-jet processes were simulated in PYTHIA (version 6.2) for $\sqrt{s}$ = 200 GeV with jet $p_t^{hard} > 12.5$ GeV/c (CKIN(3)). The Fig. 4.33 shows the dominance of qg scattering events in the range 10 GeV/c $< E_t^{jet} <$ 30 GeV/c. Among three types of events (qq, qg and gg), gluon initiated jets are of main interest where the Fig. 4.34 shows that the trigger particles are more likely to originate from a quark (quark initiated jets fragment into harder particles).

There are several standard jet reconstruction algorithms like the iterative cone algorithm [141, 142], the midpoint cone algorithm [143, 144] and the inclusive k_t jet algorithm [144, 145] . Here we are reconstructing jets using basic principle of cone algorithm.

Di-jets are reconstructed with a cone radius R = 0.7 around two leading particles ($p_t > 1.2$ GeV/c) separated by at least 1.57 radians. We have therefore reconstructed the jets with following formalisms. With the charged particles within cone of radius, R = 0.7 (containg $N_{particles}$ paricles) we construct the jet energy and direction as follows.

$$E^{jet} = \sum_{i=0}^{N_{particles}} E_{t_i}$$
$$p_x^{jet} = \sum_{i=0}^{N_{particles}} psin(\theta_i)cos(\theta_i)$$
$$p_y^{jet} = \sum_{i=0}^{N_{particles}} psin(\theta_i)sin(\theta_i)$$
$$p_z^{jet} = \sum_{i=0}^{N_{particles}} pcos(\theta_i)$$
$$E^{jet} = \sum_{i=0}^{N_{particles}} E_{t_i}$$
$$p_x^{jet} = \sum_{i=0}^{N_{particles}} psin(\theta_i)cos(\theta_i)$$
$$p_y^{jet} = \sum_{i=0}^{N_{particles}} psin(\theta_i)sin(\theta_i)$$
$$p_z^{jet} = \sum_{i=0}^{N_{particles}} pcos(\theta_i)$$
$$p_t^{jet} = \sqrt{p_x^{jet^2} + p_y^{jet^2}}$$
$$\phi_{jet} = atan\frac{p_y^{jet}}{p_x^{jet}}$$
$$sin\phi_{jet} = \frac{p_t^{jet}}{\sqrt{p_x^{jet^2}+p_y^{jet^2}+p_z^{jet^2}}}$$
$$E_t^{jet} = E^{jet}sin\theta_{jet}$$

In PYTHIA-event-recording, we can identify the hard scattered partons which appear in the line number "6" and "7" in the particle list. We will indicate them as parton6 and parton7. Fig. 4.35 shows a summarized results on the jet reconstruction performance. It has been observed that for reconstructed jet energies above 10-12 GeV, $\approx$ 90% efficiency in the reconstructed jet energy

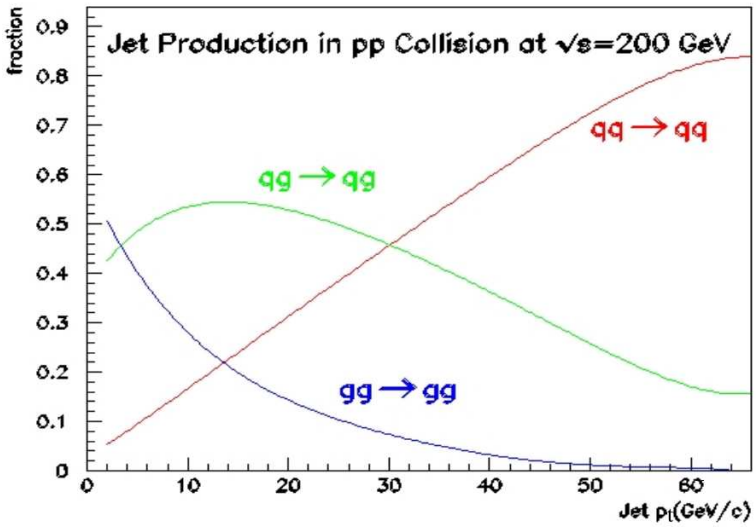

Figure 4.33: Different types of hard scattered processes as a function of the jet p_t as given by PYTHIA.

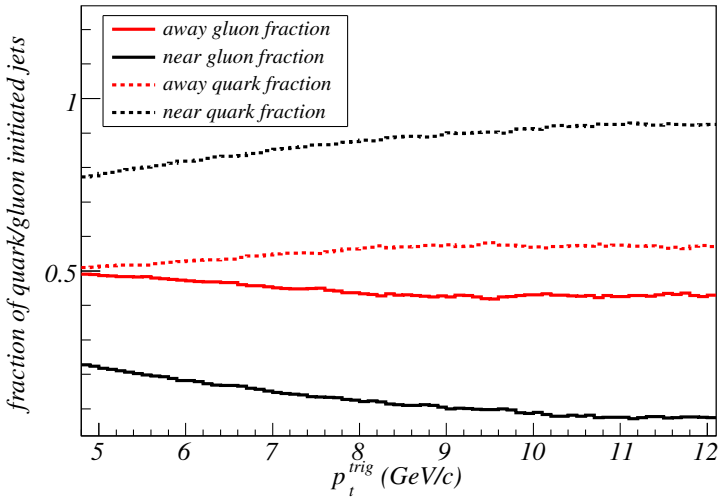

Figure 4.34: Fraction of jets generating the trigger particles (from PYTHIA).

can be achieved. Events are selected on the basis of di-jet energies and two ceses are considered and the correlation analysis is done for both the cases.

i) All the events having p_t^{trig} >6 GeV/c (before jet E_t cut).

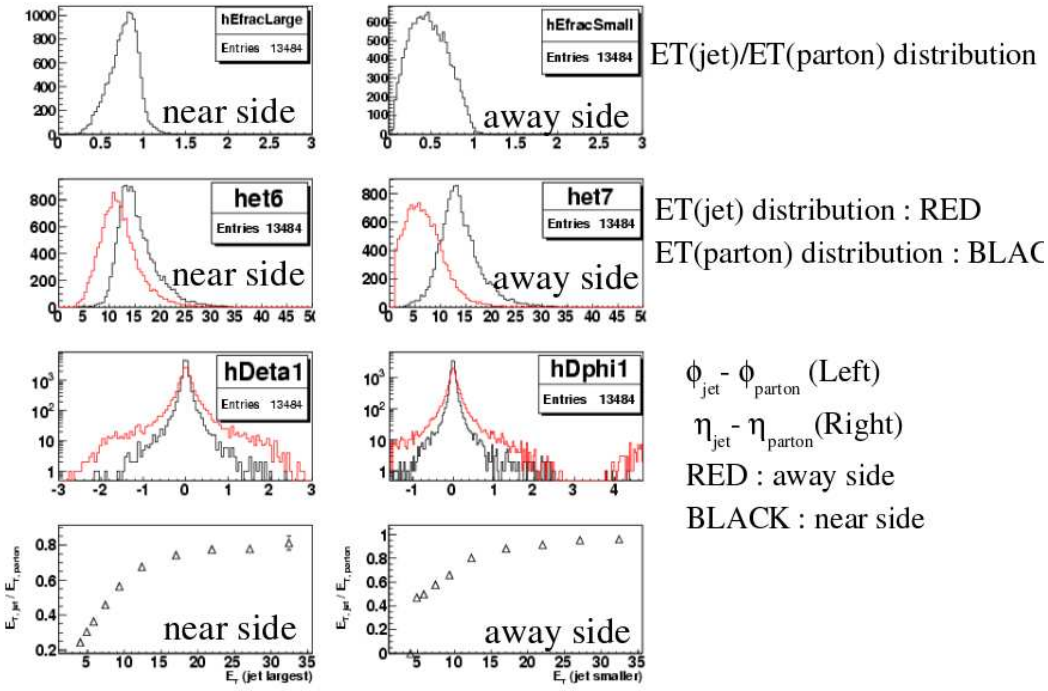

Figure 4.35: Reconstruction of dijets : A. first row - the distribution of E_t(jet)/E_t(parton); B. second row - the distribution of E_t jet/parton; C. third row - $\Delta\phi$ and $\Delta\eta$ distributions; D. fourth row - E_t reconstruction efficiency with E_t of jets.

ii) Events having two jets with energy one having E_t^{jet1} >10 GeV and the other with E_t^{jet2} >12 GeV (after jet E_t cut).

Fig. 4.36 (left: all events ; right : after event selection) shows that the jets originating from gluons mostly fail to fulfill the preceding criteria, suggesting that the gluon jet reconstruction efficiency is lower. The effect on extracted $\sqrt{\langle k_t^2 \rangle}$ with and without this event-selection criteria, shown in Fig. 4.37 (right), indicates that $\sqrt{\langle k_t^2 \rangle}$ is higher for the latter case. This arises as the combined effect of elimination of one of the jets lying outside the central rapidity region and the inclusion of more quark initiated jets due to the jet-cut.

It is to be mentioned that the RMS value form the distribution of $E_{t,jet1/jet2} sin(\phi_{jet1} - \phi_{jet2})$ and $E_{t,parton6/parton7} sin(\phi_{parton6} - \phi_{parton7})$ give $\sqrt{\langle k_t^2 \rangle}$ from the reconstructed jets and from the parton level respectively. We obtain a value of 3.0 GeV/c in the integrated p_t^{trig} range for both the cases which is shown in Fig. 4.37 with a dashed line parallel to the x-axis.

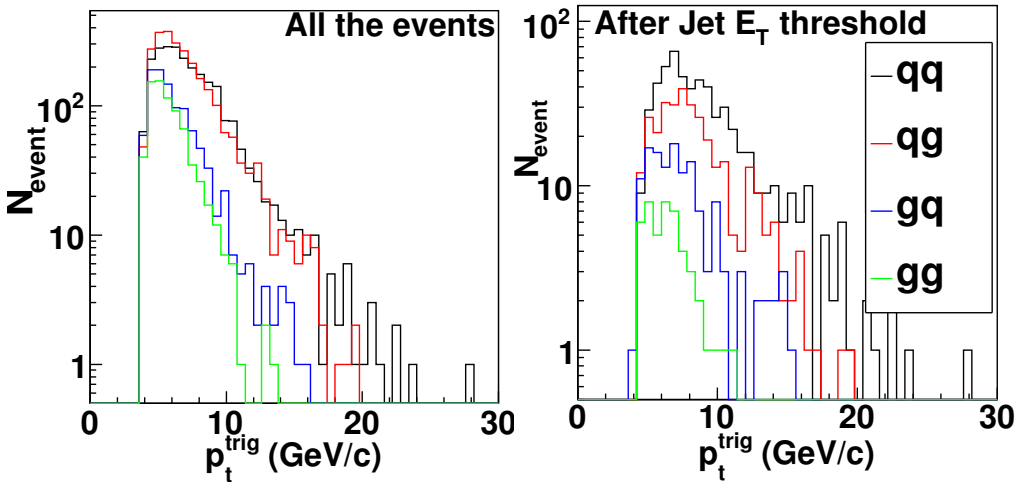

Figure 4.36: p_t^{trig} distributions before (left) and after (right) jet-E_t cut for different types of hard scattered processes, where the first parton in the labels(**q**q, **q**g, **g**q, **g**g) produces the trigger particle.

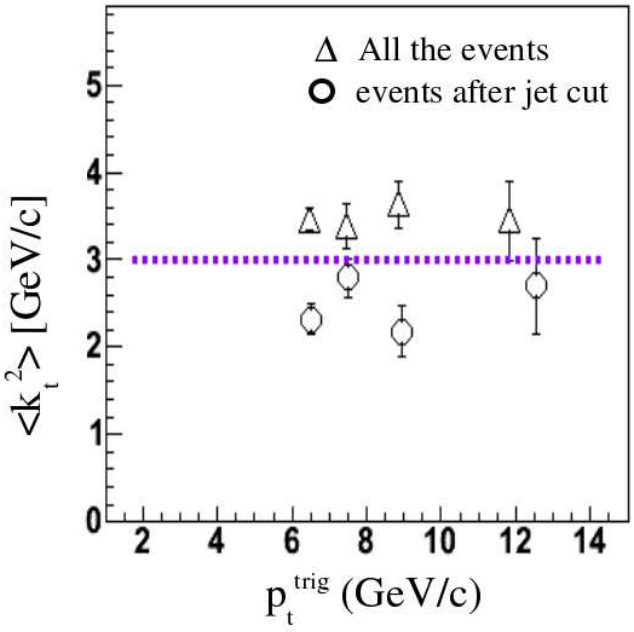

Figure 4.37: $\sqrt{k_t^2}$ of events before and after event selection (from PYTHIA). Values are consistently lower after event selection cut.

Di-hadron correlation analysis considers both the cases : (i) one jet in the acceptance, ii) 2→3 processes due to radiation in addition to 2→2 processes. The di-jet reconstruction method considers only 2→2 in the acceptance of the jet reconstruction result. In this sense for obtaining $\sqrt{\langle k_t^2 \rangle}$ for pp, using di-jet method is preferable since it considers both the jets in the acceptance. (ii) For dAu, if the nuclear effect give rises to 2→3 jets or twisting one of the di-jets out of the acceptance, di-jet method does not consider the cases while correlation can deals them better way.

Therefore from the simulation study we can infer that at least for the dAu collisions we can be sensitive to different levels of broadening using the di-hadron correlation method and the method of direct jet reconstruction.

4.6 Discussions on $\langle k_t^2 \rangle$ for pp and dAu

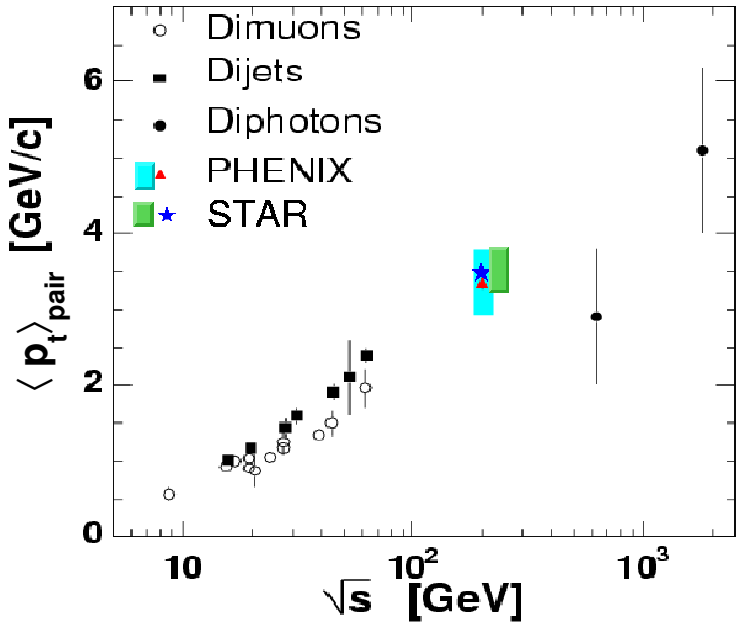

Figure 4.38: $\langle p_t \rangle_{pair}$ comparison from other experiments [84, 104] with our measurement (**STAR Preliminary**).

$\sqrt{\langle k_t^2 \rangle}$ has been obtained by the earlier measurements [84, 104] which are extracted from dimuons, diphotons and dijets measurements. We have the simple relation to correlate between $\sqrt{\langle k_t^2 \rangle}$, $\langle k_t \rangle$ and $\langle p_t \rangle_{pair}$ and the Fig. 4.38 shows a comparison for all the measurements.

$$\langle p_t \rangle_{pair} = \sqrt{2} \times \langle k_t \rangle = \sqrt{\pi/2} \times \langle k_t^2 \rangle \tag{4.8}$$

$\langle p_t \rangle_{pair} = 3.50 \pm 0.04(\text{stat}) \pm 0.34(\text{sys})$ GeV/c is consistent with earlier measurement from dijet, diphoton and dilepton [146]. It is to be mentioned that UA2 measurement [147, 148] of $\langle p_t \rangle_{pair}$ of Z^0 production at $\sqrt{s} \sim 600$ GeV gives 8.6 ± 1.5 GeV/c. The STAR data for pp at $\sqrt{s} = 500$ GeV in this respect is useful for measuring $\langle p_t \rangle_{pair}$ using dijet, Z^0 production or the present method of di-hadron correlations.

PHENIX [103] estimated the nuclear $\sqrt{\langle k_t^2 \rangle}$ for dAu at $\sqrt{s} = 200$ GeV which has been found to be very small. Our measurement estimate $\approx$ 10-20% enhacement in $\sqrt{\langle k_t^2 \rangle}$for dAu compared to pp collisions. But it should be mentioned mention that there is large systematic error due to the assumption that the fragmentation functions are same for pp and dAu.

Chapter 5

Fragmentation and direct photons : A correlation method of separation

5.1 Introduction

Direct photon generated in pp and AA collisions collisions is an important channel in determining the parton distribution function inside a nucleus. Since it gives a direct control to the parton kinematics, precise measurement of intrinsic transverse momentum of partons can be made. Direct photon yield can also be compared directly by the pQCD predictions. When one considers the detection of direct photons, the tasks at high energies e.g, at RHIC and LHC become quite difficult due to the presence of other sources of photons, acting as background to the direct photons.

Direct photons can be originated from two basic interactions e.g, $q\bar{q} \rightarrow g\gamma$ and $qg \rightarrow q\gamma$ [76]. Main sources of background photons are from hadronic decays and the fragmentation of partons. Some of the processes generating fragmentation photons e.g. qg $\rightarrow$ g(qγ) and qg $\rightarrow$ q(gγ) are even dominating in higher order. It has been shown that the yields of these photons are significant at relatively large $\sqrt{s}$. e.g, at $\sqrt{s}$ = 540 GeV [149, 150] and at RHIC and LHC energies [151, 152]. However, theoretically there are rather large uncertainties in the estimation of the yield of fragmentation photons [153], thereby making the measurement of fragmentation photons in pp collisions even more important. This will enable us to set a reference for AA collisions, where direct

photons can be used to calibrate the jets and thereby allowing more precise analysis of jet quenching. Recently at RHIC, efforts are being made to measure fragmentation photons [154].

For the measurement of direct photons, various methods (e.g. shower shape analysis method) are employed to identify and estimate the decay photons for their removal (e.g. for π^0, η). Apart from the decay photon removal, a method which being used extensively for identifying the direct photons is by the use of isolation cuts. Unlike direct photons, the fragmented photons carry charged particles as a part of the jet. The isolation cut is quite effective in rejecting the decay and fragmentation photons in most of the cases. But this cut is not very effective in rejecting fragmentation photons which share most of the parton's energy and appear like direct photons. It has been demonstrated extensively for the case of ALICE experiment [155] that all the methods mentioned earlier will enrich the photon sample. However no special effort is made for the rejection of fragmentation photons. It has been found that the fragmentation photons at LHC energies can be removed at best by 55 % by the method of isolation. Here we are presenting a technique for the discrimination of direct and fragmentation photons which is based on the measurement of the transverse energy of the away side jets relative to that of a detected photon on a transverse plane. For fragmentation photons, the ratio of the transverse energies of trigger photons and the awayside jet likely to differ from the ratio obtained for direct photons. In the present method this property is used for the enrichment of photon samples.

5.2 A method based on transverse energy balance of jets

Direct photons originate from two basic processes:

(i) annihilation of quarks $f\bar{f} \rightarrow g\gamma$ and by

(ii) Compton scattering $fg \rightarrow f\gamma$ (where f may be u, d, c, s, t, b and their anti-pairs).

On the other hand fragmentation photons are originated by the process of fragmentation of partons into colorless particles

(iii) $f_1 f \rightarrow (f_1\gamma_{frag})f$, where γ_{frag} is the fragmentation photon originating from the parton f_1.

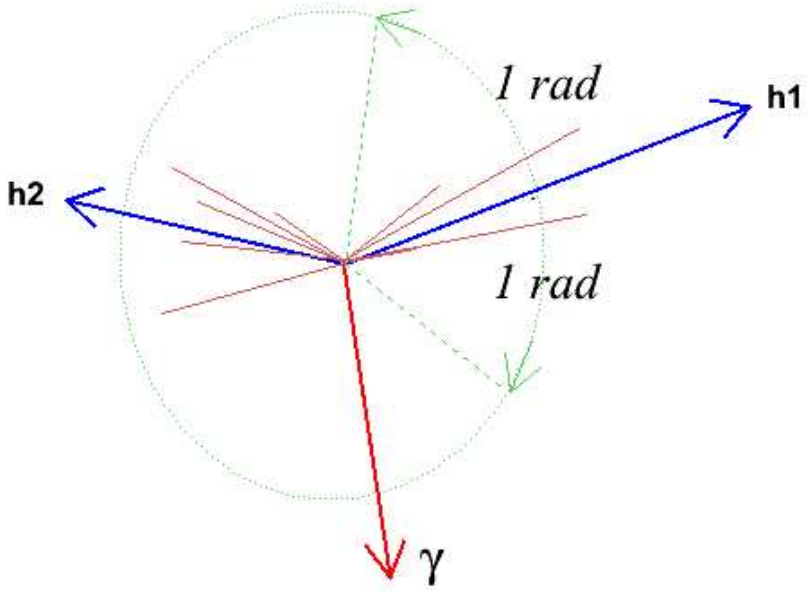

Figure 5.1: Event structure with fragmentation photons which escape isolation cut.

For the cases (i) and (ii), transverse energy of the direct photon is equal to that of the other parton(f/g), i.e, $E_{T,\gamma_{dir}} = E_{T,f/g}$. On the contrary, for the case (iii), the transverse energy of photon is always less than that of the parton f, i.e, $E_{T,\gamma_{frag}} < E_{T,f}$. From the experiments we do not get the partons but we measure the jets of particles fragmented from the parton. Hence in present method we have calculated E_T of the jet by summing over all charged particles around the leading hadron within a specific phase space in η and ϕ. After studying the jet topology on the transverse plane, we have found that the jet fragments, on away side may not have a unidirectional structure in a cone, it might even be visualized as two jets as shown in Fig. 5.1. It should be noted that, as the E_T is obtained from a limited phase space, calculated E_T does not represent the total jet energy, but a parameter based on the measured E_T, as discussed later has the property of discrimination of direct and fragmentation photons. In case of pp collisions, it is expected that the background underlying to the jet is not significant compared to those in case of heavy ion collisions.

For this work, we have used PYTHIA (6.214) as event generator. Current study is performed for the LHC energy (pp at $\sqrt{s}$ =14 TeV). We have generated direct and fragmentation photon samples in the p_T ranges 10 - 500 GeV/c. Two sources of photons are studied separately keeping relative contributions as given by the event generator. No further weights are applied for relative contributions of two sources of photons. We have taken a coverage of a photon detector as $|\eta| \leq 0.12$ and $220^0 \leq \phi \leq 340^0$, and the charge particle detector as $|\eta| \leq 1$ with full azimuthal coverage. This coverage is used for the detectors in ALICE for the detection of photons and charge particles respectively [156]. In the definition of the the away-side regions we have taken two leading hadrons h1, h2 (5.1) such that $|\phi_{h1} - \phi_{h2}| > 1$ rad. We have calculated the summed transverse energies as described below where we have considered the charged mesons only for finding E_{Ti}, the transverse energy of the particles lying in the segmented-ϕ region. This is the way to consider the jet transverse energy, where the existence of two well separated jets will account their energies in two separated ϕ sectors. We consider the larger of two E_T values to compare with the photon E_T.

$$E_{T1} = \sum_{i=\pi^{\pm},K^{\pm}(\phi_i>\phi_{h1}-1rad)}^{\phi_i<\phi_{h1}+1rad} E_{T_i} \tag{5.1}$$

$$E_{T2} = \sum_{i=\pi^{\pm},K^{\pm}(\phi>\phi_{h2}-1rad)}^{\phi<\phi_{h2}+1rad} E_{T_i} \tag{5.2}$$

The transverse energy $E_T >$ is the larger among those two (E_{T1} and E_{T2}) taken for the further analysis. We then extracted the discriminating parameter, 'f' = $E_{T,\gamma}/E_T$. It is expected that 'f' > 1 for direct γ and 'f' < 1 for fragmentation photons. Fig. 5.2 shows the distribution of 'f' for the direct photons and the fragmentation photons which demonstrate clearly the possibility of using this variable for discriminating two sources of photons. There are cases where 'f' might deviate from the expectation mentioned earlier due to the reasons that E_T might miss a significant fraction of the jet energy or the background from the underlying events might play a role. For the results presented here, we use a method called f-method where 'f' is used as the parameter for enrichment of the direct photon samples. It should be noted that by increasing the coverage of photon detectors, we can increase the statistics, but discriminating power will not change significantly.

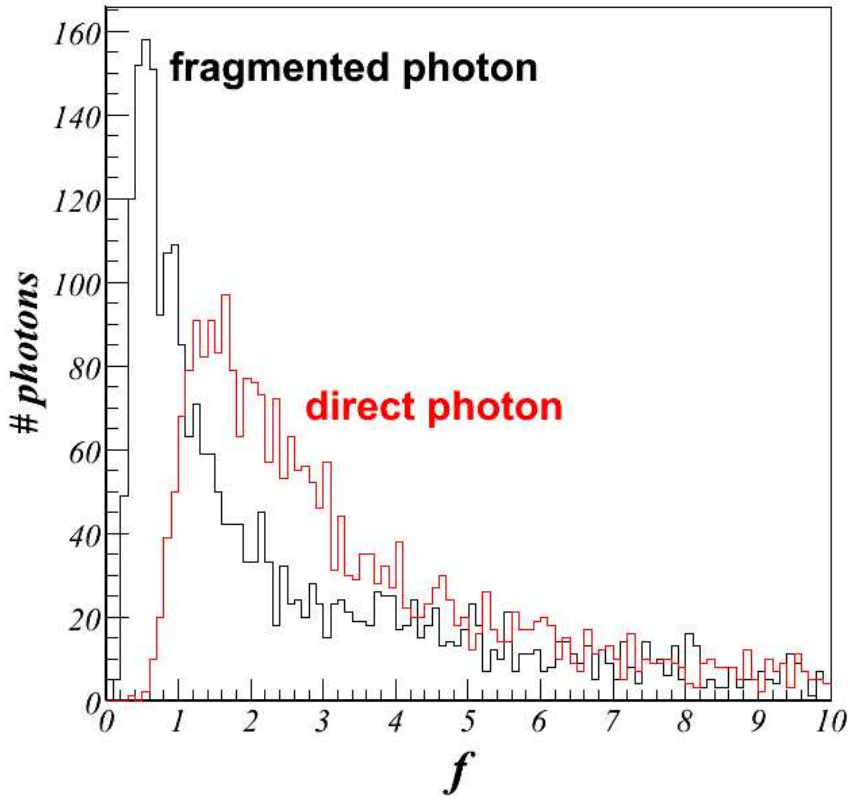

Figure 5.2: Distribution of 'f' for direct and fragmentation photons.

5.3 Simulation and results

we present the fractions of direct and fragmentation photons rejected after the application of isolation and 'f' cut, first separately and then sequentially. Simulated data consist of events having the direct photons by $\gamma-$ jet processes and the fragmentation photons from jet-jet processes in the detector coverage mentioned earlier. Other set of criteria e.g. shower shape, are not studied here as it depends strongly on the detector properties. It is expected that, these will enrich the photon samples even further. Events are filtered through varying isolation radii, R = $\sqrt{(\Delta\eta)^2 + (\Delta\phi)^2}$ with various thresholds on transverse momentum (p_T) on associated particles. Here $\Delta\eta$ and $\Delta\phi$ are the separation of associated charged particles from the triggered photon in η and ϕ directions respectively. The results from isolation cut alone are shown in Fig. 5.3 and

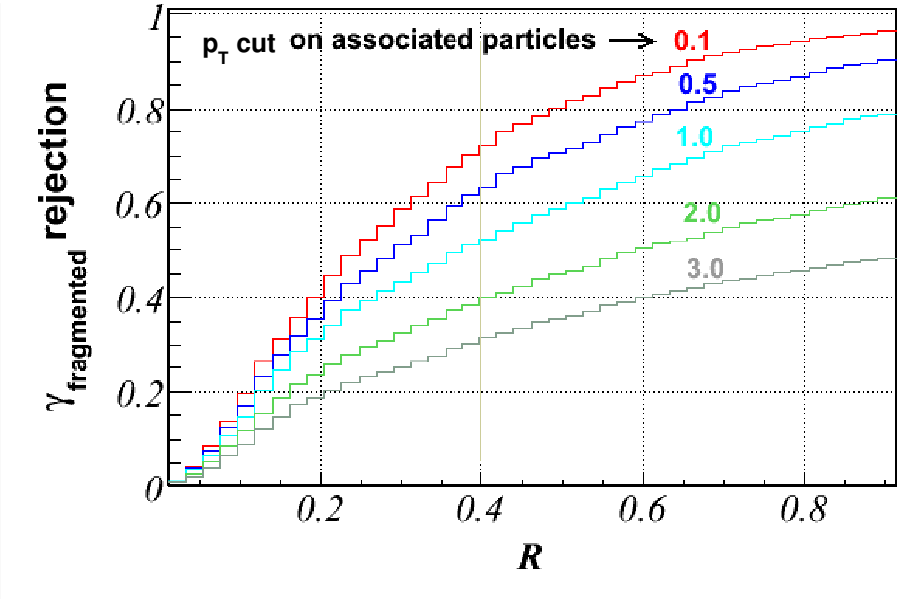

Figure 5.3: Fraction of fragmentation photons rejected after isolation cut. Various p_T cuts on associated particles are mentioned in the plot.

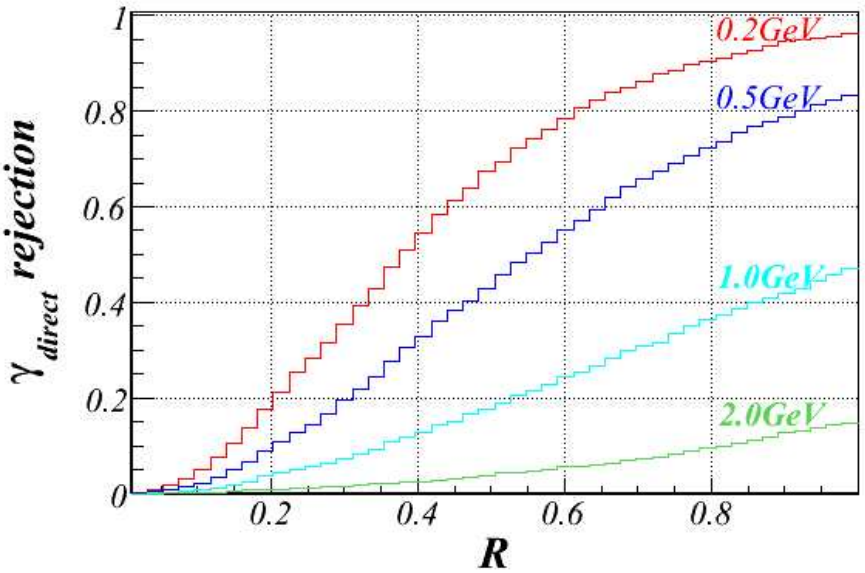

Figure 5.4: Fraction of direct photons rejected after isolation cut.

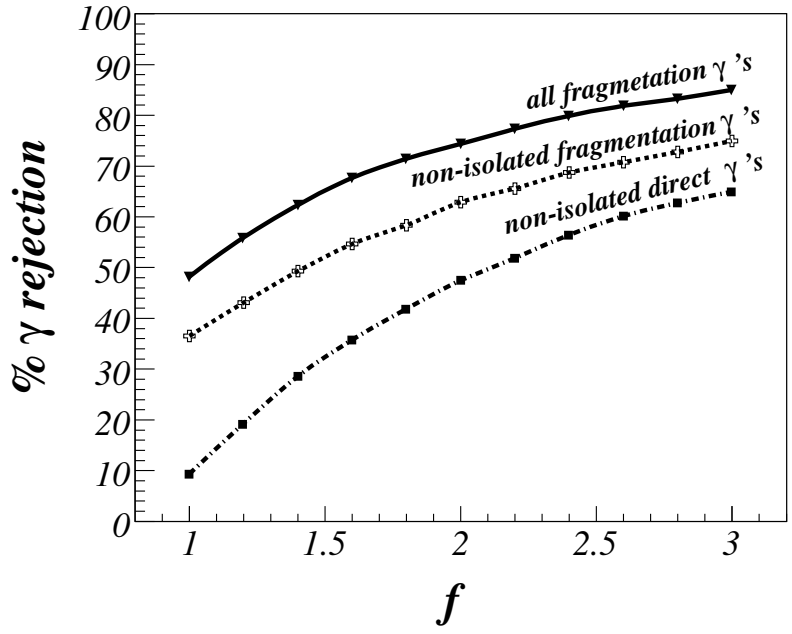

Figure 5.5: Fraction of non-isolated fragmentation (open cross markers) and direct (filled rectangular markers) photons rejected with $p_{T,associated} > 1$ GeV and for various 'f' values after isolation cut. Solid curve shows the rejection fraction for incident fragmentation photons restricted with the 'f-cut' alone. These results are obtained for Δ R = 0.4.

in Fig. 5.4. We have plotted the rejected fractions of fragmented and direct photons for different isolation radii and p_T thresholds. It is seen that for ΔR=0.4 and $p_{T,threshold}$ = 1 GeV, $\sim$55% of the fragmentation photons are rejected and $\sim$10% of the direct photons are lost due to the isolation criteria.

The results from the application of 'f' cut alone is shown in Fig. 5.5 by solid line. The dashed lines show the results of 'f'-cuts on both type of photons which survive the isolation cuts. The percentage of rejection with the variation of 'f' for two types values are as follows :

- The solid curve shows that only 'f' cut alone can reject fragmentation photons in the range of 50-80%.
- The curve with filled points shows the s rejection fraction for non-isolated direct photons which varies from 10-60%.

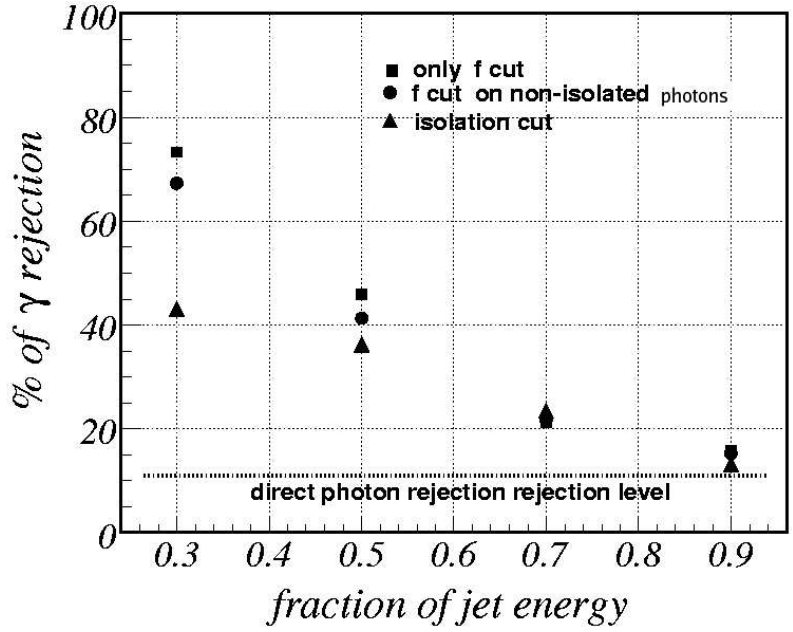

Figure 5.6: Rejection efficiency of the fragmentation photons as a function of the fraction of the jet energy carried by the fragmentation photon.

- The curve with open-cross shows the rejection efficiency of the fragmentation photons which can not be removed by isolation cuts. We have applied 'f' cuts for R=0.4 and $p_{T,associated} > 1$ GeV. As shown in the dashed curve upto 70% of non-isolated fragmentation photon can be rejected by this cut, however at this value fraction of direct photon sample rejected is relatively high.

The rejection of direct photons is always less compared to that of the the fragmentation photons. Above some 'f' value, two cases become parallel, suggesting a little increase in purity of direct photon, while not rejecting direct photons appreciably. For f = 1, ∼35% of the non-isolated fragmentation photons can be removed in the new approach at the cost of 10% loss of the direct photons.

The performance of 'f'-cut is dependent on the fraction of jet energy carried by the fragmentation photon. A study has been made at $\sqrt{s} = 200$ GeV with p_T of fragmentation photons above 4 GeV and jet $p_T \geq 10$ GeV. In Fig. 5.6 we show the variation of the rejection efficiency by the isolation and the f-cut method with varying fractions of jet energy carried by the fragmentation

photon. It is clear from Fig. 5.6 that for the fragmentation photons carrying a larger fraction of jet energy, identification efficiency decreases and performance by all methods become similar.

5.4 Summary and Discussions

Based on the differences in jet topology for direct and fragmentation photons, we have developed a method to enrich the direct photon sample in addition to the results obtained by the isolation cut method. The prescribed method is based on the transverse energy balance of near and away side jets for two sources of photons. For a case when all sources of the background photons other than the fragmentation photons are eliminated, fraction of the fragmentation photons remaining in the sample plays an important role. At LHC energy, for pp collisions, if we take the ratio as 1 in the interesting p_T region we can obtain $\sim 50\%$ fragmentation photons rejected due to the isolation cut and 40% non-isolated fragmented photon rejected by 'f' cut at the cost of 10% direct photon loss. We can estimate that the overall purity of direct photon therefore increases from 66% to 75%.

Chapter 6

Limting fragmentation and baryon stoppings in AA collisions

6.1 Introduction

At the relativistic heavy ion collisions, charged baryons and antibaryons can be produced directly or as the remnants of the colliding nuclei. With the increase in colliding energy, midrapidity region is expected to contain reduced amount of net-baryon, thereby approaching a baryon-free region. It has been found from the study of p/$\bar{p}$ and net-proton(p-$\bar{p}$) at different colliding energies ($\sqrt{s}$) that the system at midrapidity is approaching towards baryon-free at RHIC energy [157]. These studies are performed at midrapidities, but the situation is expected to be different at forward rapidities, where detected charged baryons contain beam-remnants along with the produced baryons. The fraction of beam-baryons are expected to be reduced towards more central collisions. Estimation of the relative change in the rapidity distribution of the net-charged baryons and their centrality dependence will provide the information about the chemistry of the colliding system, specially the baryon content. The distributions of net baryon at forward rapidities are important variables from the points of view of the presence of beam baryons. In normal procedure of measurement of charged baryons, different particle identification methods are used for the detection of protons or antiprotons. In the work presented here, we obtain the pseudorapidity distributions of charged baryons by a method based

on the subtractions of pseudorapidity distributions of the identified mesons from that of produced charged particles. From the extracted pseudorapidity distributions of charged baryons and their centrality dependence, we make an estimate of rapidity loss of baryons in the collisions.

6.2 Pseudorapidity distributions from rapidity distributions

Pseudorapidity distributions of the produced charged particles have been studied by all the collaborations at RHIC. The measured pseudorapidity densities at midrapidity by different collaborations are close within 6%. PHOBOS [158] and BRHAMS [159] collaborations have measured pseudorapidity distributions in an extended region of pseudorapidity for various centralities. STAR has measured pseudorapidity distributions of photons at forward rapidities at various energies. Detailed investigations of measured pseudorapidity distributions reveal that, these distributions when plotted with to $\eta^{'} = \eta$ - η_{beam}, show at scaling a forward rapidities, which is independent of the colliding energy [160]. $\eta^{'}$ distributions at various energies show that the pseudorapidity distributions shows a limiting behavior towards forward rapidity, and they fall on a single line. Depending on the collision energy, it starts deviating towards midrapidity at different η. This phenomena is known as limiting fragmentation [161], where the limiting fragmentation lines at various energies can be characterized by two parameters, $\Delta\ \eta^{'}$, giving the extent of $\eta^{'}$ over which the distributions continue to fall on a common line and $\rho^{'}$ is the limit of $(\mathrm{dN/d}\eta)/(2N_{part})$, at which it deviates from the common line. Centrality dependence of the limiting fragmentation has been a topic of interest where it was found that while for charged particles it is centrality dependent, but for identified mesons(π^+, π^-, π^0) it is centrality independent [162].

Making use of the observation of centrality-independent limiting fragmentation of the mesons, we developed a method which extracts the pseudorapidity ($\eta^{'}$) distributions of charged baryons.

We have taken the rapidity distributions of (π^+, π^-, K^+ and K^-) measured by BRAHMS and converted them into pseudorapidity distributions (Fig. 6.1) using the Jacobian

$$\frac{dy}{d\eta} = \frac{(\frac{p_L}{m})cosh\eta}{\sqrt{(\frac{p_L}{m})^2 cosh^2\eta + 1}} \tag{6.1}$$

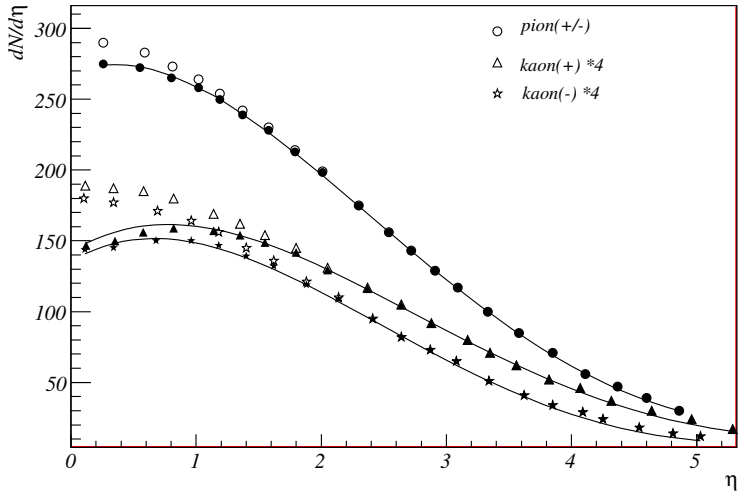

Figure 6.1: Jacobian transformation of the rapidity distributions of the identified particles.Open markers are before transformation and filled ones are after transformation.

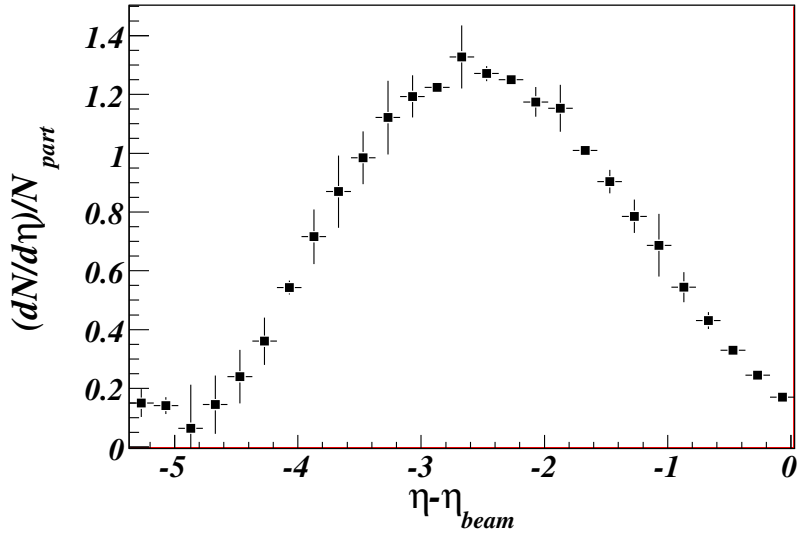

Figure 6.2: Normalized pseudorapidity distributions of baryons for central 200GeV Au-Au collisions.

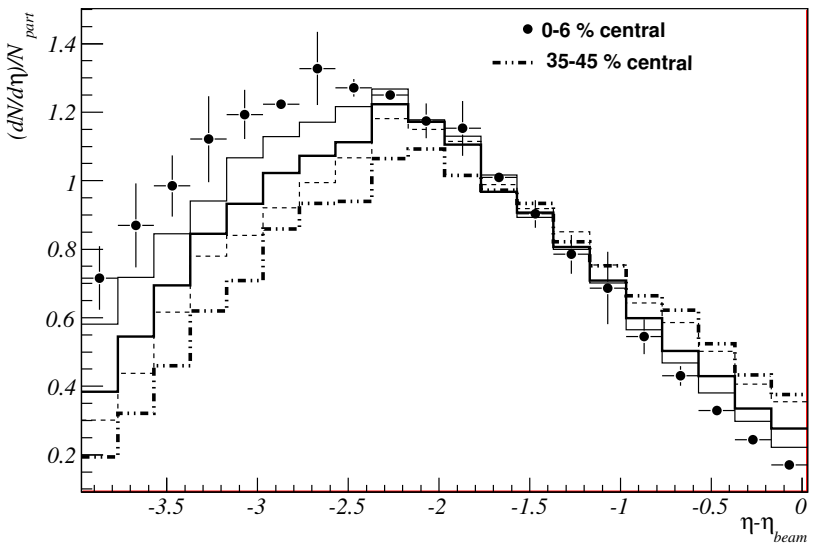

Figure 6.3: Centrality dependence of the pseudorapidity distributions of baryons at 200 GeV AuAu collisions. For $\eta \approx$-1 a crossover occurs.

, when $\langle p_T \rangle$ is taken as 0.4 MeV for pions and 0.6 MeV for kaons and p_L indicate the momentum of the particles along the direction of beam axis. Extracted pseudorapidity distributions for all mesons taken together represent the pseudorapidity distributions of charged mesons. This distribution was then converted into the $\eta^{'} = \eta$ - η_{beam} frame.

We then obtain the pseudorapidity distributions of charged particles at $\sqrt{s}$=200GeV for different centralities and converted them into $\eta^{'} = \eta$ - η_{beam} frame. $\eta^{'}$-distributions of produced mesons obtained earlier from BRAHMS data were then subtracted from the $\eta^{'}$-distributions of charged particles at various centralities. The subtracted distributions provide with the $\eta^{'}$-distribution of charged baryons.

6.3 Results and Discussions

Fig. 6.2 and 6.3 show the $\eta^{'}$-distributions of baryons for central events and at various centralities respectively. Errors represent the propagated errors from two published distributions.

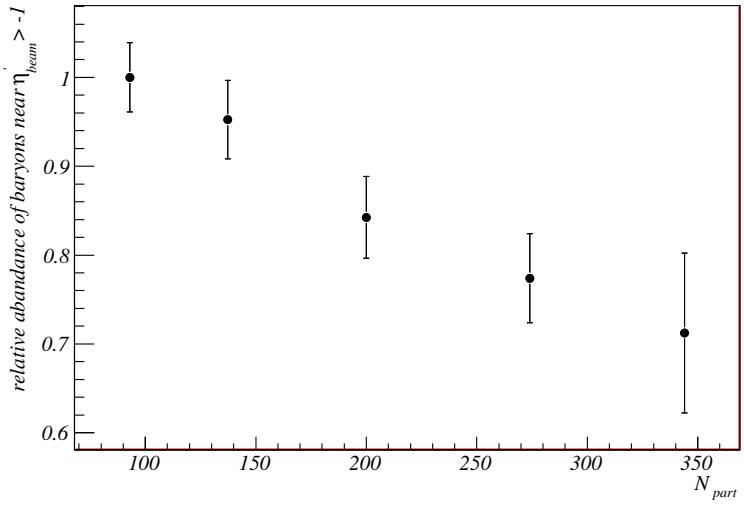

Figure 6.4: Relative decrease in the number of baryons above $\eta^{'}>$ -1 with respect to the peripheral collisions while going towards central collisions.

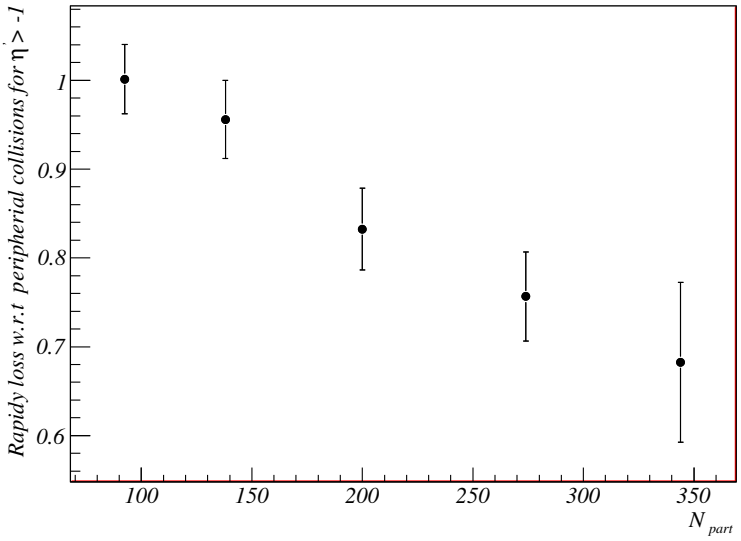

Figure 6.5: Relative loss in rapidity above $\eta^{'}>$ -1 with respect to peripheral collisions while going towards central collisions.

Even though the error is large, but from the extracted distributions, we can make several conclusions,

1. The charged baryon $\eta^{'}$-distributions follow approximate limiting fragmentation with deviations in slopes
2. the distributions at the central collisions appear to be shifted compared to the peripheral collisions
3. at $\eta^{'} \approx$ -1, peripheral distributions cross the central distributions.

As the distributions in Fig. 6.3 represent produced and beam baryons together, the produced baryons for peripheral collisions are expected to be smaller or similar to these at those at the central collisions. However the distributions at $\eta^{'} >$ -1 are expected to be mainly from beam-protons.

We therefore make an estimate of the relative fraction of beam-protons and thereby the relative loss of beam rapidities with respect to the central collisions. Fig. 6.4 shows the relative fraction of beam-protons. It shows a relative decrease in number of baryons above $\eta^{'} >$ -1 with respect to peripheral collisions while going towards central collisions. Rapidity loss is calculated from the net baryon distribution in $\eta^{'} > 1$, where the protons at $\eta^{'} >= 1$ is considered to retain the whole beam rapidity. Therefore the rapidity loss is given by normalized value of *bin content at* $|\eta^{'}| \times$ the $\eta^{'}$ value for the corresponding bin.

Fig. 6.5 shows the relative loss of rapidity at various centralities for baryons with $\eta^{'} >$ -1.0 . As shown in Fig. 6.5 the rapidity loss reduces almost linearly with centrality. This means that if for peripheral case we consider the rapidity retrained is 1.0, in the most central collisions, the beam rapidity retained is $\sim$0.7 (for $N_{part} = 350$; Fig. 6.5). This indicates that with the centrality range studied there, there is a 30% relative change in the rapidity loss.

Chapter 7

Summary and Conclusions

The work presented in this thesis is based on the detector design and fabrication, data taking and data analysis in high energy heavy in collision experiments. The major aim of this type of experiments is to study the expected creation of a deconfined state of matter called Quark Gluon Plasma (QGP). Such a state is believed to be existing a micro-sec after the creation of the Big Bang. Experiments through reletivistic heavy ion collisions is conducted to create such a state in a small scale. It is however essential that we understand the smaller systems like pp and dAu collisions before embarking on understanding the complex nuclear collisions. RHIC at BNL and LHC at CERN are the accelerator centers engaged in such a research topic.

The experimental setups are built at such accelerator centres over several years of planning, R & D and production. Specialized detector systems are employed for detecting or identifying different particle species.

PMD testing and simulations :

In this work, we have discussed the design, fabrication and testing of a major detector system built to detect photons at forward rapidities. The photon Multiplicity Detector (PMD) for the ALICE experiment at LHC is designed and built by an Indian Collaboration. A preshower detector consisting of about 2,00,000 cells each of 0.2 cm^2 area has been fabricated and installed at CERN. We have discussed in details the principle of the detector, its parameters, arrangement of cooling, and results from the testing with pion and electron beams. It is shown that the detector can operate at 1300V in proportional region with 95% efficiency of pion detection. There is $\sim$0.83% cells on preshower side which are found to be saturated with 5 GeV pion beam at 1375

V. Cell to cell gain variation is within 15% in a modue. Electron beam results provide the polynomial (degree 2) form of a calibration relation at 1400 volt with a constant term of a_0 =-1.31 and slope of a_1 = 148. A quarter model has been described for making the cooling arrangement in the detector. We have also described the results of the performance from the PMD simulation for pp collisions at $\sqrt{s}$ = 14 TeV. It has been found that an optimization is needed for obtaining best possible purity and efficiency of photon detection in pp collisions at LHC.

The major part of the work deals with the STAR data towards obtaining the correlation function of high p_T particles in pp and dAu collisions. The method of correlation is a very powerful tool which can be used to obtain and study in details the jet structures in pp and dAu collisions. In addition, we have discussed two short specialized topics in high energy collisions. One is related to the identification of a special type of jet events which are known as γ-jets and we have used PYTHIA simulation and tested the algorithm for pp collisions at $\sqrt{s}$ = 200 GeV and 14 TeV. The other topic studies the centrality dependence of the limiting fragmentation behavior of net baryons at forward rapidity which relates the baryon stopping scenario at different centralities.

Jet properties in pp and dAu collisions at $\sqrt{s}$ = 200 GeV :

The structure of the hard scattering processes due to parton parton interaction in pp from the dihadron correlations is presented in this thesis. The possible effect on the jet parameters in the cold nuclear matter of dAu collisions is also presented and a comparison is made between the pp and dAu datasets at various centralities. The correlation analysis involves a trigger particle in each event which is selected as charged tracks (for ch-ch correlation) in minimum bias datasets and π^0 (for π^0-ch correlation) in high tower datasets. STAR data from the Time Projection Chamber (TPC) and the Barrel Electromagnetic Calorimeter (BEMC) are used for this analysis. BEMC triggered datasets provide a higher p_T-trigger reach for high p_T analysis.

π^0 reconstruction from the BEMC tower involves maximum clusters a maximum of four adjacent towers and the E_T of π^0s are taken within the range of 6.5 GeV to 18.5 GeV. The jets appear as clear near and away-side peaks in the correlation functions. The yields and $\sqrt{\langle j_T^2 \rangle}$ obtained from the near side width of the correlation function are similar in magnitude for pp and dAu. $\sqrt{j_T^2}$ comes out to be 598 $\pm$ 28 (pp) and 565 $\pm$ 44 (dAu) for ch-ch correlations and 576 $\pm$ 11 (pp) and 513 $\pm$ 46 (dAu) π^0-ch correlations. The away-side width of the correlation functions differ slightly compared to pp which ap-

pears as 10-20% enhancement of $\sqrt{k_T^2}$ due to nuclear modification assuming the fragmentation function for pp and dAu being the same.

The correlation method gives the value of $\sqrt{\langle {k^s}_T^2 \rangle}$ in the form of $\frac{\langle z_t(k_T,x_h)\rangle\sqrt{\langle k_T^2\rangle}}{\hat{x}_h(k_T,x_h)}$ where the fragmentation variables, $\langle z_t(k_T,x_h)\rangle$ and $\hat{x}_h(k_T,x_h)$, are disentangled using PYTHIA simulations. $\sqrt{k_T^2}$ is found to be 2.80±0.04(stat)±0.27(sys) GeV/c for pp collisions and 3.4±0.03(stat)±0.31(sys) GeV/c for dAu using the same fragmentation parameters for pp and dAu. For dAu there might be a modification factor of the fragmentation function in cold nuclear medium and therefore $\sqrt{\langle k_T^2\rangle}$ =3.4 GeV/c obtained might have a large systematics.

In the centrality bins determined from the multiplicity of FTPC (east), dAu minimum bias datasets have been used to find the centrality dependence of jet parameters. There is no major modification of the jet properties observed at different centralities.

There are two special features in k_T which can be summarized as the intrinsic and the broadening effect. The later is dependent on the jet energy scale. In this perspective, the modification of the parton distribution function and the jet-p_T reach is important in studying the the k_T broadening. Therefore using di-hadron correlation, the STAR data for pp at $\sqrt{s}$ = 400 GeV and $\sqrt{s}$ = 500 GeV can be used to find the the acoplanarity at higher center of mass energies where we can probe both at low x and simultaneously at different jet energy scale.

Discrimination of direct and fragmentation photons :

A special type of hard scattering is γ-jet which is used as a clean calibrated probe for studying the jet modification in the matter formed in the heavy ion collisions. Detection of direct photons is very challenging due to the presence of a large background from the decay photons from π^0 and η mesons. The fragmentation photons which behave like single photons also contribute significantly to the background of direct photons. Based on the transverse momentum imbalance of di-jets, we discussed a method of isolating the direct photons from the fragmentation photon contribution. The method shows that ∼35-40% of the non-isolated fragmentation photons can be removed by this new method. The method has the potential to be useful in the analysis like probing the gluon distribution using γ-jet in pp collisions and determining the helicity preference for gluons [ΔG(x_g)] inside a polarized proton as a function of gluon spin content.

In summary, in this thesis we have discussed the experimental studies of high energy pp and dAu collisions for production of jets, which can be used as reference for AA collisions. In addition to this topic of anlysis we have discussed the fabrication and testing of a Photon Multiplicity Detector (PMD) in ALICE and simulated the enhancement in the detection of direct photons in high energy experimental experimental studies.

Bibliography

[1] E. V. Shuryak, I. Zahed, Towards a theory of binary bound states in the quark gluon plasma.

[2] T. D. Lee, Is the physical vacuum a medium CU-TP-170, Published in Trans.N.Y.Acad.Sci.Ser.2 **v.40** 1980:0111

[3] T. D. Lee, Abnormal nuclear states ans vaccum excitations, Rev. Mod. Phys,**47** 47(1975).

[4] A. Chodos, R.L. Jaffe, K. Johson, C.B. Thorn and F.V. Weisskopf, Phys. Rev. **D9**, 3471(1979).

[5] B. Anderson, G.Gustafson, G. Ingelman and T. Sjöstrand, Phys. Rep. **97** 33(1983).

[6] B. Anderson, G.Gustafson, and B. Söderberg, Nucl. Phys. **264** 29(1986).

[7] L.V. Gribov, E.M. Levin, and M.G. Ryskin, Phys. Rep. **100**, 1(1983)

[8] E.M. Levin and M.G. Ryskin, Phys. Rep. **189**, 267(1990)

[9] M. Creutz, Gauge fixing, the transfer matrix, and confinement on a lattice, Phys. Rev. **D15** 1128(1977).

[10] K. G. Wilson, Confinement of quarks, Phys. Rev. **D10** 2445(1974).

[11] E. Laermann, O. Philipsen, Status of lattice qcd at finite temperature hep-lat/0303042.

[12] F. Karsch, Lattice qcd at high temperature and density, Lect. Notes Phys. **583** (2002) 209–249.

[13] K. Rajagopal, The phases of qcd in heavy ion collisions and compact stars, Acta Phys. Polon. **B31** 3021(2000).

[14] G. Baym, Rhic: From dreams to beams in two decades, Nucl. Phys. **A698** XXIII–XXXII(2002).

[15] J. D. Bjorken, Highly relativistic nucleus-nucleus collisions: The central rapidity region, Phys. Rev. **D 27** 140(1983).

[16] M. Gyulassy and T. Matsui. Phys. Rev. **D 29** 419(1984).

[17] K.Kajantie, R. Raitio and P.V. Ruuskanen. Nucl. Phys. **B222**, 152(1983).

[18] G. Baym, B.L. Fryman, J.P. Blaizot, M. Soyeur and W. Czyz. Nucl. Phys. **A407**, 541(1983).

[19] H. Gersdorff, L.D. McLerran, M. Kataja and P.V. Ruuskanen. Phys. Rev. **D 34**, 794(1986).

[20] N.S. Amelin, E.F. Straubo, L.P. Csernai, V.D. Toneev, K.K. Gudima and D.D. Strottman. Phys. Rev. Lett. **67** 1523(1991).

[21] P.V Ruuskanen, Nucl. Phys. **A522**, 255c(1991).

[22] P.V Ruuskanen, Nucl. Phys. **A544**, 169c(1991).

[23] C.Y. Wong, Phys. Rev. **C48**, 902(1993).

[24] J. Kasputa, P. Lichard and D. Siebert, Nucl. Phys.**A544**, 485c(1992).

[25] B. Sinha, Phys. Lett. **B128**, 91(1983) and J. Alam, D.K. Shrivastavs, B. Sinha and D.N. Basu, Phys. Rev. **D48**, 1117(1993).

[26] R.C Hwa and K. Kajantie, Phys. Rev. **D32**, 1109(1985).

[27] J. Kasputa, P. Lichard and D. Siebert, Phys. Rev. **D44**, 2774(1991).

[28] C.T. Altherr, P.V. Rauskanen, Nucl. Phys. **B380**, 377(1992).

[29] J.D. Bjorken and L. McLerran. Phys. Rev. **D31**, 63(1985).

[30] L. Xiong and C.M. Ko, Phys. Rev. **C37**, 880(1988).

[31] T. Matsui and H. Satz, Phys. Lett. **B178** 416(1986);

[32] P. Braun-Munzinger, K. Redlich and J. Stachel, in Quark Gluon Plasma 3, eds. R.C. Hwa and X.N. Wang (World Scientific, Singapore, 2003), nucl-th/0304013.

[33] K. Huang, Statistical Mechanics (John Wiley and Sons, 1988).

[34] R. Hagedorn, Nuovo Cim. Suppl. **3**, 147(1965).

[35] E. Fermi, Prog. Theor. Phys. **5**, 570(1950).

[36] E.V. Shuryak, Phys. Lett. **B 42**, 357(1972); J. Rafelski and M. Danos, Phys. Lett. **B97**, (1980) 279; R.Hagedorn and K. Redlich Z. Phys. **C 27**, (1985) 541.

[37] S. Nagamiya, Nucl. Phys. **A544**, 5c(1992).

[38] C.M. Ko and L.H. Xia Nucl. Phys **A498**, 561c(1989).

[39] J. Stachel and G.R. Yong, Ann. Rev. Nucl. Part. Sci. **42**, 537(1992).

[40] Y. Pang, T.J. Schlagel, and S.H. Khanna, Phys. Rev. Lett. **18**, 2743(1992).

[41] J. Rafelski, Phys. Rep. **88**, 331(1882).

[42] P. F. Kolb, J. Sollfrank, U. W. Heinz, Phys. Rev. **C62**, 054909(2000).

[43] S. S. Adler, *et al.*, Phys. Rev. Lett. **91**, 182301(2003).

[44] S. S. Adler, *et al.*, Phys. Rev. Lett. **87**, 182301(2001).

[45] P. Huovinen, P. F. Kolb, U. W. Heinz, P. V. Ruuskanen, S. A. Voloshin, Radial and elliptic flow at rhic: Further predictions, Phys. Lett. **B503**, 58(2001).

[46] D. Teaney, J. Lauret, E. V. Shuryak, A hydrodynamic description of heavy ion collisions at the sps and rhic.

[47] D. H. Rischke, M. Gyulassy, The maximum lifetime of the quark-gluon plasma, Nucl. Phys. **A597**, 701(1996).

[48] G. F. Bertsch, Pion interferometry as a probe of the plasma, Nucl. Phys.**A498**, 173c(1989).

[49] S. Pratt, Pion interferometry of quark - gluon plasma, Phys. Rev. **D33**, 1314(1986).

[50] A. Breakstone *et al.*, Phys. Lett. **162B**, 400(1985).

[51] A. Breakstone *et al.*, Zeit. Phys. **c33**, 333(1987).

[52] P. Seyboth *et al.*, Nucl. Phys. **A544**, 293c(1992).

[53] S. Prat, Phys. Rev. **D33**, 72(1986); S. Prat, Phys. Rev. **D33**, 1314(1986).

[54] G.F. Bertsch, Nucl. Phys. **A498**, 173c(1989).

[55] Y. Hama and S.S. Padula, Phys. Rev. **D37**, 3237(1988).

[56] S. Pratt, Pion interferometry for exploding sources, Phys. Rev. Lett. **53** 1219(1984).

[57] J. Adams, *et al.*, Phys. Rev. Lett. **93**, 012301(2004).

[58] S. S. Adler, *et al.*, Phys. Rev. Lett. **93**, 152302(2004).

[59] M. Gyulassy, I. Vitev, X.N. Wang and B.W. hang nucl-th/0302077.

[60] M.H. Thoma and M. Gyulassy, Nucl. Phys. **B351**, 491(1991); M.H. Thoma, Phys. Rev. **D49**, 451 (1994).

[61] M. Gyulassy, P. Levai and I. Vitev, Phys. Rev. Lett **85**, 5535(2000).

[62] M. Gyulassy, P. Levai and I. Vitev, Nucl. Phys. **B 571**, 197(2000).

[63] M. Gyulassy, P. Levai and I. Vitev, Nucl. Phys. **B 594**, 371(2001).

[64] J. Adams *et al.* [STAR Collaboration], Phys. Rev. Lett. **91**, 072304(2003).

[65] I. Arsene *et al.* [BRAHMS Collaboration], Phys. Rev. Lett. **91**, 072305(2003).

[66] S.S. Adler *et al.* [PHENIX Collaboration], Phys. Rev. Lett. **91**, 072303(2003).

[67] B.B. Back *et al.* [PHOBOS Collaboration], Phys. Rev. Lett. **91** (2003) 072302.

[68] D. Antreasyan *et al.*, Phys. Rev. **D19**, 764(1979).

[69] X.N. Wang, Phys. Rept. **280**, 287(1997); M. Lev and B. Petersson, Z. Phys. **C21**, 155(1987); T. Ochiai *et al.*, Prog. Theor. Phys. **75**, 288(1986).

[70] C. Adler *et al.* [STAR Collaboration], Phys. Rev. Lett. **90**, 082302(2003).

[71] J. Adams *et al.* [STAR Collaboration], Phys. Rev. Lett. **93** 252301(2004).

[72] D. Kharzeev, E. Levin and L. McLerran, Phys. Lett.**B561**, 93(2003).

[73] B. I. Abelev *et al.*, Phys. Lett. **B655**, 104(2007).

[74] R.D. Field (CDF) The underlying event in hard scattering processes, eConf-C010630, P5012001; hep-ph/0201192.

[75] T. Affolder *et al.* Phys. Rev., **D64** 032001(2001).

[76] J. F. Owens, Rev. Mod. Phys. **59**, 465(1987).

[77] N. Werner *et al.*, hep-ex/0305109.

[78] A.D. Martin, R.G. Roberts, W.J. Stirling, and R.S. Thorne, Eur. Phys. J., **C23** 73(2002).

[79] J. Pumplin *et al.* (CTEQ). New generation of parton distributions with uncertainties from global QCD analysis, JHEP, **07**, 0(2002).

[80] D. Buskulic *et al.* Measurement form scaling violations in fragmentation functions in e+ e- annihilation. Phys. Lett. **B357** 499(1995).

[81] M. Della Negra *et al.*, Nucl. Phys.**B127**, 1(1977).

[82] R.P. Feynman, R.D. Field and G.C. Fox, Nucl. Phys.**B128**, 1(1977).

[83] A. Kulesza, G. Sterman, and W. Vogelsang, Nucl. Phys.**A721**, 591(2003).

[84] L. Apanasevich *et al.* Phys. Rev.**D59**, 074007(1999)

[85] J.F. Owens and J.D. Kimal, Phys.Rev.**D18**, 3313(1978).

[86] J.F. Owens and E. Reya and M. Gluck, Phys.Rev.**D18**, 1501(1978).

[87] A.L.S. Angelis *et al.*, Phys. Lett.**B97**, 163(1980).

[88] P. Darriulat, Ann. Rev. Nucl. Part. Sci.**30**, 159(1980).

[89] K. Adachi *et al.*, (TOPAZ), Phys. Lett. **B451**, 256(1999).

[90] D. Naples *et al.*, Phys. Rev. Lett. **72**, 2341(1994).

[91] C. Stewart *et al.* (E557), Phys. Rev.**D42**, 1385(1990).

[92] M. D. Corcoran *et al.* (E609), Phys Lett. **B259**, 209(1994).

[93] J.W. Cronin *et al.*, Phys. Rev. **D11**, 3105(1975).

[94] S.S. Adler*et al.*, Phys. Rev. Lett. **91**, 072303(2003).

[95] J. Adams*et al.*, Phys. Rev. Lett. **91**, 072304(2003).

[96] B.B. Back*et al.*, Phys. Rev. Lett. **91**, 072302(2003).

[97] M.R. Adams *et al.*, Rev. Lett. **72**, 466(1994).

[98] A. Accardi, hep-ph/0212148(2002).

[99] X. N.Wang, Phys. Rev. **C61**, 064910(2000).

[100] J.-W. Qiu and I. Vitev, Phys. Lett. **B587**, 52(2004); hep-ph/0405068 (2004).

[101] G. G. Barnafoldi, G. Papp, P. Levai, and G. Fai, J. Phys.**G30**,S1125(2004).

[102] R. C. Hwa and C. B Yang, Phys. Rev. Lett.**93**, 082302(2004).

[103] S.S. Adler*et al.*, Phys. Rev.**C73**, 054903(2006).

[104] S.S. Adler*et al.*, Phys. Rev. **D74**, 072002(2006)

[105] STAR Collaboration, K. H. Ackermann *et al*, Nucl. Instrum. Methods Phys. Res., Sect. **A 499**, 624 (2003).

[106] R. Bellwied *et al.*, Nucl. Intrum. Meth. **A 499**, 640(2003).

[107] L. Arnold *et al.*, Nucl. Intrum. Meth. **A 499**, 652(2003).

[108] Ming Shao *et al.*, Nucl. Instrum. Meth. **A 558**, 419(2006).

[109] F. Bergsma *et al.*, Nucl. Instrum. Meth. **A 499**, 633(2003).

[110] K.H. Ackermann *et al.*, Nucl. Instrum. Meth. **A 499**, 713(2003).

[111] M. M. Aggarwal *et al.*, Nucl. Instrum. Meth. **A 499**, 751(2003).

[112] F. Sauli. Principles of operation of multiwire proportional and drift chambers. Technical Report CERN 77-09, CERN, 1977.

[113] F. S. Bieser *et al.*, Nucl. Instrum. Meth. **A 499**, 766(2003).

[114] C. Adler *et al.*, Nucl. Instrum. Meth. **A 499**, 778(2003).

[115] M.M. Aggarwal, *et al.*, Nucl. Instr. and Meth. **A 372**, 143(1996).

[116] M.M. Aggarwal, *et al.*, Nucl. Instr. and Meth. **A 424**, 395(1999).

[117] D.P. Mahapatra, *et al.*, STAR Note SN-310, 1997;

[118] ALICE: Physics Performance Report, Volume I, J. Phys. G: Nucl. Part. Phys. **30**, 1517(2004).

[119] ALICE Collaboration, Technical Design Report for PMD, CERN/LHCC/99-32, 1999.

[120] Addendum to ALICE PMD TDR, CERN/LHCC 2003-38 (2003). CERN/LHCC 99-22, ALICE TDR 5, (1999).

[121] *http* : *//home.thep.lu.se/∼torbjorn/Pythia.html*.

[122] R. Brun, *et al.*, GEANT3 UserS Guide, CERN/DD/EE/ 84-1.

[123] *http* : *//wwwasdoc.web.cern.ch/wwwasdoc/geant_html3/geantall.html*

[124] S. Agostinelliae *et al*, Nucl. Inst. Meth. **A506**, 250 (2003).

[125] ALICE: Physics Performance Report, Volume II, J. Phys. G Nucl. Part. Phys. **32**, 1295(2006).

[126] K. Aamodt *et al*, JINST, **3** (2008).

[127] M. M. Agarwal et al Nucl. Inst. Meth. **A488**, 131(2002).

[128] Corcella, I.G. Knowles, G. Marchesini, S. Moretti, K. Odagiri, P. Richardson, M.H. Seymour and B.R. Webber, JHEP **0101** 010(2001).

[129] F.W. Bopp, R. Engel, J. Ranft hep-ph/9803437v1.

[130] M. Gyulassy and M. Plumer, Phys. Lett. B **243**, 432(1990).

[131] X. N. Wang and M. Gyulassy, Phys. Rev. Lett. **68**, 1480(1992).

[132] R. Baier, D. Schiff and B. G. Zakharov, Ann. Rev. Nucl. Part. Sci. **50**, 37(2000).

[133] K. Adcox *et al.* [PHENIX Collaboration], Phys. Rev. Lett. **88**, 022301(2002).

[134] C. Adler *et al.* [STAR Collaboration], Phys. Rev. Lett. **89**, 202301(2002).

[135] C. Adler *et al* (STAR), Phys.Rev.Lett. **90**, 082302(2003).

[136] M. Banner *et al.* [UA2 Collaboration], Phys. Lett. **B118**, 203(1982).

[137] G. Arnison *et al.* [UA1 Collaboration], Phys. Lett. B **123**, 115(1983).

[138] F. Abe *et al.* [CDF Collaboration], Phys. Rev. Lett. **62**, 613 (1989); Phys. Rev. **D41**, 1722(1990).

[139] Azimuthal Correlations of High-p_T Photons and Hadrons in Au+Au Collisions at STAR. (Thesis of Thomas Dietel)

[140] Two-particle azimuthal correlations in d+Au and p+p collisions at s_{NN} = 200 GeV in STAR. (thesis of F.Benedosso)

[141] CMS TriDAS Project Data Acquisition and High-Level Trigger Technical Design Report CERN/LHCC 2002-26CMS TDR 6.2

[142] S. V. Chekanov, Jet algorithms : A mini review, hep-ph/0211298.

[143] Gerald C.Blazey *et. al.* Run II Jet Physics in CDF, hep-ex/0005012v2.

[144] S.Catani, Y.L.Dokshitzer, M.H.Seymour, B.R.Webber, Longitudinally Invariant kT Clustering Algorithms for Hadron Hadron Collisions, Nucl. Phys. **B406** 187(1993).

[145] S. D. Ellis and D. E. Soper, Successive combination jet algorithm for hadron collisions, Phys. Rev. **D48** 3160(1993).

[146] F. Abe *et al.* (CDF), Phys. Rev. Lett. **70**, 2232(1993).

[147] R. Ansari *et al.* (UA2), Phys. Lett. **B194**, 158(1987).

[148] R. Ansari *et al.* (UA2), Z. Phys. **C41**, 395(1988).

[149] C. Albajar *et al* [by UA1 Collaboration], Phys. Lett. B **209**, 385(1988).

[150] R. Gandhi, F. Halzen and F. Herzog, Phys. Lett. B. **152** 261(1984).

[151] P. Aurenche, R. Baier, M. Fontannaz, Phys. Rev. D **42**, 1440(1990).

[152] P. Aurenche, P. Chiappetta, M. Fontannaz, J. .Ph. Guillet, E. Pilon Nucl. Phys. B **399**, 34(1993).

[153] M. Glück, L. E. Gordon, E. Reya, and W. Vogelsang, Phys Rev. Lett. **73**, 388(1994).

[154] D. Peressounko *et al* [for PHENIX collaboration], Nucl. Phys. A **783**, 577c(2007).

[155] ALICE Collaboration *et al*, J. Phys. G: Nucl. Part. Phys. **32**, 1295(2006).

[156] ALICE Collaboration *et al*, J. Phys. G: Nucl. Part. Phys. **30**, 1517(2004).

[157] I.G. Bearden et al, Phys. Rev. Lett. **93**, 102301(2004).

[158] B.B. Back et al, Phys. Rev. Lett. **91**, 052303(2003).

[159] I.G. Bearden et al, Phys. Rev. Lett. **94**, 162301(2005).

[160] B.B. Back et al, Phys. Rev. Lett. **91**, 052303(2003).

[161] J. Benecke, T.T.Chou, C.N.Yang and E.Yen, Phys. Rev. **188**, 2159(1968).

[162] J. Adams et al, Phys. Rev.C **73**, 034906(2006).

List of Publications (Work presented in the thesis ($\star$))

- *k_T measurement of partons from di-hadron correlation and a comparative study with jet reconstruction method using PYTHIA**, (Mriganka Mouli Mondal for STAR collaboration) to be appear in International Journal of Modern Physics E. Jet Workshop at Prague- 2010.

- *An Experimental Exploration of the QCD Phase Diagram: The Search for the Critical Point and the Onset of De-confinement*, By STAR Collaboration (, *et al.*). arXiv:1007.2613 [nucl-ex] (2010).

- *Measurement of the Bottom contribution to non-photonic electron production in p+p collisions at $\sqrt{s}$=200 GeV.*, By STAR Collaboration (M.M. Aggarwal *et al.*). arXiv:1007.1200 [nucl-ex] (2010).

- *Transverse momentum spectra of charged particles in proton-proton collisions at $\sqrt{s}$ = 900 GeV with ALICE at the LHC.*, By ALICE Collaboration (K. Aamodt *et al.*). arXiv:1007.0719 (2010).

- *Two-pion Bose-Einstein correlations in pp collisions at $\sqrt{s}$=900 GeV*, By ALICE Collaboration (K. Aamodt *et al.*), arXiv:1007.0516 (2010) .

- *Midrapidity antiproton-to-proton ratio in pp collisions at $\sqrt{s}$ = 0.9 and 7 TeV measured by the ALICE experiment.* By ALICE Collaboration (Authors:: K. Aamodt *et al.*). arXiv:1006.5432 (2010).

- *$K*0$ production in Cu+Cu and Au+Au collisions at $\sqrt{s_{NN}}$ = 62.4 GeV and 200 GeV.*, M.M. Aggarwal *et al.* arXiv:1006.1961 [nucl-ex] (2010).

- *Balance Functions from Au+Au, d+Au, and p+p Collisions at $\sqrt{s_{NN}}$= 200 GeV.*, By STAR Collaboration (M.M. Aggarwal *et al.*). arXiv:1005.2307 [nucl-ex] (2010).

- *Charged-particle multiplicity measurement in proton-proton collisions at $\sqrt{(}s)$ = 7 TeV with ALICE at LHC.*, By ALICE Collaboration (K. Aamodt *et al.*), arXiv:1004.3514 (2010).

- *Charged-particle multiplicity measurement in proton-proton collisions at $\sqrt{s}$ = 0.9 and 2.36 TeV*, with ALICE at LHC. K. Aamodt *et al.*, arXiv:1004.3034 (2010).

- *Azimuthal di-hadron correlations in d+Au and Au+Au collisions at $\sqrt{s_{NN}}$ = 200 GeV*, from STAR. By STAR Collaboration (M.M. Aggarwal *et al.*), arXiv:1004.2377 [nucl-ex] (2010).

- *Charged and strange hadron elliptic flow in Cu+Cu collisions at* $\sqrt{s_{NN}}$ *= 62.4 and 200 GeV.*, By The STAR Collaboration (B.I. Abelev *et al.*), Phys.Rev. C81, 044902(2010).

- *Upsilon cross section in p+p collisions at* $\sqrt{s}$ *= 200 GeV.*, By STAR Collaboration (B.I. Abelev *et al.*).arXiv:1001.2745 [nucl-ex] (2010).

- *Inclusive* π^0*,* η*, and direct photon production at high transverse momentum in p+p and d+Au collisions at* $\sqrt{s}$ *= 200 GeV.* By STAR Collaboration (B.I. Abelev *et al.*). arXiv:0912.3838 [hep-ex] (2009).

- *Studying Parton Energy Loss in Heavy-Ion Collisions via Direct-Photon and Charged-Particle Azimuthal Correlations.*, By STAR Collaboration (B.I. *Abelev et al.*). e-Print: arXiv:0912.1871 [nucl-ex] (2009).

- *Observation of pi+ pi- pi+ pi- Photoproduction in Ultra-Peripheral Heavy Ion Collisions at STAR*, By STAR Collaboration (B.I. Abelev *et al.*). Phys.Rev. C81,044901(2010).

- *First proton-proton collisions at the LHC as observed with the ALICE detector: Measurement of the charged particle pseudorapidity density at* $s^{1/2}$ *= 900-GeV. By ALICE Collaboration (K Aamodt et al.). Eur.Phys. J.C 65 111(2010).*

- *Spectra of identified high-*p_T $\pi^{\pm}$ $p(\bar{(}p))$ *in Cu + Cu collisions at* $\sqrt{s_{NN}}$*= 200 GeV. By STAR Collaboration (B.I. Abelev et al.). Phys.Rev. C81, 054907(2010).*

- *Longitudinal double-spin asymmetry and cross section for inclusive neutral pion production at midrapidity in polarized proton collisions at* $\sqrt{s}$*= 200 GeV By The STAR Collaboration (B.I. Abelev et al.), Phys.Rev D80, 111108(2009).*

- *A Method based on transverse energy balance of jets for selection of direct photons and fragmentation photons in high energy pp collisions***. Mriganka Mouli Mondal, Subhasis Chattopadhyay, (Calcutta, VECC) . arXiv:0903.3001 [nucl-ex] (2009).*

- *The ALICE experiment at the CERN LHC; By ALICE Collaboration (K. Aamodtet al.). JINST 3: S08002,2008 (2008).*

- *ALICE electromagnetic calorimeter technical design report, By ALICE Collaboration (P. Cortese et al.). CERN-LHCC-2008-014, CERN-ALICE-TDR-014, Sep 2008. 132pp.*

Conference Proceedings :

- **Fabrication and testing of ALICE PMD modules**, M.M. Aggarwal et. al., Proceedings of the DAE-BRNS Symp. on Nucl. Phys. held at M. S. University, Varoda, India from Dec. 11 to 15, 2006 Vol. 51, (2006) 648.

- **Baryon production and the centrality dependence of limiting fragmentation in heavy ion collisions**, M.M. Mondal, S. Chattopadhyay , Proceedings of the DAE-BRNS Symp. on Nucl. Phys. held at M. S. University, Varoda, India from Dec. 11 to 15, 2006 , Vol. 51, (2006) 538.

- **Status of Photon Multiplicity Detector in ALICE**, Proceedings of the DAE-BRNS Symp. on Nucl. Phys. held at Sambalpur University, Sambalpur, Orissa, India from Dec. 11 to 15, 2007, Vol. 52, (2007) 650.

- **Simulation framework for Photon Multiplicity Detector in ALICE** C. Jena et. al. Proceedings of the DAE-BRNS Symp. on Nucl. Phys. held at Sambalpur University, Sambalpur, Orissa, India from Dec. 11 to15, 2007, Vol. 52, (2007) 543.

- **Measurement of Photon Multiplicity at forward rapidity in ALICE** Poster presented in the 20th International Conference of Ultra Relativistic Nucleus Nucleus Collisions held at Jaipur, India from Feb. 4 to 10, 2008.

- **Centrality dependence of pseudorapidity distributions of baryons in heavy ion collisions at RHIC**, M.M. Mondal, S. Chattopadhyay, Poster presented in the 20th International Conference of Ultra-Relativistic Nucleus Nucleus Collisions held at Jaipur, India from Feb. 4 to 10, 2008.

- **Measurement of the production of direct photon jet in high energy collisions and study of photon-charge particle correlation**, Proceedings of the DAE-BRNS Symp. on Nucl. Phys. held at IIT Roorkee, Uttarakhand, Dec. 22-26, 2008.

- **A study of enrichment of direct photons by isolation and transverse energy balance of jets at LHC energies**, DAE - HEP symposium, Varanasi (14 - 18th December 2008).

- **Transverse energy balance for the estimation of fragmentation photons in pp collisions** Quark Matter 2009, Oak Ridge National Laboratory, TN